Copia del Acta, inscrita a fojas setenta y cinco del Libro Vigesimotercero, del Examen Final presentado por el señor Antonio Morelos Pineda para obtener el grado de Doctor en Ciencias en la especialidad de Física.

En la Ciudad de México, a los veintitrés días del mes de octubre del año de mil novecientos noventa y dos, se reunieron en el Departamento de Física del Centro de Investigación y de Estudios Avanzados del Instituto Politécnico Nacional, los señores: Doctor Augusto García González, Investigador Titular; Doctor Miguel Angel Pérez Angón, Investigador Titular; y Doctor Gerardo Antonio Herrera Corral, Investigador Adjunto; todos ellos Investigadores del mencionado Departamento; y, como Sinodales Invitados por el Centro, el Doctor Fernando Matías Moreno Yntriago, Investigador Titular del Departamento de Física Teórica del Instituto de Física de la Universidad Nacional Autónoma de México, y el Doctor Joseph Lach, Profesor de la Research Division del Fermi National Accelerator Laboratory, en Batavia, Illinois, U.S.A., a fin de efectuar el Examen Final que para obtener el grado de Doctor en Ciencias sustentó el señor Antonio Morelos Pineda, Físico y Maestro en Ciencias (Física).

El señor Antonio Morelos Pineda presentó la tesis titulada: "Medida de la polarización y momento magnético de los hiperones Σ^+ y Σ^-", que fue desarrollada bajo la dirección del Doctor Joseph Lach y del Doctor Augusto García González.

Con fundamento en los resultados de este examen, el Jurado dictaminó que el señor Antonio Morelos Pineda aprobó el Examen Final para obtener el grado de Doctor en Ciencias en la especialidad de Física.

Augusto García González

Miguel Angel Pérez Angón

Gerardo Antonio Herrera Corral

Fernando Matías Moreno Yntriago

Joseph Lach

El Director del Centro certifica que las firmas que anteceden son auténticas.

Feliciano Sánchez Sinencio

A11 37:81

CENTRO DE INVESTIGACION Y DE
ESTUDIOS AVANZADOS DEL IPN

MEDIDA DE LA POLARIZACION Y MOMENTO MAGNETICO DE LOS HIPERONES Σ^+ y $\bar{\Sigma}^-$

TESIS

Presentada al Departamento de Física como
requisito parcial para la obtención del
grado de Doctor en Ciencias
por

Antonio Morelos Pineda

México, D.F.
23 de octubre de 1992

A mi esposa Leticia, a mi hijo Aaron
A mis padres Arturo y Leonor
A mis Hermanas y Hermanos

MEASUREMENT OF THE POLARIZATION

AND

MAGNETIC MOMENT

OF

Σ^+ AND $\bar{\Sigma}^-$ HYPERONS

"Resumen"

Las mediciones de la polarización y el momento magnético de los hiperones Σ^+ y $\bar{\Sigma}^-$ han sido hechas usando el aparato E761 en Fermilab. Hiperones polarizados a 375 GeV/c fueron producidos inclusivamente haciendo incidir protones de 800 GeV contra un blanco fijo de cobre.

Los resultados muestran que la polarización de Σ^+ crece de cero a cero $p_\perp$ hasta un máximo de $\approx$ 16 % a un $p_\perp$ de 1 GeV/c y luego desciende hasta $\approx$ 10 % a un $p_\perp$ de 1.7 GeV/c. Dependencia de la polarización de Σ^+ como función de la energía es observada cuando los datos son comparados contra otras mediciones hechas con protones a una energía de 400 GeV. Por primera vez es reportada la medición de la polarización de $\bar{\Sigma}^-$. La polarización de $\bar{\Sigma}^-$ es del mismo signo y menor que la polarización de Σ^+ . La polarización de $\bar{\Sigma}^-$ tiene la misma dependencia en $p_\perp$ aunque el máximo esta a un diferente valor de $p_\perp$. La polarización de $\bar{\Sigma}^-$ crece de cero a cero $p_\perp$ hasta un máximo de $\approx$ 10 % a un $p_\perp$ de 0.7 GeV/c y luego desciende hasta $\approx$ 6 % a un $p_\perp$ de 1.0 GeV/c.

El momento magnético es medido haciendo uso de la técnica de precesión de spin. El spin precesa mientras atravieza un campo magnético cuya integral ($\int B\,dl$) es de $\approx$ 20 $T \cdot m$. La medición del ángulo de precesión es hecha con 250000 eventos del tipo $\Sigma^+ \rightarrow p\pi^0$ arrojando un error estadístico de $\approx$ 0.1 % en el momento magnético. De igual manera el ángulo de precesión de $\bar{\Sigma}^-$ es medido con 12000 eventos del tipo $\bar{\Sigma}^- \rightarrow \bar{p}\pi^0$ arrojando un error estadístico de $\approx$ 1.5 %. Mediciones preliminares del momento magnético dan por resultado:

$$2.4707 \pm 0.0035 \pm 0.0199\ \mu_N \text{ para } \Sigma^+$$
$$\text{y}$$
$$-2.4375 \pm 0.0363 \pm 0.0199\ \mu_N \text{ para } \bar{\Sigma}^- .$$

El error sistemático esta dominado por la medición del campo magnético.

Abstract

Polarization and magnetic moment of the Σ^+ and $\bar{\Sigma}^-$ hyperons has been measured using the Fermilab E761 apparatus. Polarized hyperons at 375 GeV/c were produced inclusively with 800 GeV protons incident on a Cu target.

Polarization results indicate that the Σ^+ polarization increases from zero at zero $p_\perp$ to a maximum of $\approx$ 16 % at $p_\perp$ of 1 GeV/c and then decreases to $\approx$ 10 % at $p_\perp$ of 1.7 GeV/c. A production energy Σ^+ polarization dependence is observed when the data are compared to polarization measurements with incident protons at 400 GeV. The first measurement of $\bar{\Sigma}^-$ polarization has been performed. The $\bar{\Sigma}^-$ polarization has the same sign as the Σ^+ but has smaller magnitude. The $\bar{\Sigma}^-$ polarization has the same $p_\perp$ dependence as the Σ^+ but it peaks at different $p_\perp$. It increases from zero at zero $p_\perp$ to a maximum of $\approx$ 10 % at $p_\perp$ of 0.7 GeV/c and then decreases to $\approx$ 6 % at $p_\perp$ of 1.0 GeV/c.

The magnetic moment is measured using the spin precession technique. The hyperon spin precessed while passing through an $\approx$ 20 $T \cdot m$ integral magnetic field. The Σ^+ spin precession is measured with 250000 $\Sigma^+ \rightarrow p\pi^0$ decay events providing $\approx$ 0.1 % statistical error on the magnetic moment. Similarly the $\bar{\Sigma}^-$ spin precession is measured with 12000 $\bar{\Sigma}^- \rightarrow \bar{p}\pi^0$ decay events providing $\approx$ 1.5 % statistical error. Preliminary magnetic moment measurements are found to be:

$$2.4707 \pm 0.0035 \pm 0.0199\ \mu_N \text{ for } \Sigma^+$$
$$\text{and}$$
$$-2.4375 \pm 0.0363 \pm 0.0199\ \mu_N \text{ for } \bar{\Sigma}^- .$$

The systematic error is dominated by the magnetic field measurement.

Acknowledgements

I have interacted with so many people while pursing my training to become a Ph.D. in experimental high energy physics at Fermilab (March 1986 to october 1992) that the list of persons would be rather large. The list grows even larger including the people involved while I was taking courses as a M.Sc. and Ph.D. student at CINVESTAV. To all of them thanks. Special remarks follows:

Augusto Garcia who guided me to reach the area of research that matched the ideas which were wandering in my head. All the time I wished to be in a physics research program where I could learn and use skills, beyond the pencil and paper or buy the machines and make the measurements; experimental high energy physics meets my requirements and even goes beyond in a very modern context. I am proud of all the senior professors of CINVESTAV for keeping themselves at the world level of research and encouraging their students to go deeply into the wonders of science.

Joe Lach, my advisor at Fermilab, for taking me as his student on unusual circumstances, for reading and correcting my thesis, and for leading and designing the strategy for data taking which transformed into the now shining E761 results.

The kind of research I have done was made possible only because Leon Lederman, Director Emeritus of Fermilab, had the vision to link Latino-America to experimental high energy physics research, a decade ago. Ten years ago, I started the M.Sc. program at CINVESTAV. I should comment that since the beginning of the mexican physics structure there has been, and still there are, international links in many other areas of physics.

I had a great time around Fermilab, learning from and meeting with people, looking at organizational structure, and playing with todays technology, all of that towards a physics goal. All my activities were driven by the research I have done with the E761 collaboration. Thanks to each one of the E761 collaborators, without their work I could never have completed my tasks, and thanks for overcoming the linguistic, cultural, and character differences.

Philippe Gouffon who helped me to jump from zero knowledge in computer and hardware into a skillful person to keep up with the experiment. Also thanks for his immense work in making all our E761 environment a complete and shareable solid piece.

Charles Newsom for his patience in co-working with me in several parts of the experiment, for the continuous conversations we had, and for encouraging me to do my best at all times.

Nikolai Terentiev for continuous conversation on all related topics.

Alexander Denisov and Victor Golovtsov for their enormous patience while interacting with me during the assembly of the readout electronics.

I am greatly thankful to Peter Cooper for his patience in all the conversations we had in all subjects. He is a person with broad experiences covering tiny technical details to entire physics goals, a person with outstanding abilities to interact and guide students and a person which made a variety of contributions to the experiment.

Another experience, inherit to this collaboration, was the access to meet people, and to apply technology, from the USSR. No need to travel overseas. Thanks in particular to the Leningrad group for providing, I can say 80% of, the tracking and readout equipment.

My colleagues students, Roberto Mahon, Ivone Freire, Tim Dubbs, Steve Timm, Dong Chen, and Maurice Foucher, for their dedicated work and for the discussions we had around the experiment.

David Daniels, an undergraduate student, and Yuanyuan Zhong for co-working with me doing analysis and software directly related to my thesis topic.

Tim Dubbs, Vince Smith, Nicolai Kuropatkin and David Daniels for the time they dedicate for reading and correcting the thesis.

Roy Rubinstein, the person who is in charge of the links of Latino-America high energy physics at Fermilab.

Willma Cardona and Boris Jurkiew for always finding a way to keep me aligned with the USA Immigration and Naturalization Service.

Mark Bernett, Sten Hansen, Art Neubauer (including all PREP), and Ron Miska for the patience they had answering my questions and requests during the setup and running of E761. Thanks to the Computer Division

which has worked excellent, during the run and analysis time.

Lewis Morris, for being in charge of the technical work for E761, from setup to dismantling. Gregory Sellberg for joining the technical work during the setup and running period.

My latino-american colleagues Gerardo Moreno, Hector Mendez, Arturo Fernandez, and German Valencia for all the conversations we have had.

In the mean time I needed to survive. Fermilab was able to incorporated me in its structure as a guest scientist, a pompous title while I was student. CONACyT supported me since the beginning of the M.Sc. program to the first two years of my Ph.D. program, the nominal five years. I remember that in my student days at CINVESTAV, CINVESTAV itself provided the students a compensation.

FERMILAB EXPERIMENT E761

An Electroweak Enigma: Hyperon Radiative Decays

R. Carrigan, P.S.Cooper, H. Gottschalk, J. Lach, A. Morelos[a,b]
FERMILAB, Batavia, Illinois 60510

Li Yunshan, Tang Fukun, Lang Pengfei, Li Chengze Shi Huanzhang,
Zhao Wenheng, Dia Lisheng, Zheng Shuchen, Zhong Yuanyuan, Yan Jie
Institute of High Energy Physics, Beijing, PRC

V. Baublis, N.F. Bondar, A.S. Denisov, A. Dobrovolsky, V.L. Golovtsov,
V.T. Grachev, A.V. Khanzadeev, N. Kuropatkin, V.M. Samsonov, V. Schegelsky,
N.K. Terentyev, I.I. Tkatch, L.N. Uvarov, A.A. Vorobyov[1]
St. Petersburg Nuclear Physics Institute, St. Petersburg, Russia

P.A. Goritchev, M.A. Kubantsev, V .N. Lebedenko
Institute of Theoretical and Experimental Physics, Moscow, Russia

T. Dubbs[a], E. McCliment, C. Newsom
University of Iowa, Iowa City, Iowa 42242

I.F. Alburquerque[a], C. Escobar, P. Gouffon, J. Mahon[a]
University of Sao Paulo, Brazil

M. Foucher[a]
Yale University, New Haven, Connecticut 06511

A.M.F. Endler
Centro Brasileiro de Pesquisas Fisicas, Rio de Janeiro, Brazil

M.C. Pommot Maia
Conselho Nacional de Pesquisa - CNPq, Rio de Janeiro, Brazil

D. Chen[a]
State University of New York - Albany, Albany, New York 12222

V.J. Smith
H.H. Wills Physics Laboratory, University of Bristol, United Kingdom

S. Timm[a]
Carnegie Mellon University, Pittsburgh, PA 15213

M. Luksys
Universidade Federal da Paraiba, Paraiba Brazil

[1] Spokesman
[a] graduate student
[b] graduate student from CINVESTAV-IPN, México

Contents

"Resumen" i

Abstract ii

Acknowledgments iii

List of Figures viii

List of Tables ix

Introduction 1

1 Experimental and Theoretical Review 2
- 1.1 Polarization 4
  - 1.1.1 Polarization Experimental 6
  - 1.1.2 Polarization Theory 11
- 1.2 Magnetic Moment 17
  - 1.2.1 Magnetic Moment Experimental 18
  - 1.2.2 Magnetic Moment Theory 19

2 Experimental Setup 24
- 2.1 Introduction 24
- 2.2 Hyperon Production 27
  - 2.2.1 Beamline 28
  - 2.2.2 Target 33
  - 2.2.3 Hyperon Target Magnet (HTM) 34
- 2.3 Hyperon Spectrometer 35
  - 2.3.1 Silicon Strip Detector (SSD) 37
  - 2.3.2 Hyperon Dipole Magnet (HYPE2) 40
- 2.4 Baryon Spectrometer 40
  - 2.4.1 Proportional Wire Chamber (PWC) 40

2.4.2 Baryon Dipole Magnet (MA-MB-MC) 42
2.5 Photon Spectrometer 42
2.5.1 Electromagnetic Calorimeter (EC) 43
2.5.2 Transition Radiation Detector (TRD) 45
2.6 Trigger 45
2.6.1 Counters and Logic 48
2.7 Data Acquisition (DAQ) 51
2.7.1 Rates 53

3 Data Analysis **56**
3.1 Track Reconstruction 56
3.2 Alignment of Chambers (SSD and PWC) 58
3.3 Signal Σ^+ and $\bar{\Sigma}^-$ 59
3.4 Absolute Momentum Calibration 64
3.5 Target: Angles, Position and HTM Ptk 65
3.6 Polarization 71
3.6.1 Polarization Measurement Technique 71
3.6.2 Hyperon Phase Space 73
3.6.3 Polarization and Targeting angle Sign 73
3.6.4 Acceptance Function 77
3.6.5 Comparing Arithmetic and Geometric Mean 82
3.6.6 History: Asymmetry Measurement 84
3.6.7 Systematic: Binning in θ_{x0} and θ_{y0} 85
3.6.8 Systematic: Run by Run and Variable Splitting 87
3.6.9 Polarization Σ^+ 89
3.6.10 Polarization $\bar{\Sigma}^-$ 91
3.7 Magnetic Moment 93
3.7.1 Spin Precession Technique 93
3.7.2 Determination of n 2 π 94
3.7.3 History: Magnetic Moment Measurement 95
3.7.4 Systematic: Binning in θ_{x0} and θ_{y0} 95
3.7.5 Systematic: Run by Run and Variable Splitting 96
3.7.6 Systematic: HTM and HYPE2 Ptk 98
3.7.7 Magnetic Moment Σ^+ and $\bar{\Sigma}^-$ 100

4 Comparisons and Conclusions **106**
4.1 Polarization Σ^+ 106
4.2 Polarization $\bar{\Sigma}^-$ 108
4.3 Magnetic Moment 109

A Fermilab Accelerator Complex **112**

B E761 Track Fit Algorithm **115**

C Bias Canceling Method (BCM) **119**
C.1 Arithmetic Mean (BCMAM) 120
C.2 Geometric Mean (BCMGM) 123

D Spin Precession in a Magnetic Field **126**

List of Figures

1.1 Standard Model 3
1.2 Baryon Octet and Decouplet. 4
1.3 Polarization in Inclusive Hyperon Production by Unpolarized Protons on Fixed Target, Σ^+ , Σ^- , and Σ^0 8
1.4 Polarization in Inclusive Hyperon Production by Unpolarized Protons on Fixed Target, Ξ^- , Ξ^0 , and $\bar{\Xi}^+$ 9
1.5 Polarization in Inclusive Hyperon Production by Unpolarized Protons on Fixed Target, Λ^0 , $\bar{\Lambda}^0$, and Ω^- 10
1.6 Kane: One and Two Gluon Exchange Diagrams. 12
1.7 Moriarty: Polarization Contribution $K^*(890)$ and $K^*(1420)$ on Λ^0 13
1.8 DeGrand: Polarization on Λ^0 as a Function of x_f and $p_\perp$ . . . 14
1.9 Szwed: Polarization on Λ^0 14
1.10 Erhan (LUND): Polarization on Λ^0 15
1.11 Cea: Polarization on Λ^0 , predictions on Σ^+ and Σ^- 15
1.12 Soffer: Polarization on Λ^0 16
1.13 Dharmaratna: Polarization on Λ^0 17

2.1 E761 Apparatus Geometry. 25
2.2 Naive Σ^+ and $\bar{\Sigma}^-$ Production. 28
2.3 Estimated Beam Fractions at 10 m from the Target with 800 GeV Incident Protons. 29
2.4 Proton Beam Layout. 32
2.5 Proton Beam at +3.0 $mrad$ Horizontal and Vertical Mode. . 33
2.6 E761 Target Sketch. 34
2.7 Hyperon Target Magnet and E761 Tungsten Channel. 36
2.8 Hyperon Target Magnetic Field Map at 3230 $Amps$ 37
2.9 Horizontal Forbidden Targeting Angles. 38
2.10 Hyperon Spectrometer. 39
2.11 Baryon Spectrometer. 41
2.12 Photon Spectrometer. 44

2.13 Electromagnetic Calorimeter Geometry. 46
2.14 Transition Radiation Detector Geometry. 47
2.15 Qualitative Enhancement of Trigger with the EC Energy Cut. 50
2.16 E761 Trigger Components. 52
2.17 E761 Data Acquisition. 54

3.1 χ^2_ν for Hyperon and Baryon Tracks Run 2116. 58
3.2 θ_{YB} Versus r Scatter Plot. 61
3.3 Neutral Mass Square for Positive and Negative Hyperon Beam. 62
3.4 Neutral Mass Square Versus r. 65
3.5 $T1PS$-Alignment projected into the Target x Center. 69
3.6 Cosine Event Distributions. 74
3.7 Event Distribution in θ_{x0} and θ_{y0} 75
3.8 Event Distribution in x_f and $p_\perp$ 76
3.9 Horizontal Σ^+ Polarization and Targeting Angle Signs. . . . 78
3.10 Horizontal $\bar{\Sigma}^-$ Polarization and Targeting Angle Signs. . . . 79
3.11 Vertical Σ^+ Polarization and Targeting Angle Signs. 80
3.12 Vertical $\bar{\Sigma}^-$ Polarization and Targeting Angle Signs. 81
3.13 Acceptance Function from Data. 83
3.14 Historical Asymmetry Review. 86
3.15 Asymmetry Versus Time. 88
3.16 Asymmetry Study from Variable Splitting. 90
3.17 Polarization Versus x_f 91
3.18 Polarization Versus $p_\perp$ for Σ^+ 92
3.19 Megasample Data Polarization Versus $p_\perp$ 93
3.20 Polarization Versus $p_\perp$ for $\bar{\Sigma}^-$ 94
3.21 Spin Precession in a Magnetic Field. 95
3.22 Precession Angle Versus Ptk 96
3.23 Polarization Vector Before and After Precession. 97
3.24 Historical Magnetic Moment Review. 98
3.25 Magnetic Moment Versus Time. 102
3.26 Magnetic Moment Study from Variable Splitting. 105

4.1 Σ^+ Polarization World Data. 106
4.2 Anti-Hyperon Polarization. 109
4.3 E761 $\bar{\Sigma}^-$ and Σ^+ Polarization. 110
4.4 Σ^+ and $\bar{\Sigma}^-$ Magnetic Moment. 111

A.1 Fermilab Accelerator Complex. 112

B.1 Mid Plane Momentum Deflection. 116

C.1 Geometric Mean. 124

List of Tables

1.1 Experimental Baryon Magnetic Moments. 19
1.2 Baryon SU(6) Spin-Flavor Wave Functions. 20
1.3 Naive Quark Model. 21
1.4 Gupta: Fit to Baryon Magnetic Moments. 23

2.1 Proton Beam Intensity and Beam Dipole Magnets. 31
2.2 Number of Triggers or Events to Tape. 55

3.1 Analysis Cuts. 63
3.2 Targeting Angle, $p_\perp$, HTM Ptk , and Number of $\Sigma^+ \rightarrow p\pi^0$. 68
3.3 Hyperon x and y Target Position, Momentum and σ. 70
3.4 Asymmetry using Arithmetic and Geometric Mean. 84
3.5 Asymmetry Σ^+ 101
3.6 Polarization Σ^+ 102
3.7 Asymmetry $\bar{\Sigma}^-$ 103
3.8 Polarization $\bar{\Sigma}^-$ 104
3.9 Magnetic Moment. 104

4.1 Parameters of E620, E497, and E761. 111

A.1 Fermilab Acceleration Stages. 113

Introduction

Although the Σ^+ and $\bar{\Sigma}^-$ hyperons were discovered by the 50's and 60's respectively, they still contribute to today's understanding of nature. Obviously, they will not reveal the ultimate structure of matter, but through precision measurement of their properties and their decays they will shed light on contemporary theoretical understanding of branching ratios, production cross sections, asymmetry parameters, production polarization, and magnetic moments. E761, a multinational collaboration included scientists from Former USSR (today Russia), England, China, Brazil, USA and Mexico, was formed in 1984 with a commitment to contribute to hyperon physics. The group took data at the Proton Center beam line at Fermilab in 1990. My thesis is concerned with the measurement of the production polarizations and magnetic moments of Σ^+ and $\bar{\Sigma}^-$ through the decays $\Sigma^+ \rightarrow p\pi^0$ and $\bar{\Sigma}^- \rightarrow \bar{p}\pi^0$.

Chapter 1

Experimental and Theoretical Review

The modern starting point of particle physics is the standard model (SM), which in its most simple version states that the most fundamental point-like particles are the leptons and quarks (which obey fermion statistics), with interactions between them mediated by gauge bosons. There are three generations of leptons and quarks. Interactions are classified as electroweak, mediated by γ , $W^{\pm}$, and Z^0 with characteristic times for weak process on the order of $10^{-8} sec$ and for electromagnetic process $10^{-20} sec$. Strong interactions, mediated by gluons having characteristic times on the order of $10^{-23} sec$. The gravitational force is neglected. These particles can be characterized by a set of parameters which include: mass, spin, magnetic moment, isospin, hypercharge, flavor, color, charge, and parity, not all of them are independent from each other. Along with the leptons and quarks there is a set of associated particles characterized mainly by having the same mass but opposite charge which are called anti-particles. Figure 1.1 sketches the elements of the standard model.

Particles made of three quarks are called baryons. Particles with two

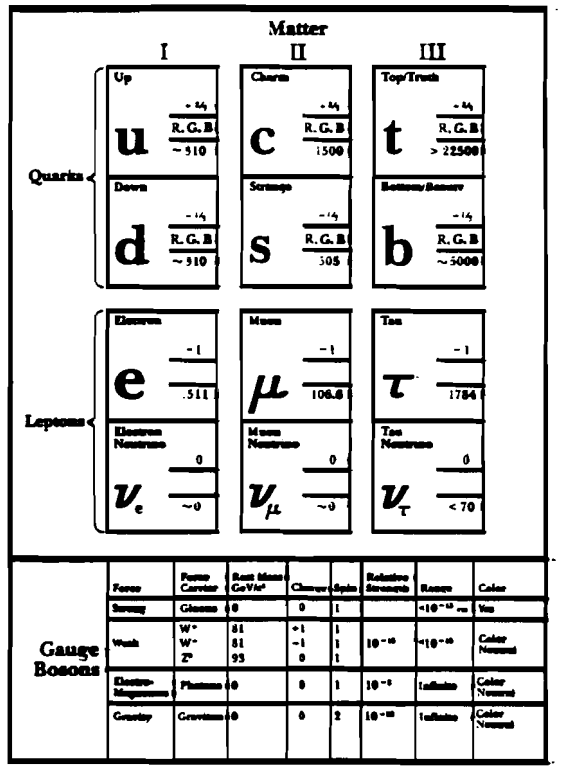

Figure 1.1: Standard Model .

quarks (quark and anti-quark) are called mesons. Hyperons [1] are a subset of baryons, which contain at least one s quark. Figure 1.2 shows the structure of the baryon quark model using only the u, d, and s quarks. The quark model classifies the particles through the SU(3) group [2] . One of the multiplets is called decuplet composed of spin $\frac{3}{2}$ baryons with almost all of them decaying through strong interactions, except for the Ω^- . The other multiplet is called octect composed of spin $\frac{1}{2}$ baryons to which the Σ^+ belongs.

The Σ^+ ($\bar{\Sigma}^-$) polarization (spin) physics allows us to study the u, d, and s quark recombination process in hadron collisions. It uses the dynamics of the strong interaction to produce polarized hyperons from a totally unpolarized beam and target nucleons. The weak interaction governs the decay $\Sigma^+ \rightarrow p\pi^0$ ($\bar{\Sigma}^- \rightarrow \bar{p}\pi^0$) which allows me to identify and measure the

[1] Through this thesis the following points apply:

- A hyperon can mean either a hyperon itself or an anti-hyperon. Similarly baryon and anti-baryon or quark and anti-quark, unless explicitly specified.
- The sign on top right of the symbol is the charge. Example: $\bar{\Sigma}^-$ is the anti-hyperon of Σ^+ .

[2] The special unitary matrix group SU(3), contains three independent elements in its fundamental representation [2, 3]. Those elements are identified as the u,d, and s flavors.

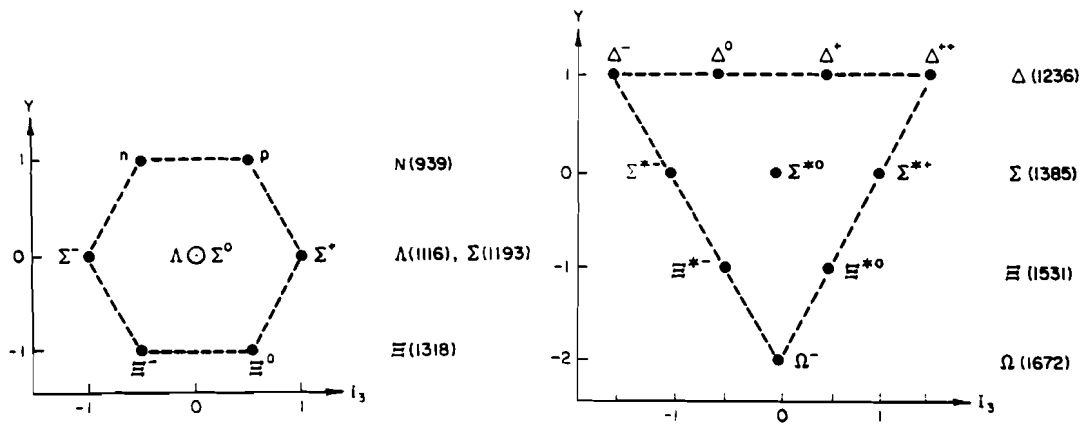

Figure 1.2: Baryon Octet and Decouplet.

polarization of the hyperon.

The Σ^+ ($\bar{\Sigma}^-$) magnetic moment physics allows us to study the internal structure of the baryons. Static models assume non-interacting quarks, so the baryon magnetic moment is the sum of the three constituent quark magnetic moments. The dynamics of the strong interaction between the quarks make corrections to the baryon magnetic moment.

1.1 Polarization

The polarization ($\vec{\mathbf{P}}$) is not an intrinsic property of a particle. The polarization is measured along a specified direction on an ensemble of particles, and defined as the number of particles with spin projected up ($N\uparrow$) minus the number of particles with the spin projected down ($N\downarrow$), normalized to the total number of particles. The polarization can be stated as:

$$\left|\vec{\mathbf{P}}\right| = \frac{N\uparrow - N\downarrow}{N\uparrow + N\downarrow}$$

From parity conservation: [3] : the hyperon polarization vector should

[3] A direct proof is to take combinations of the momentum vectors, of the incident proton

be along the cross product between the incident proton momentum and hyperon momentum as:

$$\vec{\mathbf{P}} \sim \vec{p}_{p_{incident}} \times \vec{p}_{hyperon} \tag{1.1}$$

We use the Basel Convention [14] which states that positive polarization will point in the same direction as the cross product 1.1.

Before going into the experimental review section, I describe the parity violation effect of the polarized hyperon (Y) over the angular distribution of the baryon (B) and neutral meson (X) in the decay $Y \rightarrow B + X$. The angular distribution of the baryon allow me to measure the polarization as I explain in the following lines.

The orbital angular state of a spin $\frac{1}{2}$ baryon and a spin zero neutral coming from a spin $\frac{1}{2}$ hyperon can be written in terms of S and P waves by angular momentum conservation as:

$$\Psi_{BX} = S\Psi_S(J = 1/2, l = 0) + P\Psi_P(J = 1/2, l = 1)$$

As a result, the baryon angular distribution in the hyperon center of mass system (CM) is written as [4] :

$$I(\theta, \phi) = |\Psi|^2 = \frac{1}{N_0}\frac{dN}{d\Omega} = \frac{1}{4\pi}(1 + \alpha\ \vec{\mathbf{P}}\ \cdot \hat{p}_b)$$

where:

$$\alpha = \frac{-2Re\, S^* P}{|S|^2 + |P|^2},$$

and produced hyperon, to set the direction of the polarization vector. Then apply the parity operation and realize that only the cross product of those vectors is an invariant vector under parity.

[4] As an illustration [4] consider the case in which the hyperon is totally polarized along an axis. Using the Clebsch-Gordan coefficients and the spherical harmonics for the states $\Psi_S(J = 1/2, l = 0, Jm = +1/2)$ and $\Psi_P(J = 1/2, l = 1, Jm = +1/2)$ I can write:

$$\Psi_{BX} = S Y_0^0 \chi^+ + P\left[\sqrt{\frac{2}{3}} Y_1^1 \chi^- - \sqrt{\frac{1}{3}} Y_1^0 \chi^+\right]$$

it is straight forward to get:

$$I(\theta) = |\Psi|^2 = 1 + \alpha \cdot \cos\theta$$

$\Sigma^+ \rightarrow p\pi^0$ α parameter is -0.980 ± 0.016 [1],

$\bar{\Sigma}^- \rightarrow \bar{p}\pi^0$ α parameter is $+0.980 \pm 0.016$ [5],

$\hat{p}_b$ is a unit vector along the baryon momentum in the hyperon CM,

N_0 is the total number of events in the sample,

1.1.1 Polarization Experimental

The discovery of the high energy Λ^0 polarization by experiment E8 at Fermilab in 1976 [22] marks the beginning of studies on high energy hyperon polarization in inclusive reactions:

$$p + N \rightarrow hyperon + X$$

where: p is a proton beam, N is a nucleon fixed target, X represents all other particles, and the momentum of the particles is $\geq 10\ GeV/c$ [6] .

The hyperon polarization has been studied over a range of variables as: beam energy, target material (interaction length), x_f [7] and $p_\perp$ [8] .

All octect hyperons, $\bar{\Lambda}^0$, $\bar{\Xi}^+$, $\bar{\Sigma}^-$ and the stable decouplet hyperon, Ω^- , produced in inclusive reactions have been studied for polarization using

[5] With the assumption that the weak interaction (or weak hamiltonian) is CP invariant, and noting that particle and anti-particle states are identical under CP then the S and P amplitudes for particle and antiparticle are related by [15]: $S = -\bar{S}$ and $P = \bar{P}$.

[6] Hyperon polarization phenomena at energies $\leq 1\ GeV$ has been experimentally known and quantitatively described by a finite number of coherent amplitudes and phases in exclusive reactions since the early 60's [20].

This wave analysis predicts that hyperon polarization at high energies will disappear. High energy means more possible amplitudes (final states), each with a different phase. The polarization decreases because of the increase of incoherent final states.

[7] The ratio of the longitudinal hyperon momentum along the incident proton momentum to the incident proton momentum at the production point is called Feynman x (x_f). The x_f is approximated to $x_f = \frac{p_{hyperon}}{p_{incident\ proton}}$

[8] The perpendicular hyperon momentum to the incident proton momentum at the production point is called $p_\perp$.

fixed target mode experiments with an unpolarized proton beam [9] . Figures 1.3,1.4, and 1.5 show a sample of each one polarized hyperon.

$\bar{\Lambda}^0$ is unpolarized [24, 25, 28, 33]. The unpolarized $\bar{\Lambda}^0$ result made the belief that all anti-hyperons were unpolarized, supporting models based on leading particle effect. That myth turned down with the measurement of the $\bar{\Xi}^+$ polarization in 1990.

$\bar{\Xi}^+$ [45] is polarized. The magnitude of the $\bar{\Xi}^+$ and Ξ^- polarization is the same.

$\bar{\Sigma}^-$ polarization has been measured for the first time by E761. This thesis reports its non-zero polarization and $p_\perp$ dependence, see section 4.

Ω^- has negligible polarization [46, 48].

All the octect hyperons are polarized. In the following lines I add a few comments on each one of them.

Λ^0 polarization is the most studied of all hyperons [22, 23, 24, 25,

[9]The studies of polarization have gone beyond the hyperons. Also, hyperon polarization studies have been made on a variety of modes. The following lines list several of those studies.

Proton polarization has been studied in inclusive production by proton beam on H_2 and on carbon [21].

No studies on neutron polarization have been done.

Polarized Λ^0 produced by polarized proton beam [32] shows the same behaviour as unpolarized proton beam production.

Polarized Λ^0 produced by K^- beam [29] shows same sign and higher magnitude than proton beam production.

Polarized Λ^0 studies include pp collider mode [26, 31].

The $\sqrt{(s)}$ dependence is flat in the region $\sqrt{(s)}$=31 to 62 GeV. This energy range is approximately equivalent to 400 and 1600 GeV proton beam on a proton target. The polarization magnitude increases with x_f at constant $p_\perp$. The polarization magnitude increases with $p_\perp$ at constant x_f .

$\bar{\Lambda}^0$ polarization [29] has been measured using anti-proton beam on H_2. The polarization show similar $p_\perp$ dependence as the Λ^0 produced by proton beam.

Zero $\bar{\Lambda}^0$ polarization has been measured using polarized proton beam on fixed target [32].

Sizable Ω^- polarization has been measured using a polarized neutral hyperon beam on fixed target [46, 48, 47]. Fermilab experiment E800 [49] has a $\approx$ 10 times more Ω^- than all previously reported experiments, the data is in analysis stage.

The charm baryon Λ_c^+ polarization has been measured using a π^- beam on Cu [51]. A limit on the charm baryon Λ_c^+ polarization was previously reported [50] using a neutron beam on carbon.

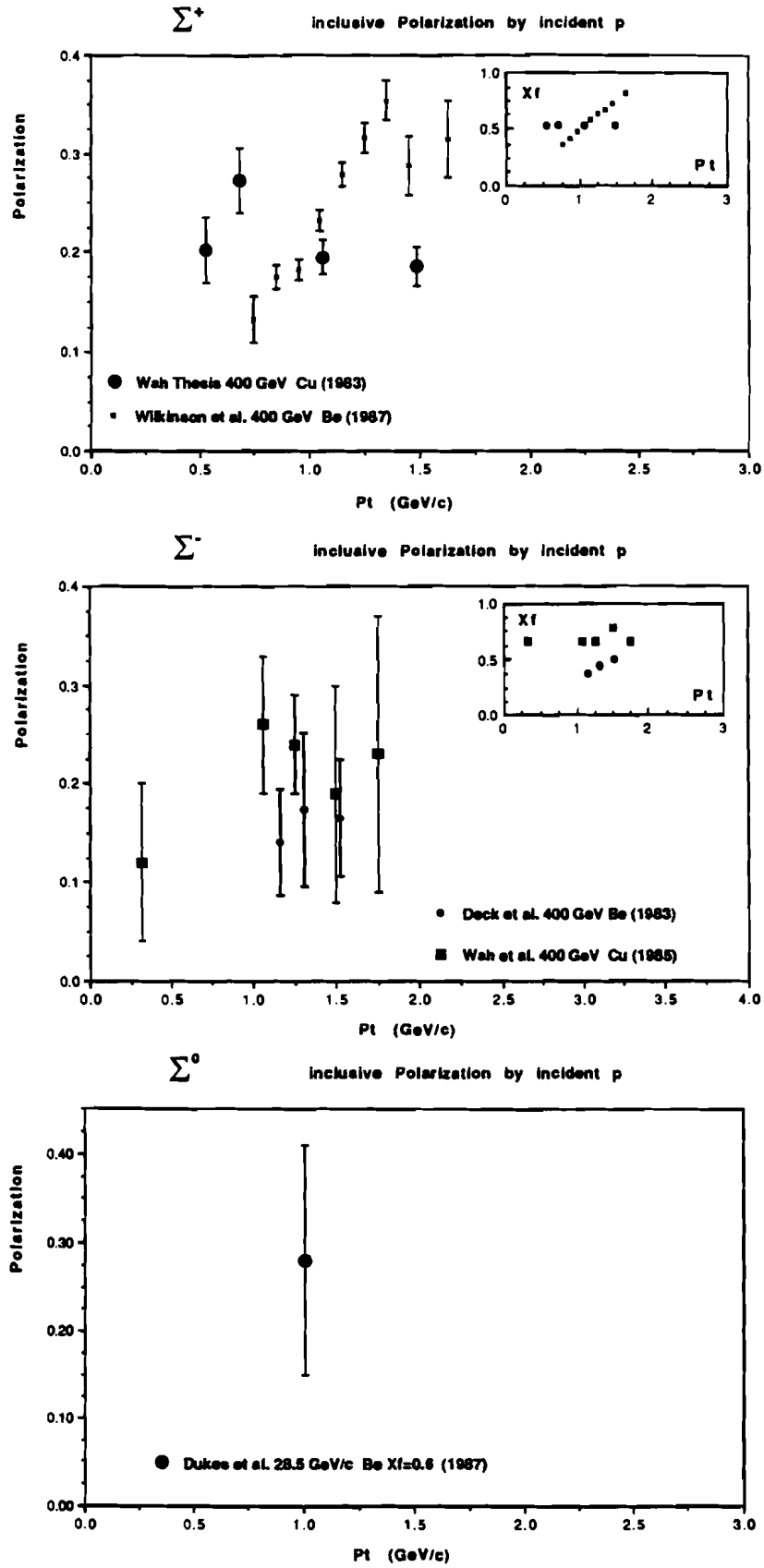

Figure 1.3: Polarization in Inclusive Hyperon Production by Unpolarized Protons on Fix Target, Σ^+ , Σ^- , and Σ^0 .

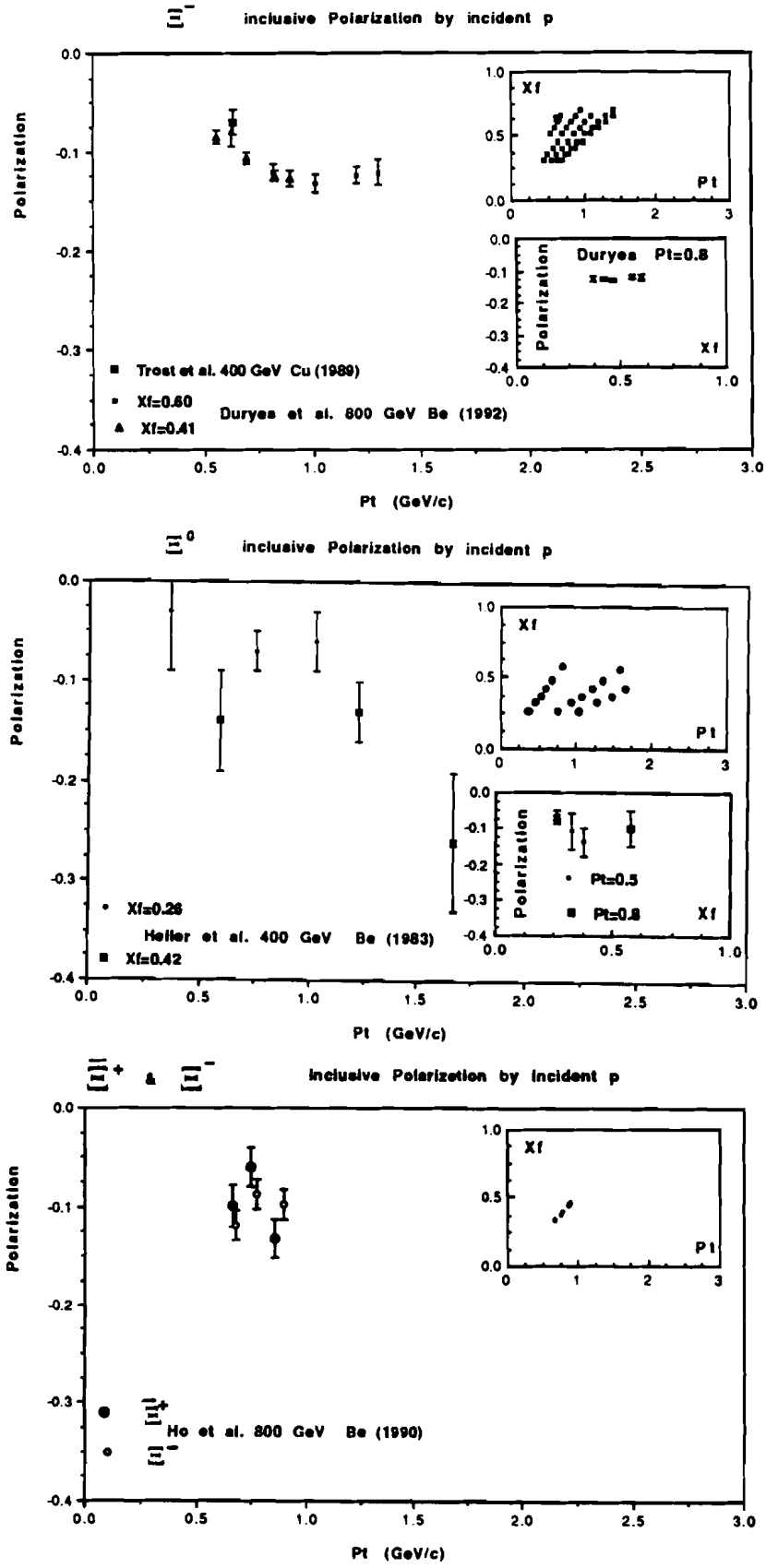

Figure 1.4: Polarization in Inclusive Hyperon Production by Unpolarized Protons on Fix Target, Ξ^- , Ξ^0 , and $\bar{\Xi}^+$.

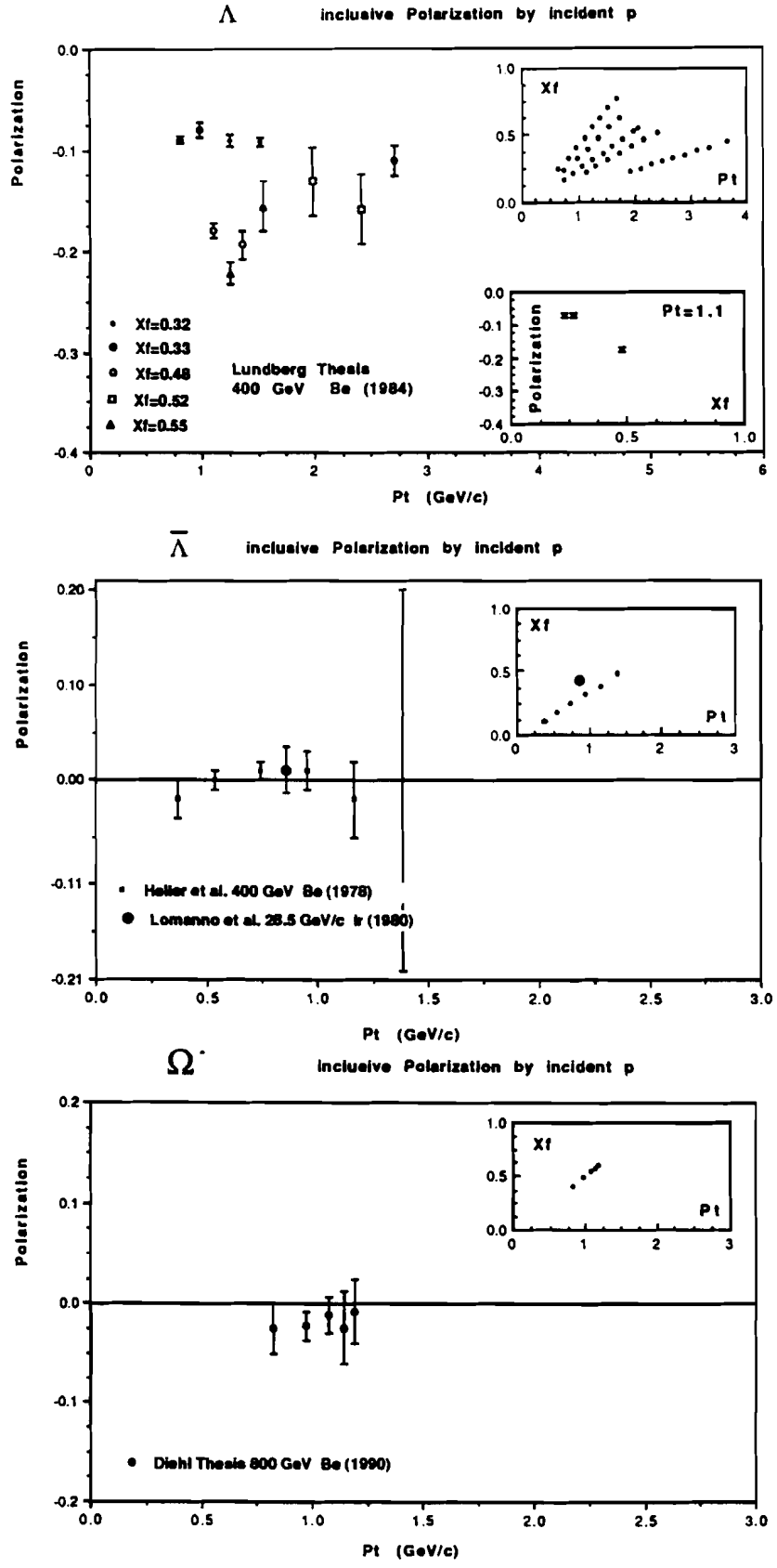

Figure 1.5: Polarization in Inclusive Hyperon Production by Unpolarized Protons on Fix Target, Λ^0 , $\bar{\Lambda}^0$, and Ω^- .

27, 28, 29, 30, 33, 36, 40] . Studies include different target material (A). Reference [33] quotes a polarization ratio of combining Cu and Pb to Be of 0.76 $\pm$ 0.06 on 0.486, 0.473, and 0.497 collision length targets. This result confirms A dependence of the polarization. Experiments cover a wide range of proton energies. Energies go from 12 to 800 GeV and up to the equivalent of 1600 GeV [26, 31] in collider case. All measurements indicate no polarization dependence on the proton energy. All experiments agree that the polarization magnitude increases with x_f at constant $p_\perp$. Also the polarization magnitude increases with $p_\perp$ at constant x_f up to a maximum near $p_\perp$ of 1.0 GeV/c. The polarization becomes constant at high $p_\perp$ [19].

Σ^+ polarization has been measured by three experiments [34, 35] and this thesis. E761 has expanded the amount of polarization data in the kinematical region of $p_\perp$ at fix x_f . Several conclusions from the E761 polarization measurements are found in section 4.

Σ^0 polarization has been reported once [36] at only one point in x_f and $p_\perp$ variables.

Σ^- polarization has been reported twice [38, 39]. The polarization magnitude as a function of $p_\perp$ increases from zero at zero $p_\perp$ to 17 % at 1.5 GeV/c $p_\perp$.

Ξ^0 polarization [40] shows the same kinematic behaviour as the Λ^0 in magnitude and sign. The combined Ξ^0 polarization using Cu and Pb compared to the one using Be indicates no A dependence.

Ξ^- polarization [41, 42, 43] is the second best studied hyperon. Qualitatively the polarization magnitude at 400 GeV proton beam is lower than the one at 800 GeV. Note that the 800 GeV data was made with a 0.22 interaction length Be while the 400 GeV data was with 0.5 interaction length Be. The polarization magnitude is constant as a function of x_f at constant $p_\perp$. The polarization magnitude increases with $p_\perp$ at any x_f up to a maximum near $p_\perp$ of 1.0 GeV/c. There is no conclusive data for $p_\perp$ higher than 1.0 GeV/c.

1.1.2 Polarization Theory

In contrast to the low energy hyperon polarization phenomena [20] the high energy hyperon polarization phenomena has not yet been quantita-

tively described by theory.

Even worse, up to now all existing models can not address anti-hyperon polarization.

At high $p_\perp$ region perturbative quantum chromodynamics (PQCD) predicts zero polarization. Following are two approaches for high $p_\perp$ in chronological order.

In 1978 G.L. Kane et al. [55] using PQCD to order α_s with one and two gluon exchange diagrams calculated the polarization of a scattered or produced quark at large $p_\perp$ predicting zero polarization , see figure 1.6.

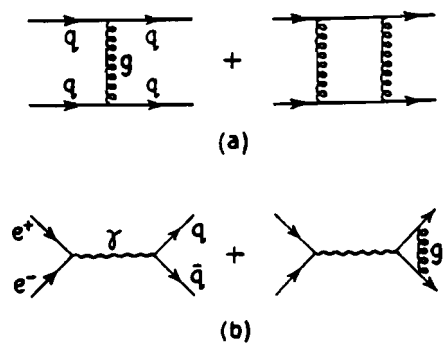

Figure 1.6: Kane: One and Two Gluon Exchange Diagrams.

In 1988 P. Cea et al. [61] focused their attention on Λ^0 assuming it was produced from an interference between a virtual Σ and a resonance Σ^* hyperon states. The model uses a quark-gluon QCD process for the production of Σ and Σ^*. The model predicts negligible polarization.

On the other hand there are a few phenomenological models which attempt to explain the low $p_\perp$ polarization phenomena. I should mention that PQCD does not work in the low energy regime, perturbative higher orders tend to diverge rather than diminish. The models are shown in chronological order in the following lines. Each one has its successful qualitative predictions and its severe limitations.

In 1977 Moriarty et al. [54] focused their attention on Λ^0 showing the contributions due to the various possible t-channel Regge pole exchanges. Comparing against the data the most relevant exchanges are $K^*(890)$ and $K^*(1420)$. The obtained polarization follows the data in the low $p_\perp$ range.

Figure 1.7 shows the model on Λ^0 , data from [22]. (In 1976 Paige et al. [53] using different Regge poles found negligible < 5% Λ^0 polarization).

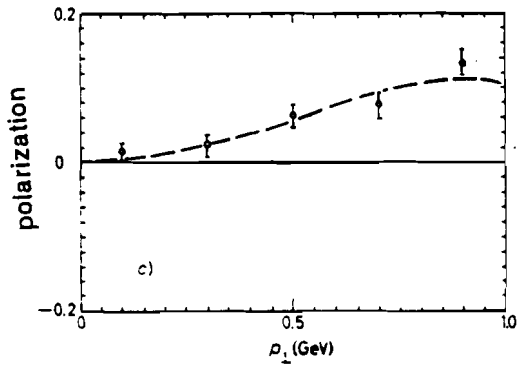

Figure 1.7: Moriarty: Polarization Contribution $K^*(890)$ and $K^*(1420)$ on Λ^0 .

In 1978 Heller et al. [25] proposed a qualitative model that, in the case of Λ^0 , assumes that a u valence quark from the incident proton will scatter off a target nucleus radiating a gluon (gluon bremsstrahlung) producing the s $\bar{s}$ quark pair. If the gluon is polarized then the $s\bar{s}$ will be also. The polarized s will be combined with the spectator diquark ud, assuming the diquark is on a singlet, giving rise to Λ^0 polarization. For the $\bar{\Lambda}^0$ case the $\bar{u}$ and $\bar{d}$ are created from the sea, as well as the $\bar{s}$, at incoherent states such that the net $\bar{\Lambda}^0$ polarization is zero.

In 1981 DeGrand et al. [57] proposed a Thomas precession [9] [10] effect caused by the color field acting upon the quarks or diquarks, s and ud in Λ^0 . The Thomas frequency ($\vec{\omega}_T$) is proportional to $\vec{F} \times \vec{v}$. Assuming the color force points along the same direction as the incident proton then $\vec{\omega}_T$ has the direction of the normal to the hadronic scattering plane $\hat{n} \sim \vec{p}_{p\,incident} \times \vec{p}_{hyperon}$. The Thomas frequency enters into the Hamiltonian as $U_T = \vec{s} \cdot \vec{\omega}_T$. In order to minimize the energy the spin should be opposite to $\vec{\omega}_T$. Since the diquark is in a spin single the spin is given by the quark s, for incident proton then the sign of the Λ^0 polarizations is correctly assigned. The model predicts zero polarization for anti-hyperons. Figure 1.8 shows the model on Λ^0 , for data source see original paper.

[10]Thomas precession is a kinematic effect which arises from the fact that the product of noncollinear boosts is both a boost and a rotation.

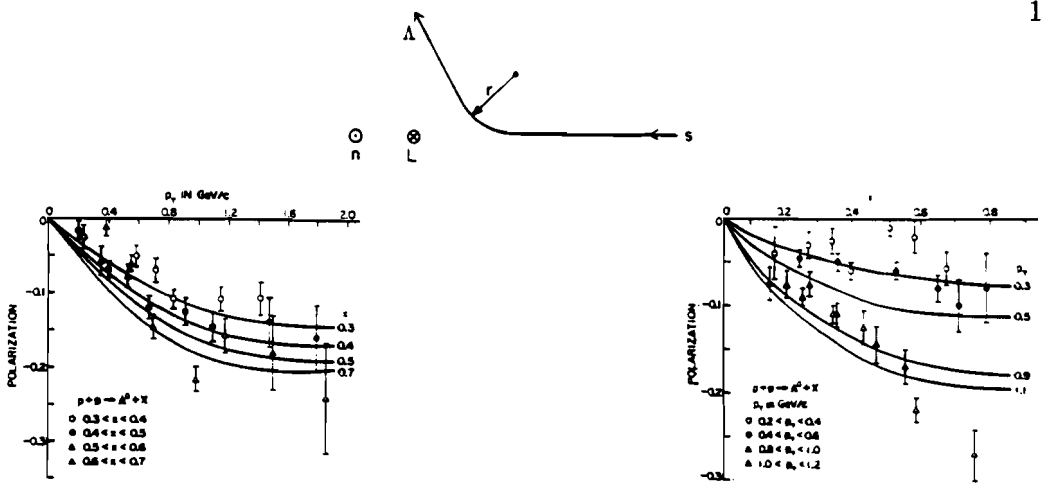

Figure 1.8: DeGrand: Polarization on Λ^0 as a Function of x_f and $p_\perp$.

In 1981 Szwed [58] concentrated on the Λ^0 polarization proposing that the s quark acquires its polarization from multiple scattering in the color field. The procedure is approximated with a simple gluonic field model. This model is able to obtain an analytical expression for the s quark polarization. In 1988 [62] a quantitative Λ^0 polarization comparison was made at low $p_\perp$, with fairly good agreement. Figure 1.9 shows the model on Λ^0 , for data source see original paper.

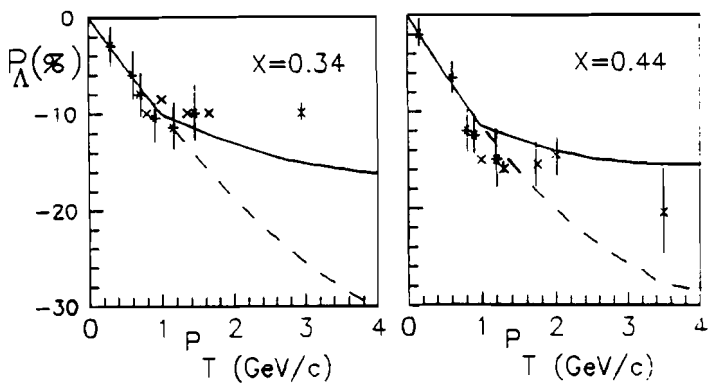

Figure 1.9: Szwed: Polarization on Λ^0 .

In 1983 Andersson et al. (LUND) [59] used a string picture in the color field stretching it to create a pair quark-antiquark (or diquark anti- diquark) and combining it with the valence quarks from the projectile to form the hyperon. The pair is assumed to be produced not point-like but at a distance l. Local angular momentum conservation leads to a preferential spin alignment, $\vec{S} = -\vec{L}$. The LUND model agrees with the hyperon polarization

sign. Originally the model was applied to Λ^0 polarization with a good qualitative comparison with data at low $p_\perp$ in 1979 [56]. Figure 1.10 shows the model on Λ^0 , data from [26].

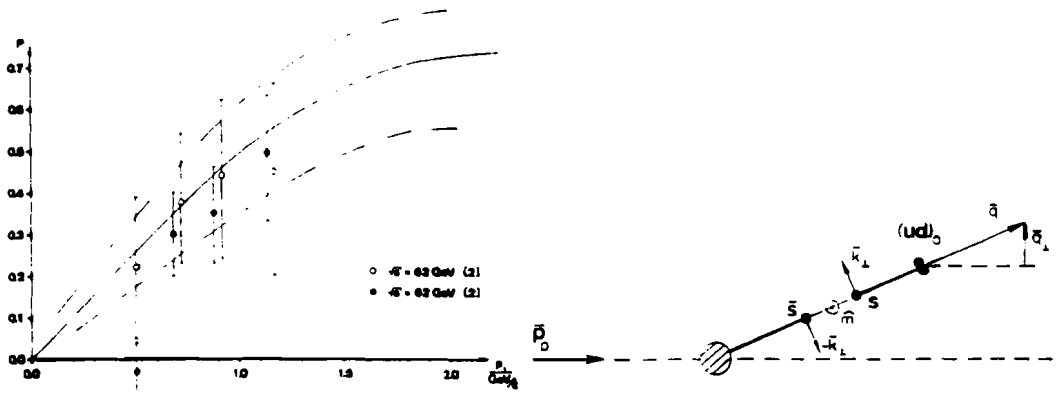

Figure 1.10: Erhan (LUND): Polarization on Λ^0 .

In 1987 Cea et al. [60] focused their attention on high x_f and low $p_\perp$ ($\leq$ $1GeV/c$) inclusive hyperon production, proposing a two step process where hyperon resonance states are produced in the primary interaction and then their decay interference produce the polarized hyperon. The model uses the interference between a virtual Σ and a resonance Σ^* to create the Λ^0 . The production of Σ's came from the interference of Σ^*, Σ, and Λ^0 . The model is compared to Λ^0 polarization data with qualitative agreement. Figure 1.11 shows the model on Λ^0 , and predictions on Σ^+ and Σ^- , for data data source see original paper.

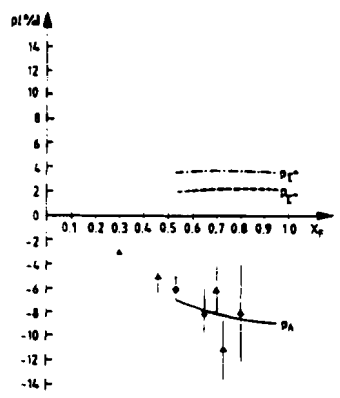

Figure 1.11: Cea: Polarization on Λ^0 , predictions on Σ^+ and Σ^- .

In 1992 Soffer et al. [64] focused their attention on Λ^0 assuming a single pion exchange process in the inclusive reaction $pp \rightarrow \Lambda^0\ K\,X$. In the process to compute the Λ^0 polarization the model uses parameters from the $\pi^-\ p \rightarrow K^0\,\Lambda^0$ cross section and polarization. Figure 1.12 shows the model on Λ^0 , data from [17, 33, 31].

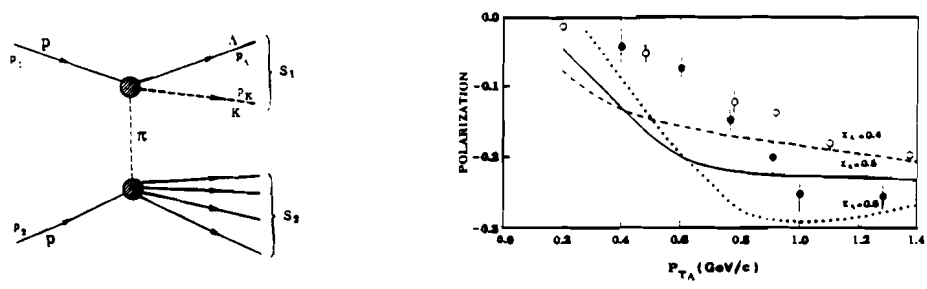

Figure 1.12: Soffer: Polarization on Λ^0 .

As an exceptional case only one model has been able to address the low and high $p_\perp$ range at once with impressive success on Λ^0 .

In 1990 Dharmaratna et al. [63] assuming that a quark pair is produced mainly through gluon fusion $g + g \rightarrow q + \bar{q}$ were able to obtain an analytical expression for the polarized quark. With the polarized s quark, a mechanism to produce hyperons with simple gluon distribution functions was used to describe Λ^0 polarization. Also a linear model to relate $x_{f\ s}$ to $x_{f\ \Lambda}$ is used. Figure 1.13 shows the model on Λ^0 , data from [25, 33, 30].

The major drawback with above models is that they do not state any conclusion about hyperon polarization behaviour other than the Λ^0 . A sizable amount of data, with small error bars, is accessible on Ξ^- , Ξ^0 , and Σ^+ . Nonzero anti-hyperon polarization is now measured. The most promising procedure could be the one of Dharmaratna, since it is adequately able to address the low and high $p_\perp$ range at once.

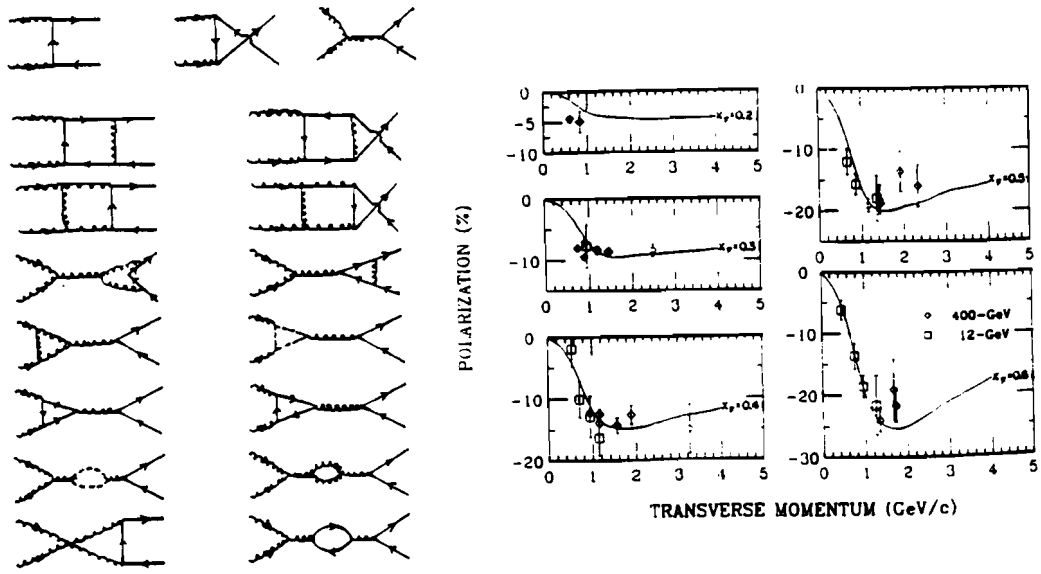

Figure 1.13: Dharmaratna: Polarization on Λ^0 .

1.2 Magnetic Moment

The magnetic moment ($\vec{\mu}$) is an electromagnetic property of non-zero spin ($\vec{s}$) particles. The magnetic moment of a particle can be written as:

$$\vec{\mu} = \frac{g}{2}\frac{q}{mc}\vec{s}$$

where g, q, m, and $\vec{s}$ are the particle's Lande factor (2 for point-like particles), charge [11] , mass, and spin (or intrinsic angular momentum), and c is the speed of light.

[11] For neutral particles the equation still may hold with $q = e$. A more proper definition can be done with the interaction potential term between an external magnetic field and the particles's magnetic moment:

$$\delta E = -\vec{\mu} \cdot \vec{B}$$

or the spin's torque under an external magnetic field, see appendix D:

$$\frac{d\vec{s}}{d\tau} = \vec{\mu} \times \vec{B'}$$

1.2.1 Magnetic Moment Experimental

The magnetic moment of all stable (long-lived) hyperons, including $\bar{\Xi}^+$, and $\bar{\Sigma}^-$ have been measured using the spin precession technique [12] [38, 39, 42, 44, 45, 47] , see appendix D.

The magnetic moment of the p and n have been measured to great accuracy, 0.02 ppm and 0.26 ppm [1] respectively [13] . The stable octect hyperon magnetic moments are at or below the 1 % precision level [14] . The Σ^0 magnetic moment has not been measured. Instead of that the transition magnetic moment $\Sigma\Lambda$ has been measured to a 5 % precision. Two decouplet baryon magnetic moments, Ω^- and Δ^{++} , have been measured to an $\approx$ 10 % precision [15] . Table 1.1 lists the experimental values of the baryon magnetic moments.

The Σ^+ magnetic moment has an experimental discrepancy between two 1 % precision measurements, E620 [35] and E497 [34], which differ by 3 σ. This thesis has a new $\approx$ 1 % precision measurement. Comments will be found in section 4.

The $\bar{\Sigma}^-$ magnetic moment is measured for the first time in this thesis. The magnetic moment of a particle and anti-particle are of equal magnitude but opposite sign by CPT conservation.

---

[12]Other techniques have been used to measure magnetic moments:

Magnetic resonance technique has been used to measure the p and n magnetic moments [18].

Exotic atom technique has been used to measure the $\bar{p}$ and Σ^- magnetic moments [18].

Primakoff method has been used to measure the $\Sigma^0 \rightarrow \Lambda^0\ \gamma$ transition magnetic moment ($\Sigma\Lambda$) [37, 18].

The πp bremsstrahlung technique has been used to measure the Δ^{++} magnetic moment [52].

Spin precession of channeled particles in bent crystals has been observed for the first time in E761 [13]. This technique was used to measure the Σ^+ magnetic moment. This technique may allow magnetic moment measurements of short lived particles in the future.

[13]The quoted number is the ratio of the error over the magnitude of the measurement in parts per million (ppm).

[14]The experimental precision is the ratio of the experimental error over the experimental value in percent.

[15]Fermilab experiment E800 [49] has accumulated Ω^- data for an $\approx$ 2 % precision measurement.

Table 1.1: Experimental Baryon Magnetic Moments.

baryon [1]	μ (μ_N)	σ (μ_N)	precision (%)
p	2.79284739	0.00000006	0.0
n	-1.91304270	0.00000050	0.0
Λ^0	-0.6130	0.0040	0.7
Σ^+	2.4200	0.0500	2.1
Σ^0			
Σ^-	-1.1600	0.0250	2.2
Ξ^0	-1.2500	0.0140	1.1
Ξ^-	-0.6507	0.0025	0.4
Ω^-	-1.9400	0.2200	11.3
Δ^{++} [52]	4.5200	0.6727	14.9
$\Sigma\Lambda$	-1.6100	0.0800	5.0

1.2.2 Magnetic Moment Theory

Magnetic moments provide useful information on the structure of the baryons. In principle, quantum chromodynamics (QCD) is expected to provide the basic formalism to compute the magnetic moments, but at present it is not possible to carry out such QCD calculations. Different QCD inspired phenomenological models attempt to describe the magnetic moments.

Historically, a successes of the naive quark model [16] was the prediction of the hyperon magnetic moments to ≈ 20 % precision [65] [17] . The prediction used as input the n, p, and Λ^0 magnetic moments. That predicted precision has been surpassed by the present octect baryon magnetic moment measurements which are at or below the 1 % precision.

In the naive quark model the SU(6) baryon wave functions are written in terms of the flavor (u, d, and s) and spin quark components. The baryon wave functions are written in table 1.2.

[16]The naive quark model assumes that the constituent quarks do not interact between themselves and they are in a zero orbital angular momentum state (S).

[17]The predicted precision is the ratio of the difference of the predicted value minus the experiment value over the experimental value in percent.

Table 1.2: Baryon SU(6) Spin-Flavor Wave Functions.

baryon	simplified	expanded
$p\uparrow$	$uud\,\chi_{1/2}$	$(2\,u\uparrow u\uparrow d\downarrow - u\uparrow u\downarrow d\uparrow - u\downarrow u\uparrow d\uparrow)/\sqrt{6}$
$n\uparrow$	$ddu\,\chi_{1/2}$	$(2\,d\uparrow d\uparrow u\downarrow - d\uparrow d\downarrow u\uparrow - d\downarrow d\uparrow u\uparrow)/\sqrt{6}$
$\Lambda^0\uparrow$	$uds\,\chi'_{1/2}$	$(u\uparrow d\downarrow s\uparrow - u\downarrow d\uparrow s\uparrow)/\sqrt{2}$
$\Sigma^+\uparrow$	$uus\,\chi_{1/2}$	$(2\,u\uparrow u\uparrow s\downarrow - u\uparrow u\downarrow s\uparrow - u\downarrow u\uparrow s\uparrow)/\sqrt{6}$
$\Sigma^0\uparrow$	$uds\,\chi_{1/2}$	$(2\,u\uparrow d\uparrow s\downarrow - u\uparrow d\downarrow s\uparrow - u\downarrow d\uparrow s\uparrow)/\sqrt{6}$
$\Sigma^-\uparrow$	$dds\,\chi_{1/2}$	$(2\,d\uparrow d\uparrow s\downarrow - d\uparrow d\downarrow s\uparrow - d\downarrow d\uparrow s\uparrow)/\sqrt{6}$
$\Xi^0\uparrow$	$ssu\,\chi_{1/2}$	$(2\,s\uparrow s\uparrow u\downarrow - s\uparrow s\downarrow u\uparrow - s\downarrow s\uparrow u\uparrow)/\sqrt{6}$
$\Xi^-\uparrow$	$ssd\,\chi_{1/2}$	$(2\,s\uparrow s\uparrow d\downarrow - s\uparrow s\downarrow d\uparrow - s\downarrow s\uparrow d\uparrow)/\sqrt{6}$
$\Omega^-\uparrow$	$sss\,\chi^{3/2}_{3/2}$	$s\uparrow s\uparrow s\uparrow$
$\Delta^{++}\uparrow$	$uuu\,\chi^{3/2}_{3/2}$	$u\uparrow u\uparrow u\uparrow$

$$\chi_{1/2} = (2\,\alpha\,\alpha\,\beta - \alpha\,\beta\,\alpha - \beta\,\alpha\,\alpha)/\sqrt{6}$$
$$\chi'_{1/2} = (\alpha\,\beta\,\alpha - \beta\,\alpha\,\alpha)/\sqrt{2}$$
$$\chi^{3/2}_{3/2} = \alpha\,\alpha\,\alpha$$

α and β denote the quark spin third component $+\frac{1}{2}$ and $-\frac{1}{2}$ [2]
The quark symbol together with an arrow
represent the individual flavor-spin state.

With the baryon wave function and baryon magnetic moment operator I can write:

$$\mu = \langle\, b\uparrow |\hat{\mu}_z| b\uparrow \,\rangle$$

where I have selected the spin third component as the quantization axis. The baryon magnetic moment operator is written as the sum of the three constituent quarks as:

$$\hat{\mu}_z = \sum_{q=1,3} \mu_{zq}$$

Table 1.3 list the baryon magnetic moments in terms of the constituent quark magnetic moments using the naive quark model.

After the naive quark model several theoretical attempts have been made to predict the baryon magnetic moments. I made a broad classification into five different categories: Lattice Gauge Theory, QCD sum rules, bag models, potential (excluding bag), and static (none of the above).

- Models based on Lattice Gauge Theory [106, 107]. In reference [106] the largest predicted precision is 20 % on Ξ^- . It requires the p magnetic moment as input.

Table 1.3: Naive Quark Model.

baryon		FIT (μ_N)	difference (μ_N)	precision (%)	deviation (σ exp)
p	$\frac{4}{3}u-\frac{1}{3}d$	2.793	0.000	0.0	8.0
n	$-\frac{1}{3}u+\frac{4}{3}d$	-1.913	0.000	0.0	10.0
Λ^0	s	-0.703	-0.090	14.8	20.0
Σ^+	$\frac{4}{3}u-\frac{1}{3}s$	2.703	0.283	11.7	6.0
Σ^0	$\frac{2}{3}u+\frac{2}{3}d-\frac{1}{3}s$	0.821			
Σ^-	$\frac{4}{3}d-\frac{1}{3}s$	-1.061	0.099	8.5	4.0
Ξ^0	$-\frac{1}{3}u+\frac{4}{3}s$	-1.555	-0.305	24.4	20.0
Ξ^-	$-\frac{1}{3}d+\frac{4}{3}s$	-0.614	0.037	5.6	10.0
Ω^-	$3s$	-2.110	-0.170	8.8	0.8
Δ^{++}	$3u$	5.555	1.035	22.9	2.0
$\Sigma\Lambda$	$-\frac{1}{\sqrt{3}}u+\frac{1}{\sqrt{3}}d$	-1.630	-0.020	1.3	0.3
	u	1.852			
	d	-0.972			
	s	-0.703			

the quark symbol denote the individual magnetic moment
comparison is made to [1]

- Models based on QCD sum rules [86, 98]. In reference [86] the largest predicted precision is 38 % on Ξ^- .

- Bag models [67, 68, 72, 74, 78, 82, 85, 87, 90, 94, 96, 100, 101, 103] have used one or more of the following corrections:
  1.- assign mass to the s quark while u and d are kept at zero,
  2.- quark kinetic energy,
  3.- colour gluon exchange (one gluon exchange),
  4.- orbital configuration mixing,
  5.- relativistic corrections,
  6.- isospin violation,
  7.- pion cloud (pion contributions),
  8.- chiral bag,
  9.- center of mass corrections (recoil),
  10.- quark anomalous magnetic moment,
  11.- photon gluon interaction,
  12.- gluon radiative corrections, and
  13.- Σ^0 Λ^0 wave-function mixing.

In the following lines I mention the magnetic moment predictions which are at the 10 % level. I do not put attention on Ω^- , Δ^{++} , and $\Sigma\Lambda$ magnetic moments which are experimentally at the same 10 % precision level . I quote the largest deviation (excluding p and n) from the experimental value in σ experimental units. Almost all the models do not require magnetic moments as input.

Theberge [85] used number 7 and 9 corrections. The largest deviation is 16.28 σ (6.3 %) on Ξ^- .

Ushio [90] used number 7 and 3 corrections. The largest deviation is 27.72 σ (10.7 %) on Ξ^- .

Krivoruchenko [96] used number 7, 3, 8, 11, and 10 corrections. In this model the p, n, and Λ^0 are inputs. The largest deviation is 23.7 σ (9.1 %) on Ξ^- .

Hogaasen [100] used number 7, 3, 8, 12, and 13 corrections. The largest deviation is 31.72 σ (12.2 %) on Ξ^- .

- Potential models [66, 81, 89, 91, 93, 99, 104, 105] have used one or more of the previous corrections. Almost all the models do not require magnetic moments as input. In reference [93] the largest predicted precision is 15.2 % on the Ξ^- . The precision of the other theoretical approaches are no better than reference [93].

- Static models [69, 79, 70, 71, 73, 75, 76, 77, 80, 83, 84, 88, 92, 95, 97, 102] are characterized by starting from the naive quark model and then add up the above and/or the following phenomenological corrections:
  21.- broken su(3),
  22.- broken su(6),
  23.- quark effective mass,
  24.- decuplet contributions,
  25.- baryon mass, and
  26.- quark effective charge.

  Almost all the models require some magnetic moments as input. In a few cases a fit to all magnetic moments is made. In the following lines I mention the magnetic moment predictions (or fits) which are at the 10 % level. I do not put attention on Ω^- , Δ^{++} , and $\Sigma\Lambda$ magnetic moments. I quote the largest deviation (excluding p and n) from the experimental value in σ experimental units.

  Franklin [88] used number 7, 5, and 13 corrections. The largest deviation is 14.3 σ (9.3 %) on Λ^0 . Relativistic effects on the u and d quarks help

the Ξ^- , 12.3 σ (4.7 %).

Gupta [95] used number 24 correction. The model uses a previous work by Teese [77] which adds to the sum of quark magnetic moments a tensor term coming from decouplet corrections. Teese formalism fail on Σ^- at 13.6 σ (29 %). Gupta realized that an ad hoc sign change in the Σ^- tensor part fixes the Σ^- and keeps all other hyperons in good agreement. Also there is a negligible corrections of $m_u = m_d$. This technique can not go beyond the naive quark model for the decouplet baryons. Table 1.4 shows the fit results to the baryon magnetic moments.

Table 1.4: Gupta: Fit to Baryon Magnetic Moments.

baryon	FIT (μ_N)	difference (μ_N)	precision (%)	deviation (σ exp)
p	2.793	0.000	0.0	2543.5
n	-1.913	0.000	0.0	85.4
Λ^0	-0.612	0.001	0.2	0.3
Σ^+	2.397	-0.023	1.0	0.5
Σ^0	0.638			
Σ^-	-1.122	0.038	3.3	1.5
Ξ^0	-1.250	0.000	0.0	0.0
Ξ^-	-0.677	-0.026	4.0	10.5
Ω^-				
Δ^{++}				
$\Sigma\Lambda$	-1.524	0.086	5.3	1.1
u	1.760			
d	-0.878			
s	-0.612			
comparison is made to measurements [1]				

Verma [97] used number 26 correction. The largest deviation is 18.2 (11.9 %) on Λ^0 . The effective charge effect on the Ξ^- is 3.72 σ (1.4 %). The model used Ξ^0 as input.

After the naive quark model by Franklin in 1968, the most promising corrections are: pion contributions and gluon contributions. All other effects do not play a striking role, or by basic principles should be able to compute the corrections from pion and gluon effects. The tensor model of Gupta gives the best fit by far but lacks from a justification of the tensor elements.

Chapter 2

Experimental Setup

2.1 Introduction

Experiment E761 was performed in the fixed Proton Center beam line at Fermilab. A brief description of the Fermilab accelerator is given in appendix A.

E761 was a high resolution apparatus to study charged hyperons. Figure 2.1 shows the full E761 apparatus layout. Polarization and magnetic moment measurements of Σ^+ and $\bar{\Sigma}^-$ make use of the decays $\Sigma^+ \rightarrow p\pi^0$ and $\bar{\Sigma}^- \rightarrow \bar{p}\pi^0$. The only experimental difference in these decay modes was the polarity change of all the spectrometer magnets to keep the particles within the apparatus acceptance. The apparatus was designed to detect decays which occurred in a region of 1200 *cm* starting from the last hyperon tracking station. Subsequently the decay products are named baryon and neutral. The baryon is p or $\bar{p}$. The neutral is π^0 , since the π^0 life-time is $10^{-16} sec$ and 99 % of its decays are $\pi^0 \rightarrow \gamma\ \gamma$ [1], so the actual neutral we detected was one or two γ's. A goal of E761 was to achieve a good neutral mass resolution with high angle and momentum resolutions for the hyperon and baryon. As explained in section 1.1 the polarization is controlled by the angle between the incident proton beam and the hyperon at the target.

The E761 apparatus is divided into four parts; hyperon production, hyperon spectrometer, baryon spectrometer and photon spectrometer.

- Hyperon production consists of an initial proton beam from the Fermilab accelerator which produces a polarized hyperon beam at the target. The elements of this section are the incident proton beam line, the target and

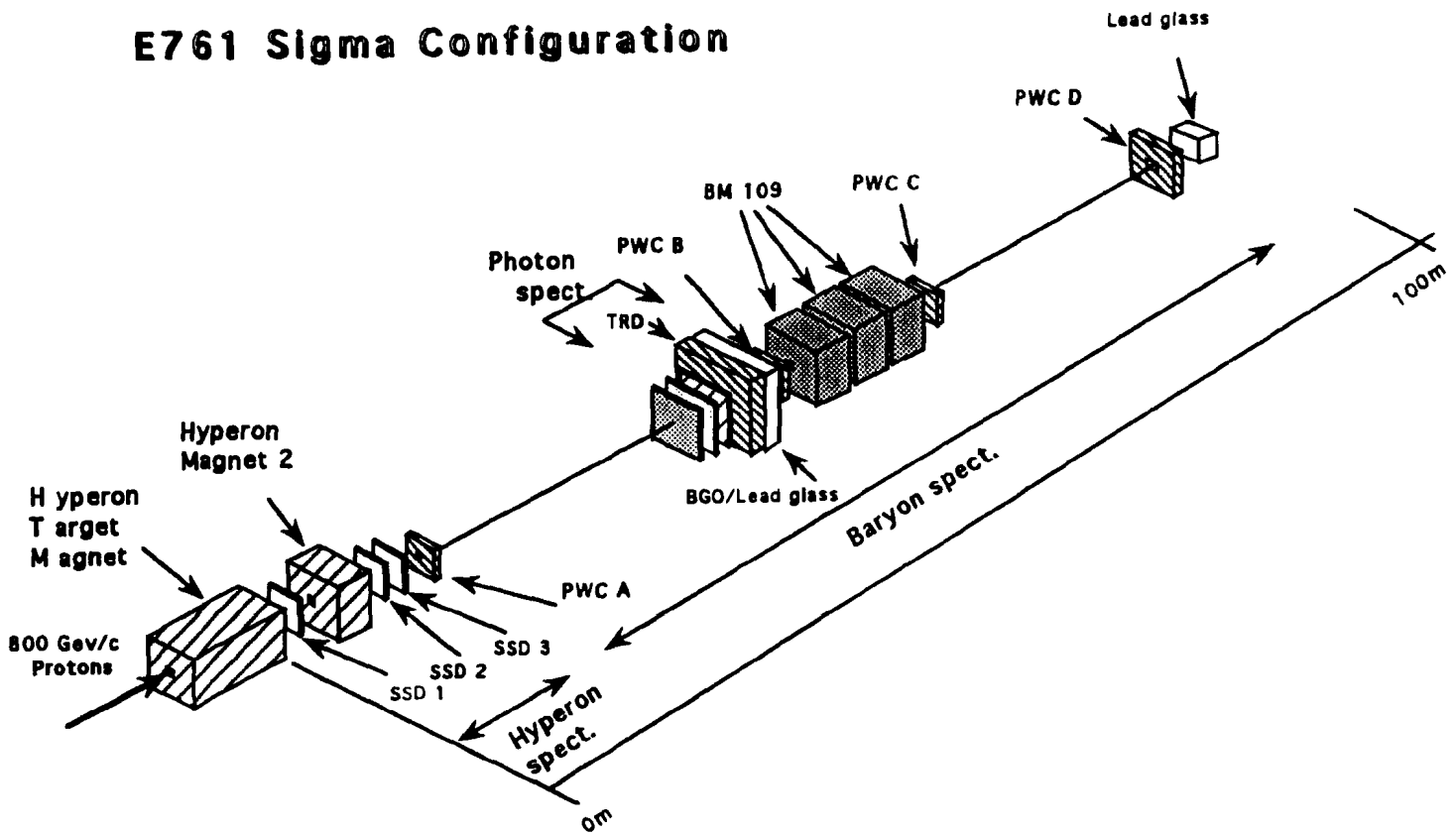

Figure 2.1: E761 Apparatus Geometry.

a channel collimator embedded in a vertical magnetic field, produced by the hyperon target magnet (HTM).

- The hyperon spectrometer measures the hyperon position and momentum using silicon strip detectors (SSD) and a dipole magnet. The algorithm relating momentum, angle, and position to silicon strips and magnetic field is explained in the appendix B.
- The baryon spectrometer measures the baryon position and momentum using proportional wire chambers (PWC) and three dipole magnets.
- The photon spectrometer measures the photon energy and position. This spectrometer consisted of an electromagnetic calorimeter (EC) and transition radiation detectors (TRD).

The trigger was the simultaneous detection of a charged particle going through the hyperon spectrometer, a charged particle going through the baryon spectrometer, and a signal from the photon spectrometer. The trigger was defined by scintillators [1] installed in each spectrometer.

The data acquisition system (DAQ) collected the signals from the apparatus with CAMAC [2] readout electronics. At the same time data was taken the ACP [3] made online event reconstruction. From the ACP all data were written onto tapes and part was sent to a memory pool for monitoring and debugging purposes.

Figure 2.1 shows the full E761 apparatus layout. The coordinate system was arranged such that:

[1] Scintillator or scintillator counter is a piece of scintillating material optically coupled to a photomultiplier. As a high energy particle passes through the scintillator, it excites the atoms which produce light. The time response of scintillator materials is a few *ns*. A discriminator transforms the analog phototube signal into a logic pulse which indicates the passage of a charged particle.
For an introduction to experimental particle physics techniques see references [6, 7, 8].

[2] CAMAC is a protocol to transfer digital information between electronic modules. The protocol sets regulation on the mechanical and electronic design. CAMAC stands for: Computer Automated Measurement and Control.

[3] ACP is the name of a modular parallel computer developed at Fermilab. ACP is based on M68020 CPU. ACP stands for Advanced Computer Program.

$+\hat{z}$ pointing downstream,

$+\hat{y}$ pointing to sky, and

$+\hat{x}$ completes a right handed coordinate system.

Axis x ended up pointing approximately west. The $+\hat{z}$ axis was selected to be approximately parallel to the average hyperon beam trajectory after the exit of HTM.

In the following sections I describe each of the E761 apparatus components.

2.2 Hyperon Production

Hyperons are produced by the inclusive reaction:

$$p + N \rightarrow hyperon + X$$

where: N is a nucleon and X represents all other particles produced with the hyperon.

In this reaction a hyperon s quark, as any anti-quark, should be produced from the available center of mass (CM) energy at production point. The incident proton momentum was 800 GeV corresponding to 40 GeV CM energy. The s quark constituent mass is 0.5 GeV/c^2 [1] [4] and is also the heaviest of the quarks inside a hyperon. Thus, the E761 CM energy was well above the amount needed to produce a high energy, long lived hyperon beam in the laboratory system. Figure 2.2 sketches a naive hyperon production model.

The products of $p + N$ interactions include more variety of particles than just hyperons. Figure 2.3 shows the beam fractions at 10 m from the target with 800 GeV incident protons. Values were extrapolated from 400 GeV data [10]. Notice that Σ^+ is 1.5% of the total beam flux.

[4]The constituent quark masses are computed from the naive quark model. It assumes non-interacting quarks. The constituent masses are found to be 0.338, 0.322, and 0.510 GeV/c^2 [1] for the u, d, and s quark respectively.

The current quark masses are estimated from more complete models. The current masses are approximately 0.006, 0.010, and 0.199 GeV/c^2 [1] for the u, d, and s quark respectively.

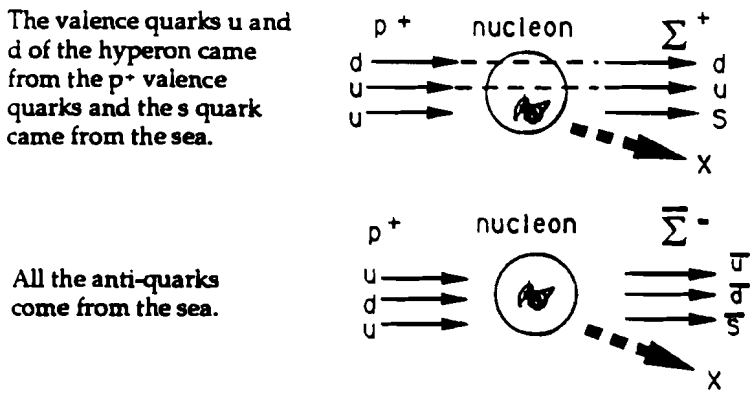

Figure 2.2: Naive Σ^+ and $\bar{\Sigma}^-$ Production.

From section 1.1 equation 1.1, the hyperon polarization is related to the cross product:

$$\vec{\mathbf{P}} \sim \vec{p}_{p_{incident}} \times \vec{p}_{hyperon} \tag{2.1}$$

To control this simple reaction we needed three components: the proton beam, the target, and the HTM. The different parts are described in the following sections.

2.2.1 Beamline

Before any description I define the targeting angle as follows:

- The targeting angle is the angle between the incident proton ($\vec{p}_{p_{in}}$) and the produced hyperon ($\vec{p}_{hyperon}$) at the target.
- Horizontal (H) mode is when $\vec{p}_{p_{in}}$ and $\vec{p}_{hyperon}$ lie on the x-z plane [5] .

[5] Horizontal mode produced hyperon polarization parallel to $\hat{y}$. The polarization vector was kept fixed while the hyperon traveled through E761 apparatus until it decays. Horizontal positive targeting angles produced Σ^+ polarization vector pointing along $-\hat{y}$. This mode was used to gather data for polarization studies.

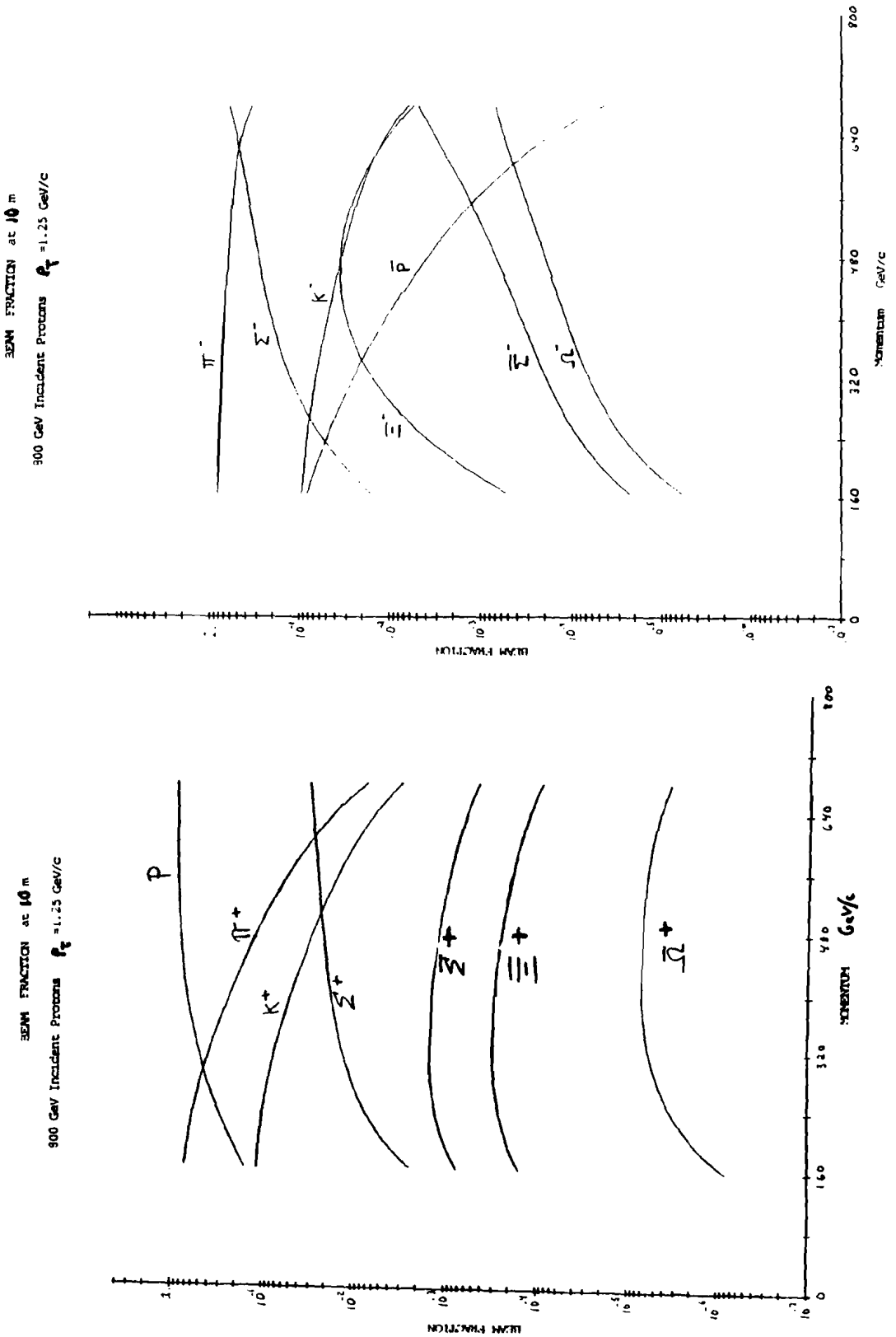

Figure 2.3: Estimated Beam Fractions at 10 m from the Target with 800 GeV Incident Protons.

- Vertical (V) mode is when $\vec{p}_{p_{in}}$ and $\vec{p}_{hyperon}$ lie on the y-z plane [6] .
- E761 targeting angle sign [7] can be expressed as follows:

$$\underline{\text{positive}} \text{ targeting angle if}$$
$$\vec{p}_{p_{in}} \times \vec{p}_{hyperon} \text{ points along } -\hat{y} \text{ for horizontal mode (H)}$$
$$\vec{p}_{p_{in}} \times \vec{p}_{hyperon} \text{ points along } +\hat{x} \text{ for vertical mode (V)}$$

Section 3.5 has the actual values of the targeting angles. There were 28 different combinations of targeting angle, mode (H or V), and hyperon beam charge.

The primary beam line was composed of protons at 800 GeV. The incident proton intensity was set accordingly to the targeting angle, see table 2.1. The intensity is given in ppp (protons per pulse) units. The pulse was composed of 21 *seconds* of proton beam followed by 39 *seconds* empty lapse (spill). The intensity was tuned to achieve 100 kHz of particles at the HTM exit.

To sustain a nonzero $\vec{\mathbf{P}}$ the proton beam line was steered while the hyperon beam was fixed by the geometry of the HTM. E761 used a set of dipole magnets to vary the targeting angle. It was possible to vary the incident proton beam angle by $\pm$ 6 $mrad$. Figure 2.4 sketches the proton beam line. Table 2.1 lists the dipole magnets.

The beam line was set for positive and negative targeting angles alternately. These independent setups produced polarization in opposite directions. A set of symmetric targeting angle data help us to cancel the apparatus acceptance. The polarization measurement section 3.6.1 explains in detail the use of symmetric targeting angle data.

[6] Vertical mode produced hyperon polarization parallel to $\hat{x}$ at the interaction point. The polarization vector precessed while the hyperon traveled through the HTM and HYPE2 magnetic fields. Vertical positive targeting angles produced Σ^+ polarization vector pointing along $+\hat{x}$. This mode was used to gather data for the magnetic moment measurement.

[7] This collaboration defined positive horizontal targeting angle if the incident proton points into the positive x-z quadrant. In the same spirit positive vertical targeting angle has the incident proton pointing into the positive y-z quadrant.

Table 2.1: Proton Beam Intensity and Beam Dipole Magnets.

Positive Hyperon Beam							
Horizontal Targeting Mode							
nominal targeting angle		run	proton beam intensity 10^{10} ppp	Beam Dipole Magnets (*Amps*)			
				PC3H1	PC3V	PC3BR	PC3H2
HPB	-6.0	2429	111.976	-930.6	52.5	1622.5	1258.7
HPB	-5.5	2425	104.688	-900.6	51.9	1621.3	787.5
HPB	-5.0	2421	87.584	-868.5	51.9	1620.0	316.4
HPB	-4.5	2417	32.280	-837.6	52.2	1620.0	130.1
HPB	-2.0	2409	2.032	-426.6	52.2	772.5	895.1
HPB	-1.0	2334	1.016	-207.9	30.6	388.8	-895.1
HPB	0.0	2407	2.176	2.4	51.9	-2.5	-895.1
HPB	+1.0	2411	3.544	215.7	52.2	-392.5	-895.1
HPB	+2.0	2413	8.104	422.4	52.5	-773.8	-895.1
HPB	+2.5	2415	33.040	536.7	49.5	-986.3	-895.1
HPB	+3.0	2419	74.696	642.9	51.9	-1198.8	-895.1
HPB	+3.5	2423	107.352	727.2	51.9	-1411.3	-1092.2
HPB	+4.0	2427	0.192	809.1	54.3	-1622.5	-1287.9
Vertical Targeting Mode							
VPB	+3.0	2477	14.208	-40.2	832.5	1286.2	-8.6
VPB	0.0	2496	1.184	-45.0	46.2	7.5	-9.5
VPB	-3.0	2486	14.520	-39.9	-719.1	-1288.7	-9.5
Negative Hyperon Beam							
Horizontal Targeting Mode							
HNB	-4.0	2030	105.288	-824.7	51.1	1620.0	-269.1
HNB	-3.0	2031	90.344	-653.4	49.8	1196.3	-602.1
HNB	-2.0	2032	7.424	-434.4	50.1	777.5	-602.6
HNB	-1.0	2136	4.648	-225.6	-49.8	390.0	-602.1
HNB	0.0	2132	9.368	-12.3	49.8	1.3	-602.1
HNB	+1.0	2143	19.384	204.9	50.1	-388.8	-602.1
HNB	+2.0	2147	72.016	410.1	49.8	-770.0	-602.1
HNB	+3.0	2149	74.640	632.1	49.8	-1193.8	-602.1
HNB	+4.0	2152	72.040	786.9	50.1	-1620.0	-918.5
Vertical Targeting Mode							
VNB	-3.0	2497	69.112	-55.8	817.5	1272.5	288.0
VNB	0.0	2515	4.152	-55.8	50.1	1.3	288.0
VNB	+3.0	2498	99.720	-54.0	-738.6	-1308.8	288.0

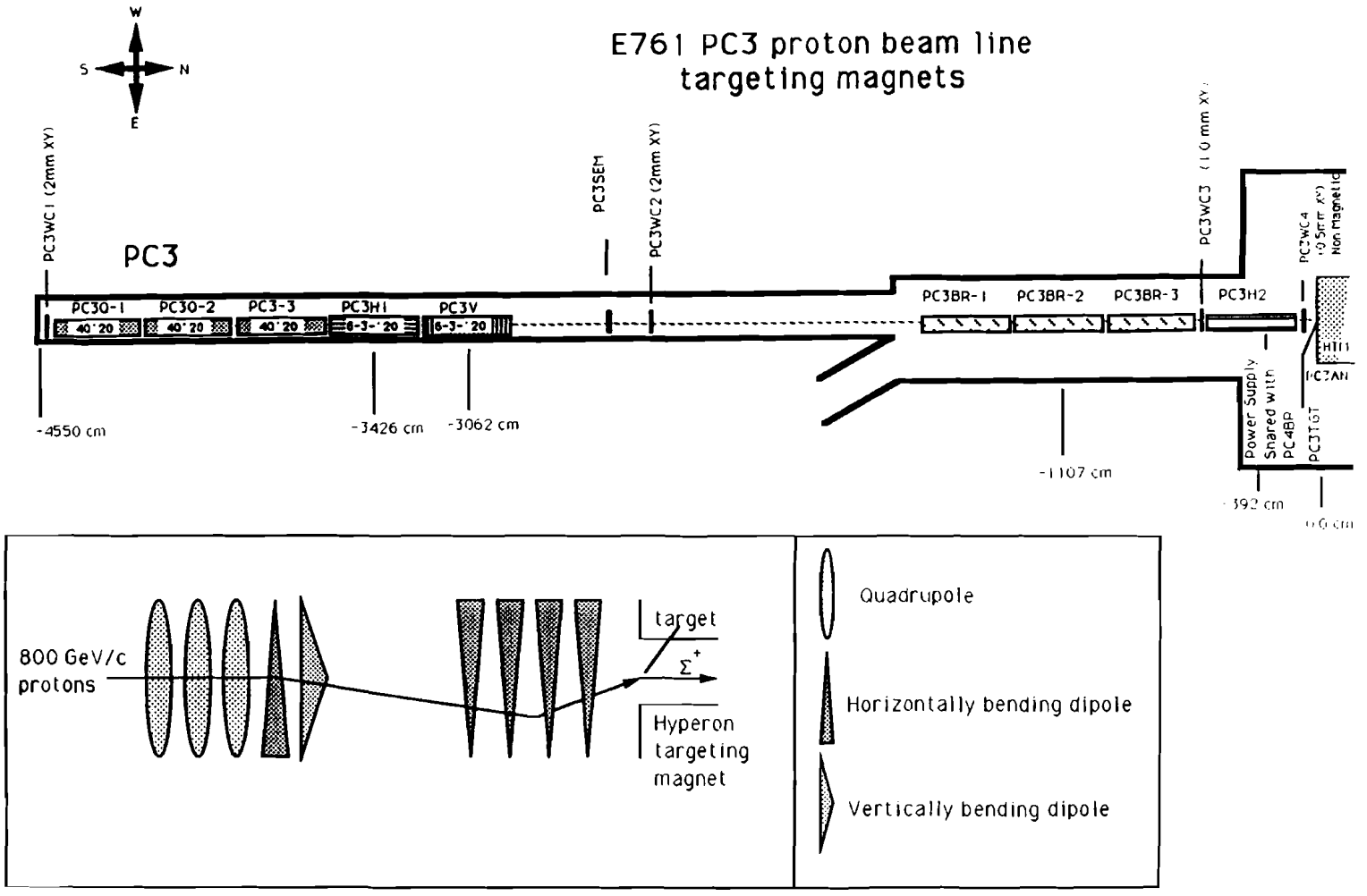

Figure 2.4: Proton Beam Layout.

Figure 2.5 shows two computer generated proton beams. One is a mode we call nominal +3.0 horizontal targeting mode. The other shows what we call nominal +3.0 vertical mode. The pictures are shown in a coordinate system where the $+\hat{z}$ axis is parallel to the design average incident proton ray when the dipoles are set to zero.

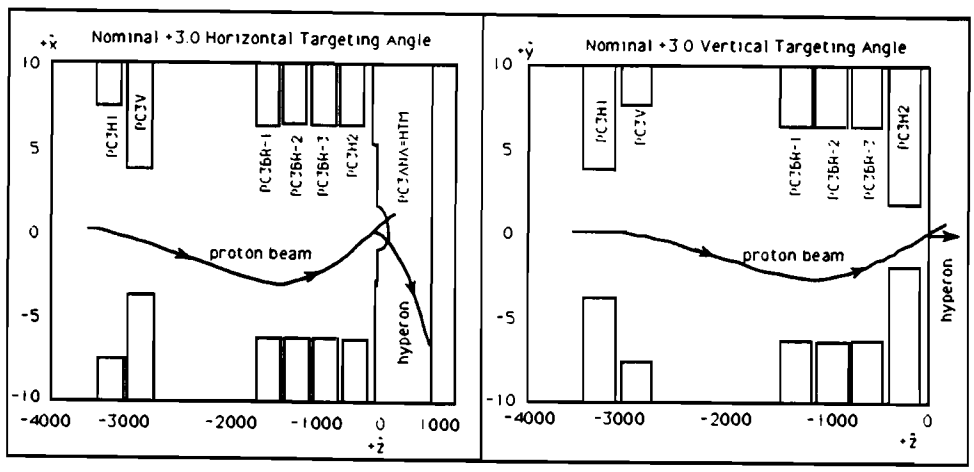

Figure 2.5: Proton Beam at +3.0 *mrad* Horizontal and Vertical Mode.

In the proton beam line there were focusing quadrupole magnets to achieve a beam spot to match the target size. The beam at the upstream target face was 0.13 *mm* in x (σ), 0.21 *mm* in y (σ), 0.34 *mrad* angular dispersion in x (σ), and 0.08 *mrad* angular dispersion in y (σ). These numbers were obtained from the design TRANSPORT [8] output sheet.

2.2.2 Target

We used a 0.58 *mm* in x, 1.98 *mm* in y, by 1 interaction length (15.06 *cm*) in z copper target.

Copper material selection was made because it is easy to use. At one

[8]TRANSPORT is a Fermilab standard program to generate and transport a particle beam through different magnet configurations.

time beryllium was considered as an alternate because it produces 10 % more polarization than copper [17, 34, 35, 33], but the interaction length is double that of copper.

This small x size was needed to improve the momentum and angular resolution [9] for mass separation of the decays $\Sigma^+ \rightarrow p\pi^0$ and $\Sigma^+ \rightarrow p\gamma$. There was no required condition on the target y width. The target length is one interaction length to achieve 60 % beam interactions.

Figure 2.6 is a target sketch. The target was located at the HTM entrance.

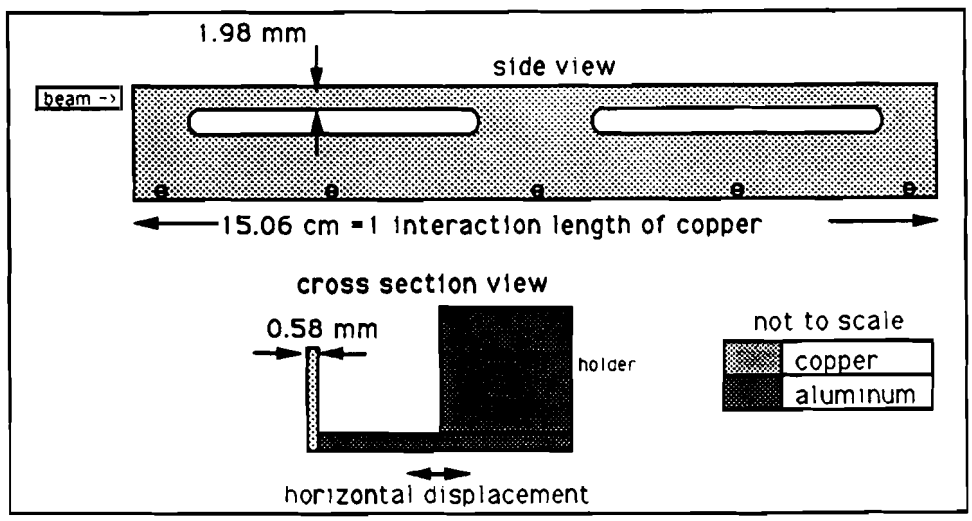

Figure 2.6: E761 Target Sketch.

2.2.3 Hyperon Target Magnet (HTM)

The HTM can be described as a 350 m radius curved channel with tungsten walls embedded in a magnetic field created by a 7.31 m iron dipole

[9] Appendix B shows the fitting algorithm referencing SSD strips and PWC wires. To include the target just add a plane at the target position with one wire in x and one wire in y.

magnet [11] (figure 2.7). The magnetic field is parallel to y axis. The combination of $\vec{B}$ field and channel geometry selected the hyperon momentum and hyperon charge.

The solid angle spread of the hyperon beam exiting the HTM is 0.62 $\mu sterad$. The momentum spread $\Delta p/p$ is 7% (FWHM [10]). The horizontal angle spread is less than 0.001 (FWHM) rad. The magnet was operated at 3230 $Amps$ producing a 3.46 kG field; figure 2.8 shows the magnetic field map at 3230 $Amps$.

The effective $\int B\,dl$ from target center to first hyperon tracking station was 25.1 $T \cdot m$, producing a -7.5 GeV/c momentum deflection (Ptk [11]). Section 3.5 has the HTM Ptk by targeting angle. The Ptk sign was the same for positive and negative hyperons due to the fact that the current polarity was reversed. At this field strength, particles with an average 377 GeV/c momentum were transported through the channel.

Before leaving this section a feature on the horizontal targeting angles is described. The horizontal targeting angle could not be freely varied. There are certain horizontal targeting angles given by the channel geometry and HTM field (or transported hyperon momentum) such that non-interacting beam protons strike into the channel neck. This interaction causes an increase in the non-hyperon flux at the exit of the channel. At this targeting angle the hyperon beam has a bad quality. The forbidden targeting angles are different for positive and negative charged hyperons. Figure 2.9 shows the forbidden targeting angles.

2.3 Hyperon Spectrometer

[10] FWHM stands for Full Width at Half Maximum.

[11] Ptk is the momentum deflection of a charged particle after crossing a magnetic field. It is measured perpendicular to the original entrance direction. Ptk does not depend on the magnitude of the momentum.

$$\mathbf{Ptk} = \frac{1}{1.602 \cdot 10^{-3}}\, q \int B\,dl$$

$$[\mathbf{Ptk}] = GeV/c,\ [q] = esu,\ [B] = gauss,\ [l] = cm$$

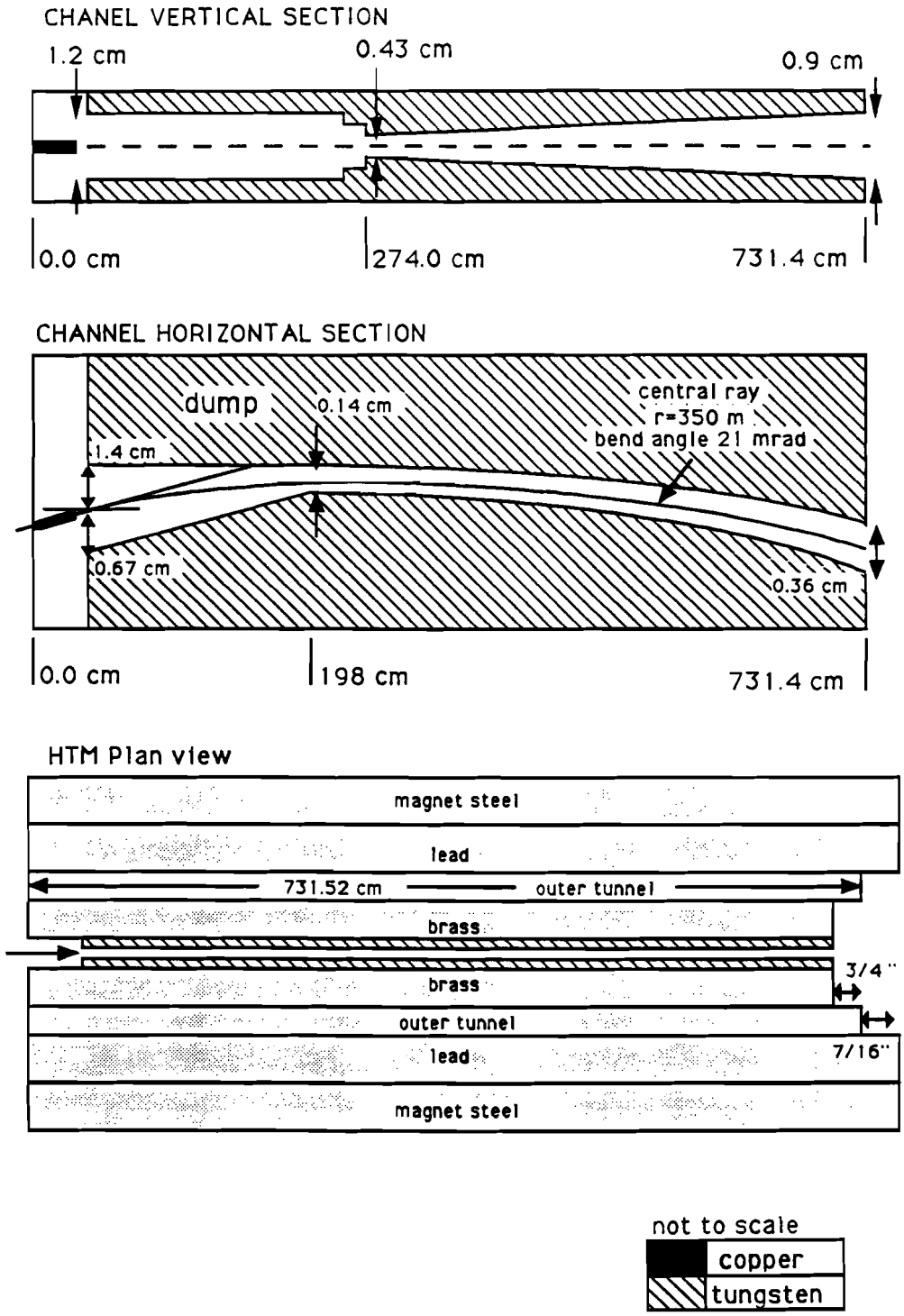

Figure 2.7: Hyperon Target Magnet and E761 Tungsten Channel.

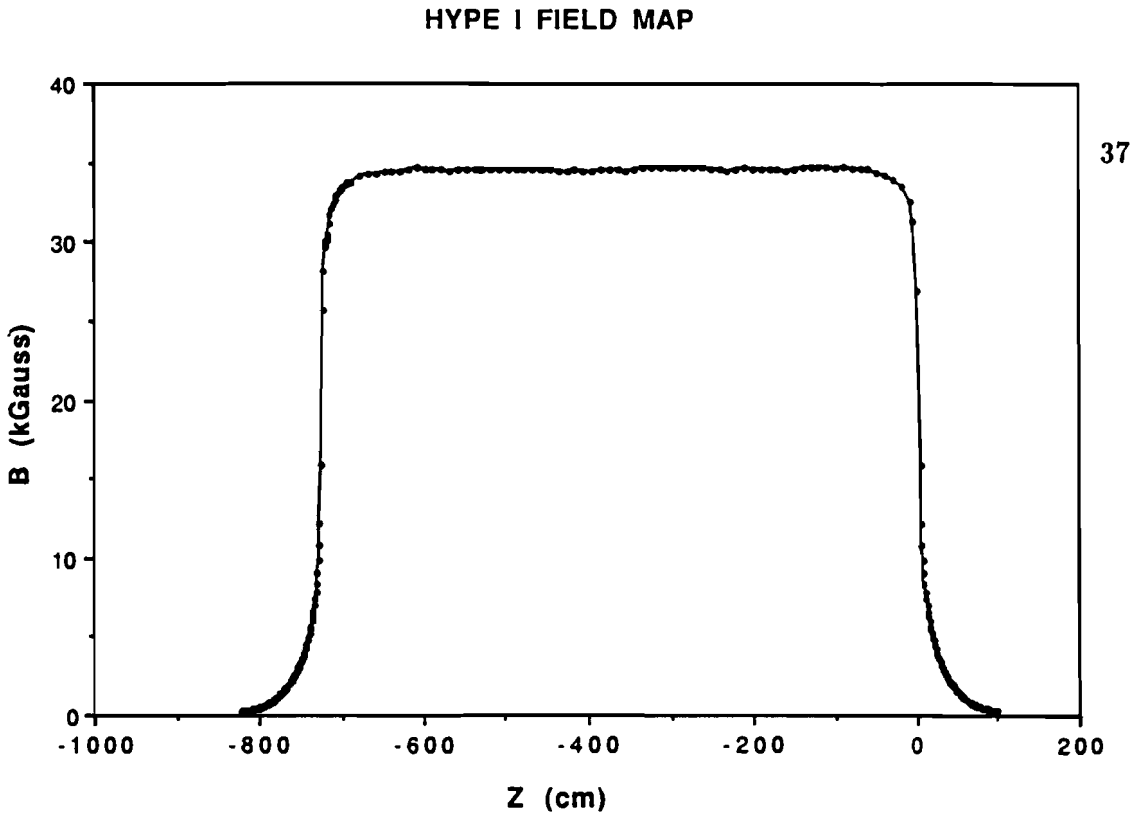

Figure 2.8: Hyperon Target Magnetic Field Map at 3230 *Amps* .

Once the 377 GeV/c hyperon polarized beam is defined (Σ^+ or $\bar{\Sigma}^-$), the next step is to measure the hyperon momentum vector and position.

Since Σ^+ ($\bar{\Sigma}^-$) have a mean life-time of $\approx 10^{-10}$ sec (7.5 m in the laboratory system at 377 GeV/c), a decision was made to make the separation between detectors as short as possible to track most of the hyperons before they decay. At the same time, we required a high momentum and angle resolution for the hyperon track.

The hyperon spectrometer consisted of three silicon strip detector (SSD) stations and a dipole magnet. The angle resolution is 10 μrad (σ), the position resolution is 13 μm (σ), and the momentum resolution is 0.7 % (σ). The momentum is measured in the x-z plane. The vertical momentum component is negligible compared to its full value and its resolution.

Figure 2.10 shows the hyperon spectrometer. The following sections describe each part of the spectrometer.

2.3.1 Silicon Strip Detector (SSD)

A SSD is a plane of metallic strips etched on a silicon wafer. The strips are in only one direction. Every strip is an independent position mea-

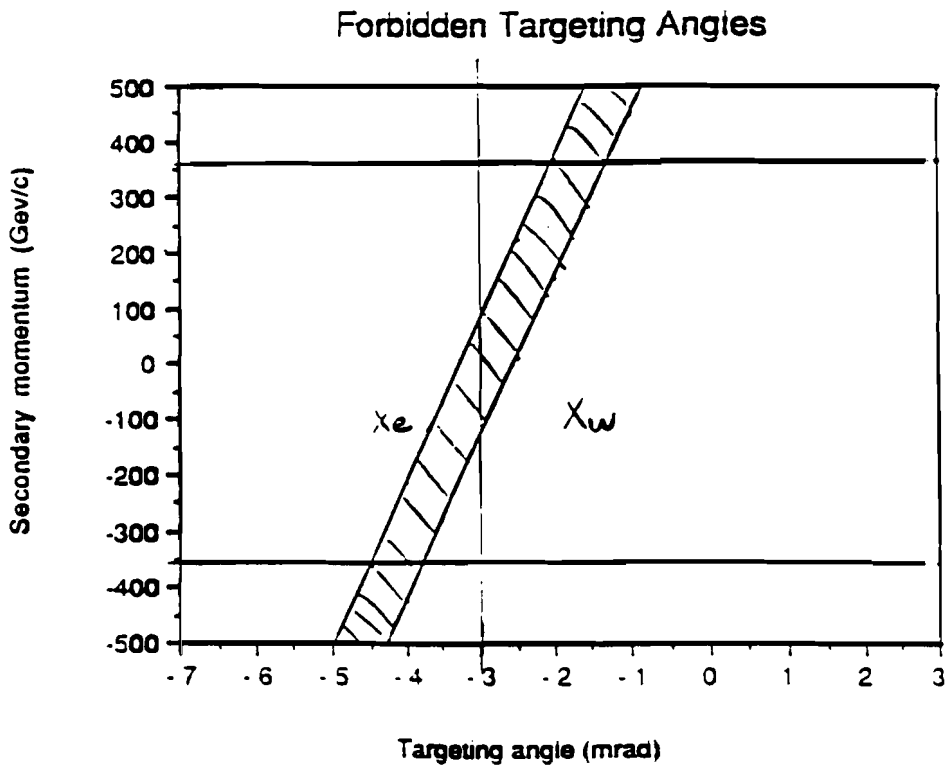

Figure 2.9: Horizontal Forbidden Targeting Angles.

surement. When a high energy charged particle [12] crosses the silicon it produces an electron-hole pair. The strips collect the charge. The collection of the charge was made possible through a high voltage (60 V) difference between the strips and a cathode plane. Electronics attached to the strips convert the signal into a hit position.

There were three silicon strip detector stations, SD1, SD2, and SD3. Every station had 3 separate silicon planes. The planes measure x, y and u coordinates respectively. The u axis was rotated 45^0 from the vertical around the z axis. To measure x position the strips were oriented vertically; the proper orientations were made to measure y and u. All silicon planes were 50 μm pitch.

[12]Charged particles lose energy when passing through a material. The shape of this energy loss [1, 6, 7] ($\frac{dE}{dx}$) is a function of the particle velocity and the material. The energy loss as a function of $\beta\gamma$ has a minimum energy loss close to 3 units [7]. The minimum energy loss is in the range of 1 to 10 $MeVcm^2/g$. Above this point there is a soft relativistic rise on the energy loss. In terms of the momentum of the particle the energy loss has the minimum at $\approx 1.0\ GeV/c$. Charged particles in the momentum range of the minimum energy loss are called *minimum ionizing particles.*

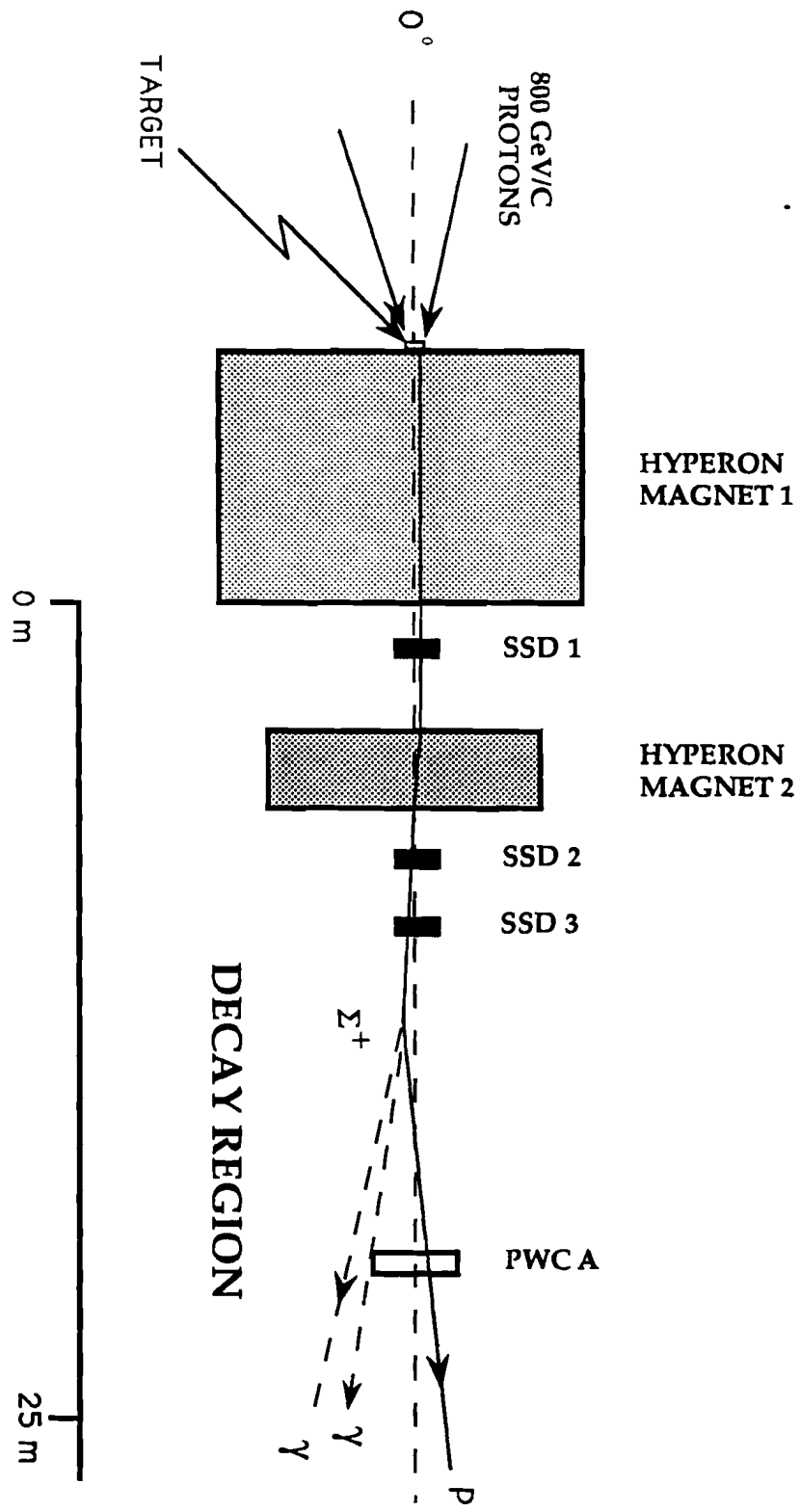

Figure 2.10: Hyperon Spectrometer.

2.3.2 Hyperon Dipole Magnet (HYPE2)

HYPE2 was a dipole magnet with full aperture of 35.56 x 3.81 x 182 cm^3. The magnetic field was parallel to the y axis.

The magnet was operated at 1520 *Amps* producing a 26 kG field. The effective $\int B\,dl$ from SD1 to SD3 was 4.77 $T \cdot m$ producing a +1.4243 GeV/c Ptk . The magnet polarity was reverse with respect to the hyperon target magnet. The Ptk sign was positive regardless of the hyperon charge since the current polarity was changed. The field was uniform to 0.1 % in a 2.0 cm horizontal center range. The widest horizontal hyperon beam size at the exit of HYPE2 was 1.75 cm. The field was found to be uniform to 0.14 % (ΔPtk 0.0020 GeV/c) on a run by run basis, see section 3.4.

2.4 Baryon Spectrometer

The hyperon will decay while it travels through the apparatus. The charged decay product is the baryon. This section explains how E761 measured the baryon momentum vector and position.

The baryon, p or $\bar{p}$, is stable; therefore, for this case we were not restricted by detector separation. The only requirements were to have high angle and momentum resolutions.

The baryon spectrometer consisted of four proportional wire chamber (PWC) stations with large separations between them, and a dipole magnet. The angle resolution is 10 μm (σ), the position resolution is 250 μm (σ), and the momentum resolution is 0.2 % (σ). The momentum is measured in the x-z plane. The vertical momentum component is negligible compared to its full value and its resolution.

Figure 2.11 shows the baryon spectrometer. The following sections describe each part of the spectrometer.

2.4.1 Proportional Wire Chamber (PWC)

A PWC is a grid made of metallic wires. The wires were immersed in "magic gas" (75 % Argon + 25 % Isobutane + 0.5 % Freon). One single

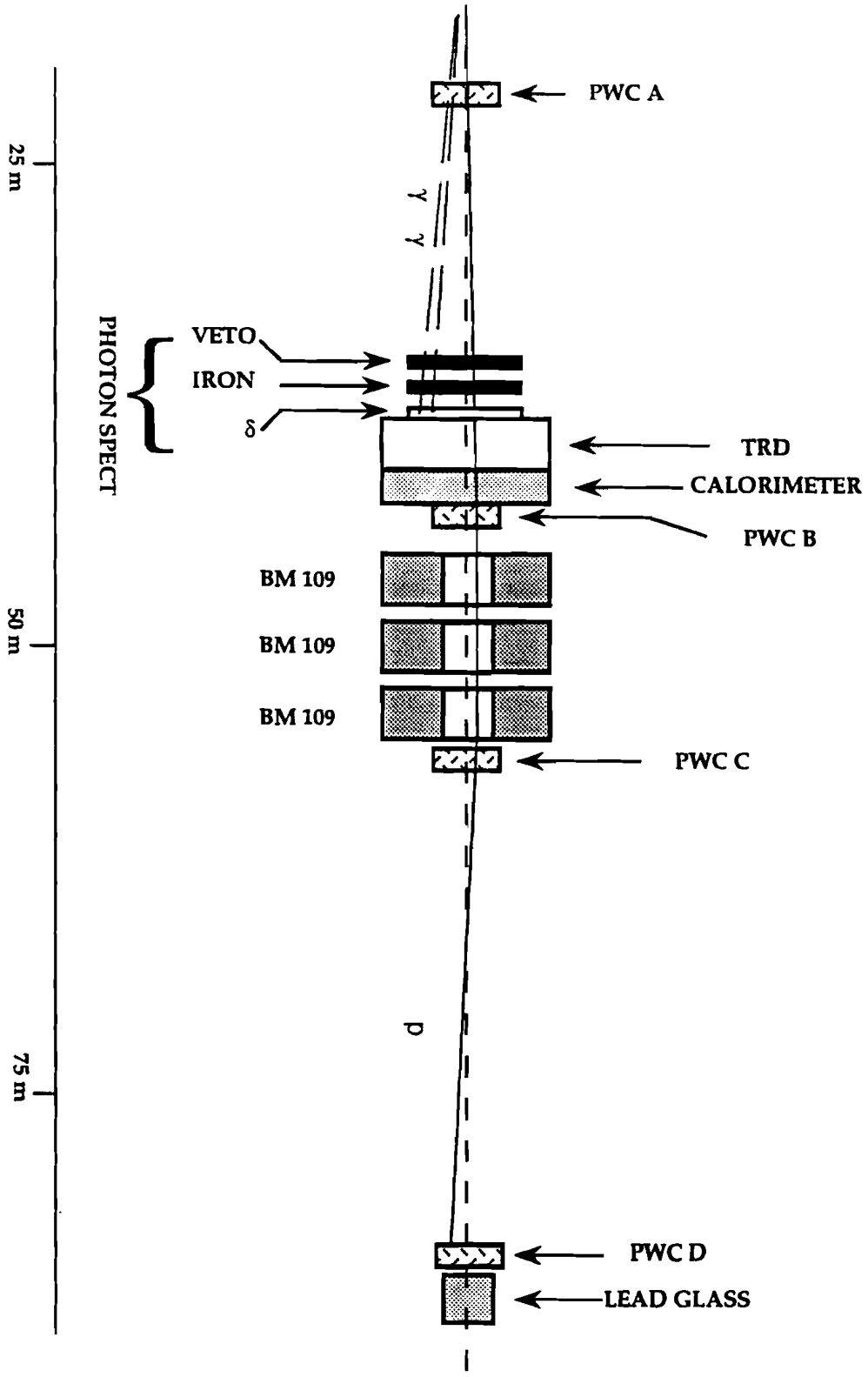

Figure 2.11: Baryon Spectrometer.

chamber unit consisted of a perpendicular pair set of parallel wires. Every wire is an independent position measurement. When a high energy charged particle passes through it ionizes the gas. The wires collect the charge. The collection of the charge was made possible through a high voltage ($\approx$ 2000 V) difference between anode wires and cathode wires (one TRD PWC chamber had a mylar cathode). Electronics attached to the wires converted the signal into a hit position.

There were four PWC stations; WA, WB, WC, and WD. Stations WA, WB, and WC had eight planes each. Each plane was 1 mm pitch. There were two planes in each x, y, u and v view (u and v are perpendicular axis). Station WD had six planes. All planes in station WD were 2 mm pitch. Station WD had two planes in each x, y, and u view.

2.4.2 Baryon Dipole Magnet (MA-MB-MC)

The spectrometer included three dipole magnets, MA, MB and MC, connected in series. Each dipole magnet had a full aperture of 60.96 x 20.32 x 182 cm^3. The magnetic field was parallel to the y axis.

The magnet was operated at 2082 $Amps$ producing a 14.4 kG field. The individual Ptk 's were -0.8205, -0.8125 and -0.8155 giving a -2.4486 GeV/c total Ptk . The effective $\int B\,dl$ from WB to WC was 8.2 $T \cdot m$. The magnet polarity was the same as the hyperon target magnet. The Ptk sign was negative regardless of the hyperon charge since the current polarity was changed. The three magnets were located as near as possible to each other, approximately 50 cm space between magnets. The field was uniform to 0.47 % across a transverse section of Δx 8 cm by Δy 6.5 cm. The total Ptk was uniform to 0.07 % (ΔPtk 0.0018 GeV/c) on a run by run basis, see section 3.4.

2.5 Photon Spectrometer

The photon spectrometer was specialized to measure the photon energy and its position. The transition radiation detector (TRD) measured the position. The electromagnetic calorimeter (EC) measured the energy. Most importantly, the photon spectrometer assured the photon's existence for either $\Sigma^+ \rightarrow p\pi^0$ or $\Sigma^+ \rightarrow p\gamma$ decays.

At this point in the apparatus we are dealing both with a charged baryon and a photon (s). A possible detector for the neutral should be transparent to charged particles and able to identify photons. Three solutions can be proposed for such a detector:

- One solution is to put a hole (7.6 by 7.6 cm^2) in the photon detector to let the charged particles pass.
- Second solution is to change the charged particle direction away from the photon detector.
- Third solution is to use a special detector naturally transparent to high energy charged particles.

All three methods were used in the photon spectrometer, see figures 2.12, 2.13, and 2.14.

The way we assured photon existence was with a scintillator charge veto, an iron sheet (1 *in* thick or 1.44 radiation lengths), a coincidence scintillator and an electromagnetic calorimeter. The charge veto guarantees a neutral particle entering the photon detector (requiring the scintillator not to fire). The iron sheet converts the photon into a charged shower which then is detected by the second scintillator. The EC, far away from the baryon, measures the energy of the photon shower.

The analysis of $\Sigma^+ \rightarrow p\pi^0$ does not use the measured photon position and energy. Only a 5 GeV EC energy requirement and scintillator signals were used in the trigger. The TRD is not used at all for the polarization and magnetic moment measurements. Photon existence is more closely defined in the trigger section.

In the following sections I describe the EC and TRD.

2.5.1 Electromagnetic Calorimeter (EC)

The electromagnetic calorimeter is a detector which will absorb the full energy of an electron or a photon. The calorimeter gives a response proportional to the energy of the incident particle. Through positron-electron pair production and bremsstrahlung the original photon (or electron) is converted into low energy positrons and electrons exciting atoms which will produce light. The light is collected by a phototube which is then amplified and sent to an analog to digital converter (ADC).

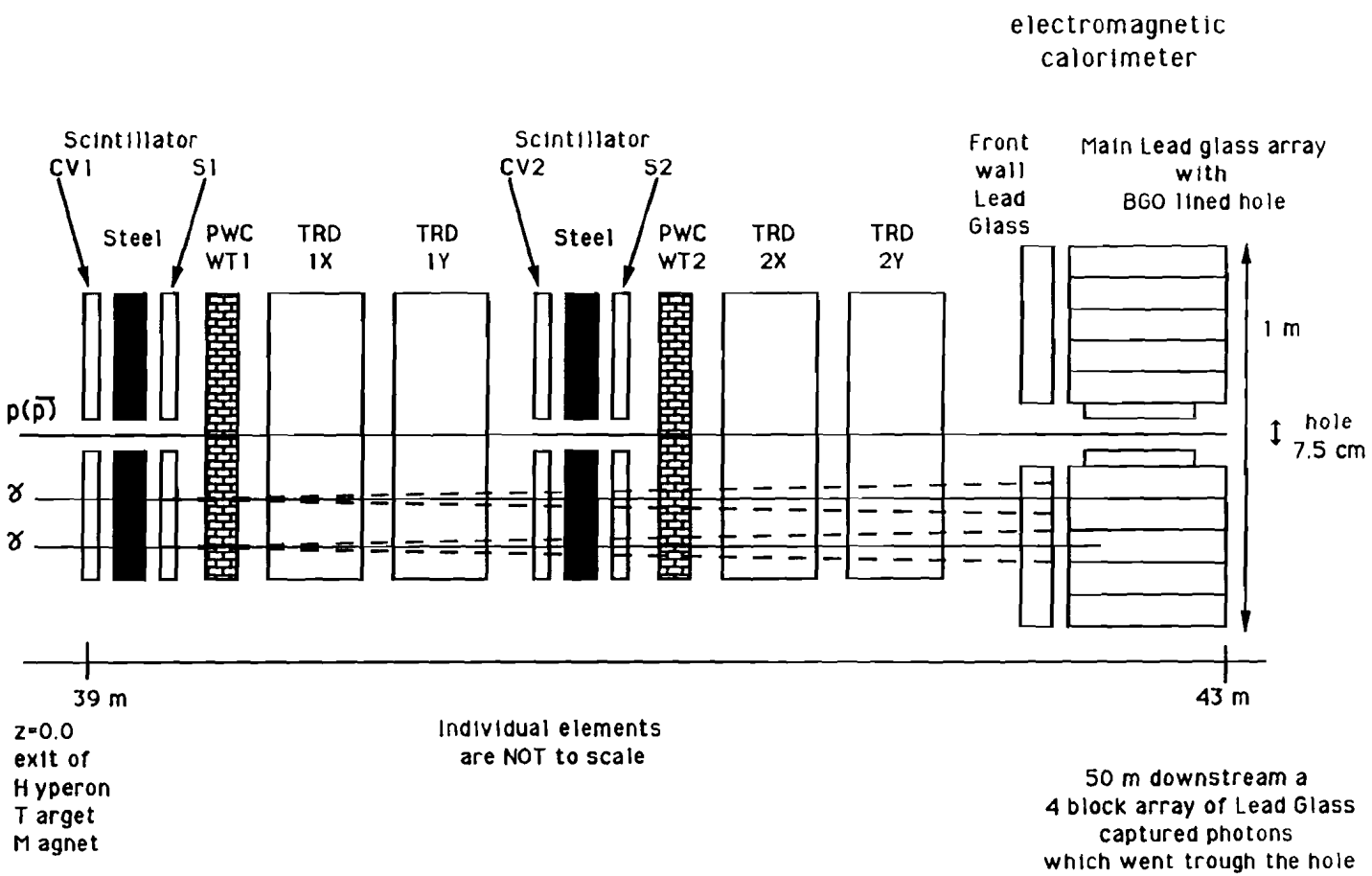

Figure 2.12: Photon Spectrometer.

The electromagnetic calorimeter was built with lead glass blocks (PBG, 3 *cm* radiation length) and Bismuth Germanate (BGO, 1.12 *cm* radiation length). There were three separate arrays; front, main, and rear. Figure 2.13 shows the geometrical block distribution. The array position was optimized to cover the solid angle distribution of the photons from $\Sigma^+ \rightarrow p\gamma$. The photon energy was in the 5 to 150 *GeV* range. The energy resolution was 73 % / $\sqrt{E}$.

2.5.2 Transition Radiation Detector (TRD)

I will only describe the TRD briefly here since it is not used in the production polarization and magnetic moment measurement analysis at all. The analysis and application of the TRD is found in reference [12]. Figure 2.14 shows a TRD sketch.

High energy photon(s) from $\Sigma^+ \rightarrow p\gamma$ or $\Sigma^+ \rightarrow p\pi^0$ ($\pi^0 \rightarrow \gamma\ \gamma$) are converted in a steel plate into positron-electron pairs (electromagnetic shower). The high energy charged component of the shower follows closely the initial photon direction. When this shower crosses a series of 200 polypropylene foils it produces transition radiation x-rays. PWC's with a Xe mixture (30% CH_4) detect these x-rays and give a 2 *mm* position resolution for the high energy photons. For a cross check there were conventional PWC's to measure the position of the charged shower itself.

2.6 Trigger

The trigger was the coincidence of a charged particle crossing the hyperon spectrometer, a charged particle crossing the baryon spectrometer, and a photon conversion signal from the photon spectrometer. The trigger was made with scintillator counters located throughout the spectrometers. Some detector signal information was also used in the trigger.

The charge of the particle crossing the hyperon spectrometer was selected by the HTM field and geometry. Oppositely charged particles would either interact in the HTM channel wall or go out of the hyperon spectrometer's geometrical acceptance.

There were two different triggers used in the selection of baryons:

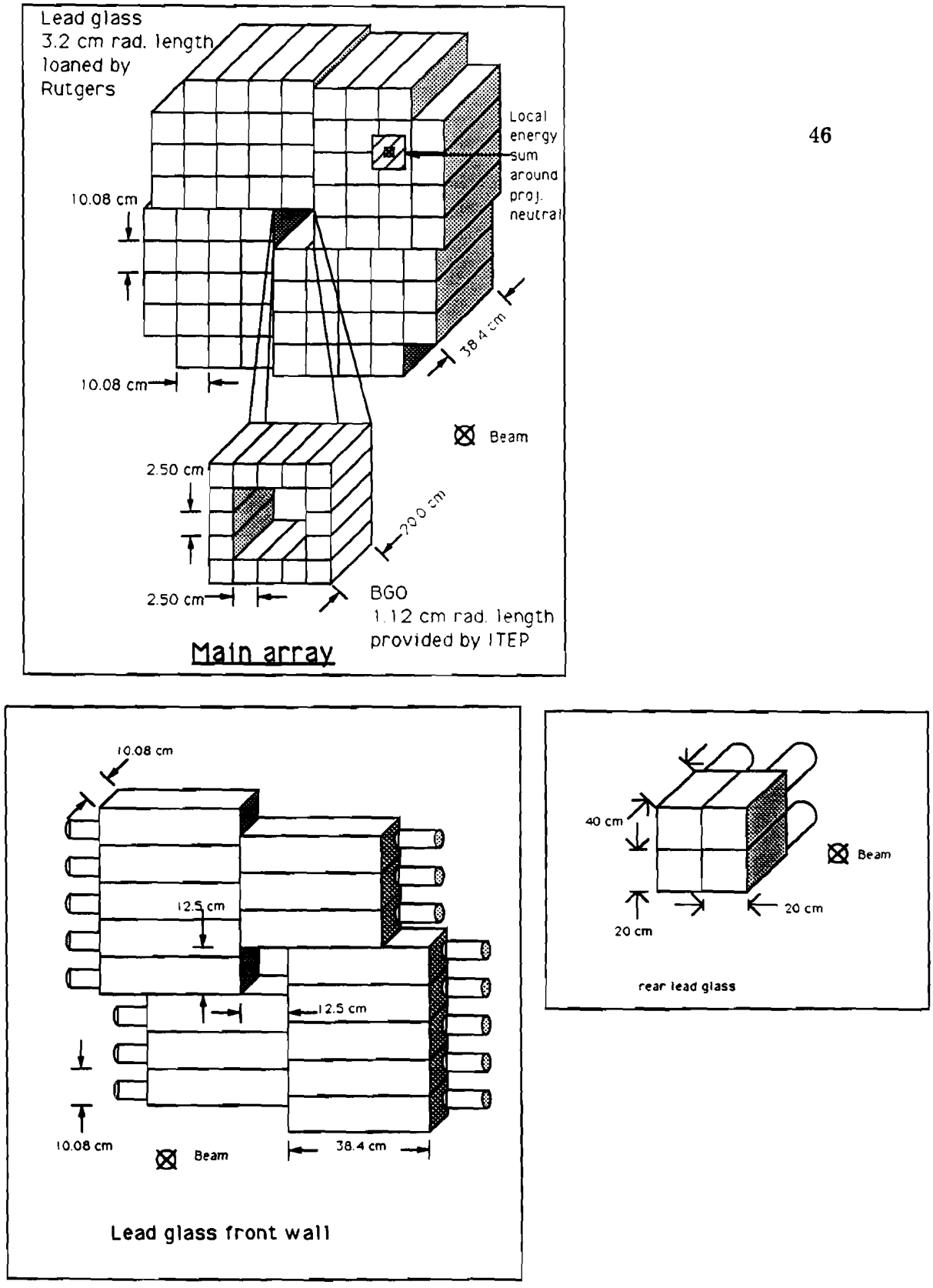

Figure 2.13: Electromagnetic Calorimeter Geometry.

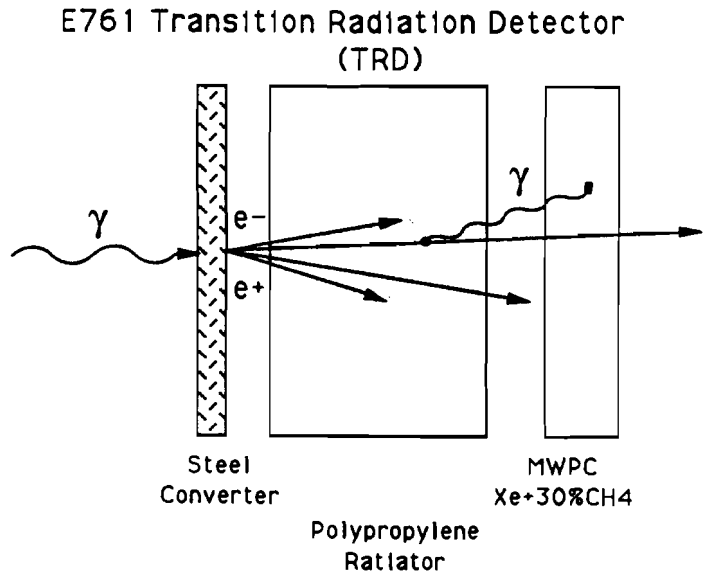

Figure 2.14: Transition Radiation Detector Geometry.

- The *PHOTON* trigger explicitly required a charged particle in the baryon spectrometer. The baryon was flagged by the proton scintillator counter (p) located upstream station WD.

  This trigger was used for $\Sigma^+ \rightarrow p\gamma$ data taking and resulted in 48 million $\Sigma^+ \rightarrow p\pi^0$ events.

- The *NEGPHOTON* trigger did not care about the baryon.

  This trigger was used for Σ^+ and $\bar{\Sigma}^-$ polarization and magnetic moment data. The reason we did not use the proton scintillator counter was due to a parallel production study $\Xi^- \rightarrow \Lambda^0 \pi^-$ ($\Lambda^0 \rightarrow p\pi^0$, $\pi^0 \rightarrow \gamma\ \gamma$). Ξ^- physics is the subject of another thesis.

Comparing the *PHOTON* and *NEGPHOTON* trigger signal fractions respect to the total number of triggers a 37 % background rejection is observed using the proton scintillator counter (p).

Photons were not distinguished between photons coming from decays $\Sigma^+ \rightarrow p\pi^0$ ($\pi^0 \rightarrow \gamma\ \gamma$), $\Sigma^+ \rightarrow p\gamma$, or any beam interaction which possibly could produce photons and trigger the photon detector.

From the above pieces the decay triggers looked more like:

$$photon\ trigger = hyperon \cdot baryon \cdot photon$$

$$negphoton\ trigger\ =\ hyperon \cdot photon$$

These decay triggers were intentionally overridden by a trigger in which only a particle crossing the hyperon spectrometer was required. The trigger overridden was at the rate of one every 100th. The generic name of this trigger mode was $T1PS$. To achieve this approximate rate the hyperon request was prescaled by a factor of 8192. The $T1PS$ data set were used for fine tuning during the data analysis. The data of triggers when only the hyperon spectrometer was requested were almost 100 % undecayed particles.

There was another trigger called $STANDARD$ with the requirement of only a particle crossing the hyperon spectrometer. The $STANDARD$ data was used to align SSD and PWC, and calibrate spectrometer magnets during the data taking (see alignment section). $STANDARD$ data, together with $T1PS$ sample, were useful for studying branching ratios and beam fluxes.

All triggers had a timer called rationer ($RATP$). This part would let only one hyperon be processed in a $\pm$ 200 ns time window. The time range was needed to assure separation of events due to the long drift time in the TRD xenon chambers.

I should state that trigger scintillators and detectors were positioned by a Monte Carlo. Using Monte Carlo simulation we found the efficiency from the geometrical (apparatus) and trigger ($PHOTON$) acceptance to be 64 % for $\Sigma^+ \rightarrow p\gamma$ and 85 % for $\Sigma^+ \rightarrow p\pi^0$. Fine position tuning of scintillators was made during run time. The analysis section describes the offline fine tuning, alignment, and calibration of detectors.

With counter signals and logic electronics we built our trigger. The following sections describe the counters and logic.

2.6.1 Counters and Logic

A particle in the hyperon spectrometer was defined by three scintillators in coincidence; $B1$, $B2$ and $B3$; two veto scintillators to remove beam halo; $VH2$ and $VH3$; together with a beam gate coming from the accelerator system, this trigger part had the generic name as $T1$.

A particle in the baryon spectrometer was defined by a scintillator called p.

The photon conversion, called $T2$, was defined by the *or* of three choices:

- The first had a charge veto $CV1$ in coincidence with a scintillator $S1$ after the iron sheet, together with a $T1$. The generic name was $S1PHOTON$.
- The second similarly used the charge veto $CV1$, another charge veto $V2$, and a coincidence scintillator $S2$ after the second iron sheet, together with a $T1$. All these scintillators and iron sheets had a square hole each in the center to let the baryon or the undecayed beam pass. The generic name was $S2PHOTON$.
- The third choice, $REARPHOTONPS$, dealt with the photons which went through the hole along with the baryon. It used: $\overline{CV1}$, $\overline{V2}$, $\overline{S1}$, $\overline{S2}$, a scintillator veto in front of rear PBG ($RPBGV$), and a 10 GeV rear PBG energy cut, together with a $T1$ and then prescaled by a factor of 4.

From a shower Monte Carlo (EGS) the photon shower conversion efficiency with one 1 *inch* iron sheet was 65 %. The global photon shower conversion using the two 1 *inch* iron sheets was 89 %. From a study using $T1PS$ data it was found that the photon detector was 76 % efficient on $\Sigma^+ \rightarrow p\pi^0$.

The signal which starts the event trigger was called $T3$. This is the one which differentiated between $PHOTON$ and $NEGPHOTON$ trigger. Signal $T3$ is the *or* of two choices:

- The first was different depending the decay trigger being used. For the $NEGPHOTON$ trigger, this choice was a triple coincidence of $T2$, a 5 GeV total EC energy cut, and rationer $RATP$. For the $PHOTON$ trigger, it was a quadruple coincidence of $T2$, a 5 GeV total EC energy cut, rationer $RATP$, and scintillator p.
- The second is $T1PS$.

Comparing the number of events with or without the EC energy cut trigger signal a 60 % background rejection is observed using the 5 GeV total EC energy cut in the trigger. Figures 2.15a-b show in a qualitative way the amount of data which is rejected when an energy cut is applied in the EC. Figure 2.15a shows the particle energy distribution when the energy cut was out of the

trigger. Figure 2.15b shows the same particle distribution sample but with a 5 GeV cut applied via a latch bit [13] ($PBGSUM$).

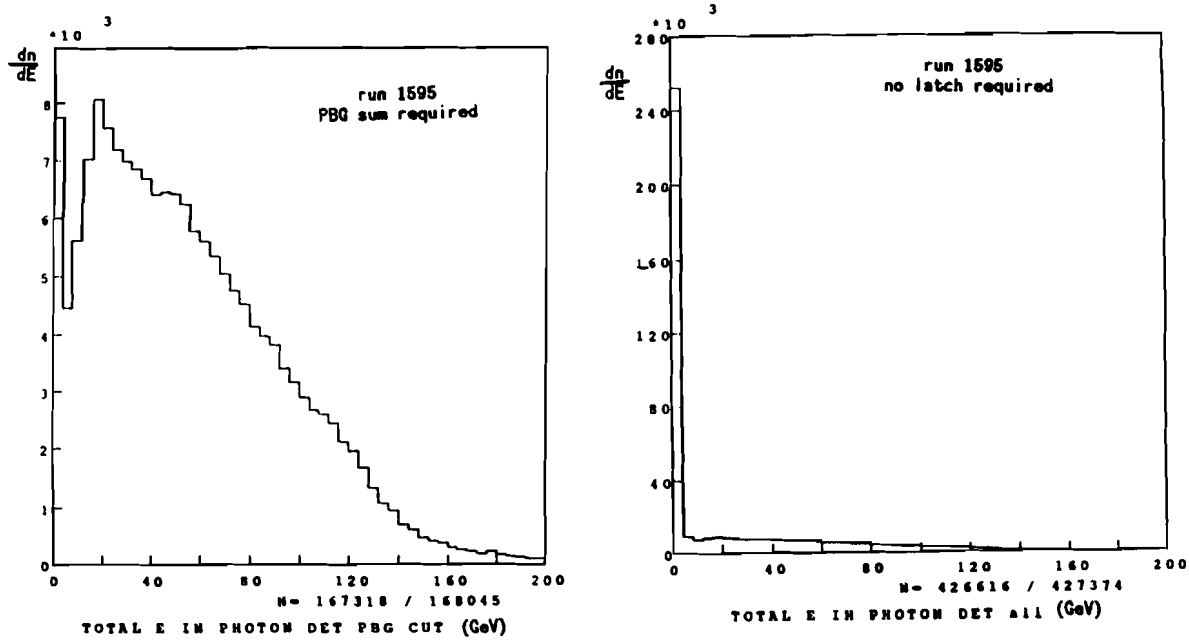

Figure 2.15: Qualitative Enhancement of Trigger with the EC Energy Cut.

With the above explanation the trigger logic construction can be represented symbolically as follows:

$$T1 = B1 \cdot B2 \cdot B3 \cdot \overline{(VH2 + VH3)} \cdot \text{(Beam gate)}$$

$$S1PHOTON = T1 \cdot \overline{CV1} \cdot S1$$

$$S2PHOTON = T1 \cdot \overline{CV1} \cdot \overline{V2} \cdot S2$$

$$REARPHOTONPS = T1 \cdot \overline{CV1} \cdot \overline{S1} \cdot \overline{V2} \cdot \overline{S2} \cdot RPBGV$$

$$\cdot \text{(energy} > 10\,GeV\ ) \cdot \text{(prescaled by a factor of 4)}$$

$$T2 = S1PHOTON + S2PHOTON + REARPHOTONPS$$

$$STANDARD : T3 = T1 \cdot RATP$$

$$PHOTON : T3 = T2 \cdot \text{(energy} > 5GeV) \cdot P \cdot RATP + T1PS$$

[13]Latch is a flag or mark. Generally this flag is a bit in a word. The latch indicates a particular element in a detector was active.

$NEGPHOTON : T3 = T2 \cdot (\text{energy} > 5GeV) \cdot RATP + T1PS$

Figure 2.16 shows details of the different trigger components. For example the $CV1$ scintillator in reality was built from 3 independent scintillator pieces.

The trigger logic was made with CAMAC programmable logic units (PLU). The logic units were programed from our control room with fortran routines.

2.7 Data Acquisition (DAQ)

The data acquisition system (DAQ) gathered signals from the sensitive detectors with CAMAC readout electronics. E761 events were built with 16 bit words. At the same time the event was being built in a Smart Crate Controller [14] (SCC) the event was being buffered into a parallel computer (ACP) for online track reconstruction. From the parallel computer all data was written onto tapes, and part was sent to a VAX 780 memory pool for monitoring and debugging purposes.

Position sensitive detector readout was under a Coordinate Readout System (CROS). The CROS system was used for all SSD strips and PWC wires. This system was designed and assembled at the Leningrad Physics Institute, USSR.

Every SSD strip was connected to an analog MSP1 preamplifier. Every SSD preamplifier and every PWC wire were connected to a N277CD amplifier discriminator. E761 had a total of 10816 instrumented channels (4800 SSD, 2304 TRD, and 3712 PWC). These channels, either on or off, were input to CROS.

CROS is divided into four parts:

- The first is a latch card (RML) which received the discriminated inputs. RML is a 16 step programmable memory. The step time was 56.6 ns, obtained from the accelerator RF divided by three.

[14]The smart crate controller, SCC, is a computer which coordinates the data flow in a CAMAC crate. The SCC is built around M68000 CPU. SCC has an output port, RS-485, suitable to transfer data into ACP.

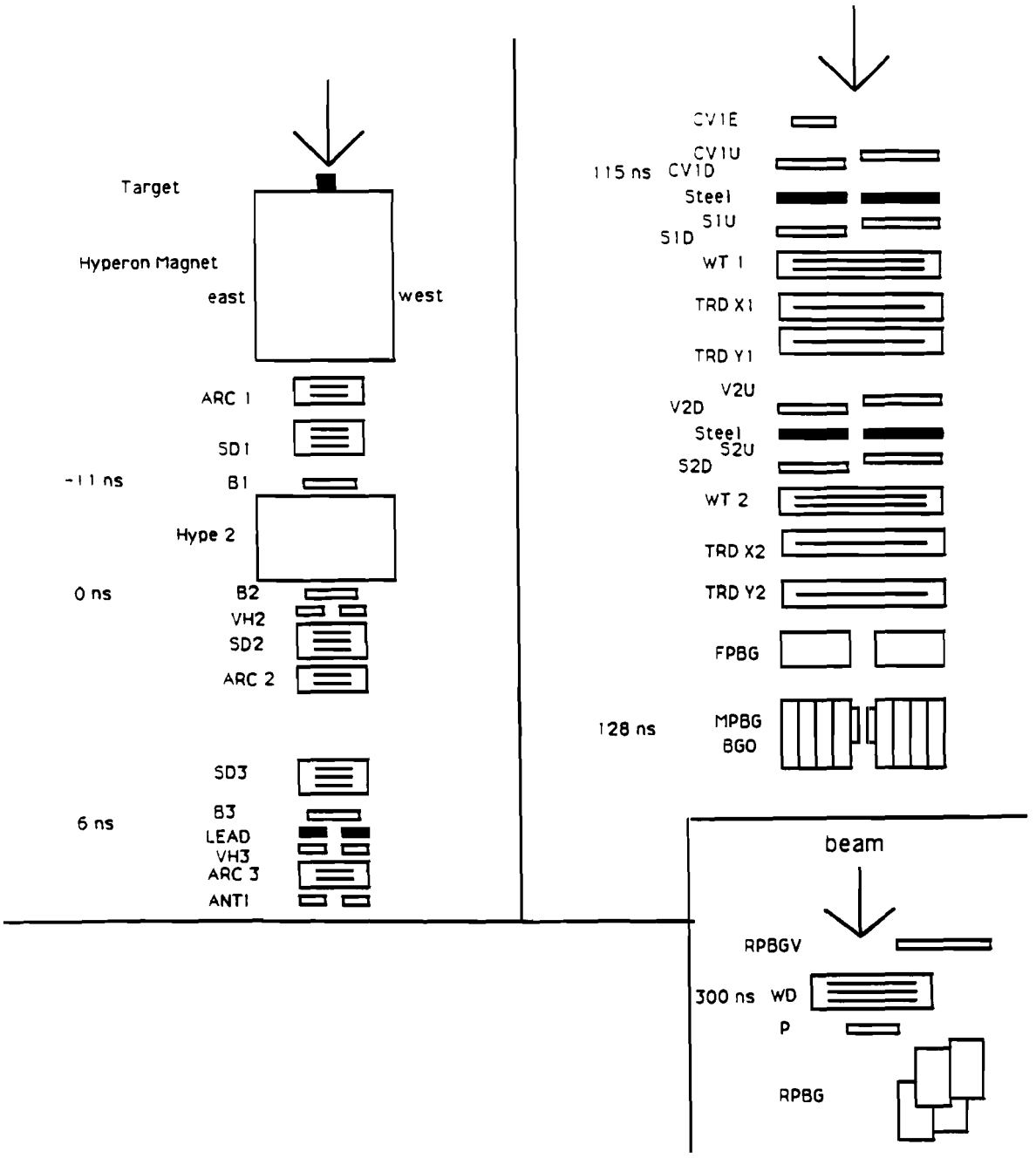

Figure 2.16: E761 Trigger Components.

- The second is a latch control unit per crate (RMLCU). RMLCU received the trigger signals to control the RML's. One of the trigger control signals was the RF/3.
- The third is a local controller per crate (CER). CER also encoded the address of each individual hit (a hit is an "on" wire).
- The fourth is a CAMAC interface and data buffer (BIS) holding up to 64 crates. In E761 there were two BIS's: one buffered the SSD and photon detector PWC's, the other buffered the baryon PWC's.

The BIS's were located in the same crate as the SCC. From there the SCC took the place as the event builder.

The electromagnetic calorimeter had 96 PBG and 16 BGO blocks. Each block was connected to an 11 bit analog to digital converter (ADC). These 11 bits let us resolve one part in 4095. Photon energy ranged between 0 and 150 GeV. The ADC gave us a resolution on the order of a few 10's of MeV. Before run time each block was calibrated with cosmic ray muons. The ADC's were located in the same crate as the SCC.

The BIS's, energy ADC's, miscellaneous scalers, ADC's and TDC's (time to digital converters) were installed in three CAMAC crates. Each of these crates had a SCC. The SCC grouped data into separate blocks depending on the detector type, and buffered the event to a parallel computer (ACP) for online analysis.

The ACP (14 nodes) was directing all events into tape and an event subsample into a VAX 780 memory pool for monitoring purposes.

Figure 2.17 sketches E761 data acquisition.

2.7.1 Rates

E761 was built to handle a hyperon beam of 100 kHz. To match this rate, depending on the targeting angle, we requested from 1 to 100 $10^{10} protons/pulse$ be transported into the proton center beam line (See table 2.1).

The $PHOTON$ trigger rate, also event rate to tape, was 0.7 kHz. This rate was equivalent to write 15000 events/spill. The $PHOTON$ rate

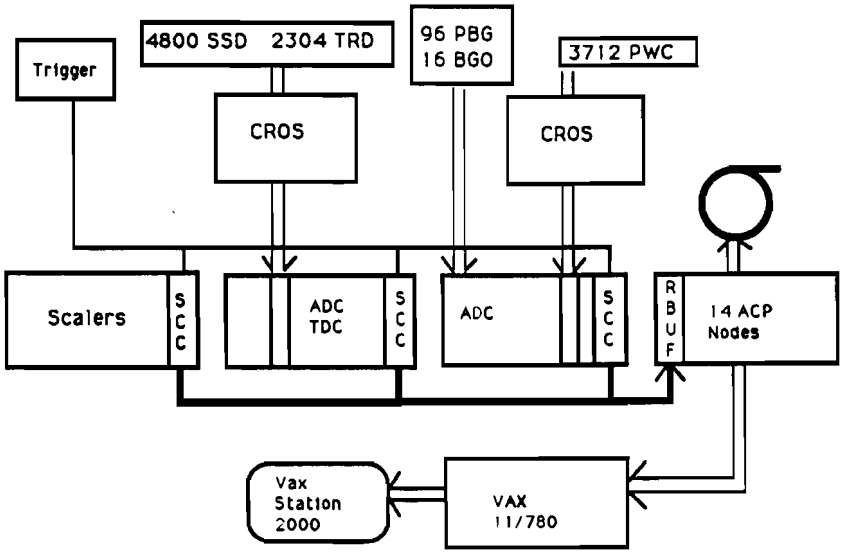

Figure 2.17: E761 Data Acquisition.

matches closely the fact that 1.5 % of the hyperon beam is made of Σ^+ , and the branching ratio of $\Sigma^+ \rightarrow p\pi^0$ is 51.6 % [1]. The DAQ was able to process an event rate little over twice the *PHOTON* rate.

In average a full event took 800 μsec for DAQ processing. In average an E761 event size is 600 bytes.

E761 had beam for 6 months during the February-August Fermilab 1990 fixed target run. The total number of 9-track 6250 BPI tapes written was 3577, storing nearly 1000 million events.

During data collection we were switching from negative targeting angle to positive targeting angle every 3 tapes. In real time this was equivalent to every hour.

Final *PHOTON* trigger physics accounts for $\approx$ 900 tapes gathering $\approx$ 200 million raw events. *NEGPHOTON* trigger accounts for $\approx$ 200 tapes gathering $\approx$ 59 million raw events. Table 2.2 shows the number of triggers or events written to tape. The other major part of data was dedicated to Ξ^- physics.

Table 2.2: Number of Triggers or Events to Tape.

Positive Hyperon Beam		
Horizontal Targeting Mode		
nominal targeting angle	number of triggers	run number (s)
HPB -6.0	250057	2429
HPB -5.5	252858	2425
HPB -5.0	860566	2165 2167 2421
	101859343	start at 1653 total runs 153
HPB -4.5	256587	2417
HPB -2.0	280677	2409
HPB -1.0	286363	2334
HPB 0.0	241468	2407
HPB +1.0	236831	2411
HPB +2.0	263822	2413
HPB +2.5	231663	2415
HPB +3.0	236542	2419
	101802430	start at 1655 total runs 146
HPB +3.5	235425	2423
HPB +4.0	226747	2427
Vertical Targeting Mode		
VPB +3.0	3166227	2477 2478 2479 2491
VPB 0.0	196018	2496
VPB -3.0	3371697	2486 2487 2488 2490 2492

Negative Hyperon Beam		
Horizontal Targeting Mode		
HNB -4.0	9272761	2030 2145 2179 2183 2195 2199 2211 2217 2221 2233
HNB -3.0	8928090	2031 2140 2181 2193 2197 2209 2215 2219 2230 2236
HNB -2.0	607680	2032 2134
HNB -1.0	1277944	2136 2192 2214 2240
HNB 0.0	669860	2036 2132
HNB +1.0	8756504	2143 2182 2194 2198 2210 2216 2220 2231 2232 2237
HNB +2.0	9566303	2033 2147 2180 2184 2196 2200 2213 2218 2222 2235
HNB +3.0	627251	2034 2149
HNB +4.0	353476	2035 2152
Vertical Targeting Mode		
VNB -3.0	4039203	2497 2499 2501 2511
VNB 0.0	282853	2515
VNB +3.0	3854398	2498 2500 2502 2512

Chapter 3

Data Analysis

3.1 Track Reconstruction

The generic decay we are looking for is $Y \rightarrow B + X$. The hyperon (Y) and baryon (B) are reconstructed with their respective spectrometers. The neutral (X) is not reconstructed, but its energy and position is measured. Another class of event, an undecayed particle, is reconstructed with the hyperon and baryon spectrometers.

E761 required a fast pattern recognition algorithm to select a set of hits in the planes, which could most likely make a track. Even though today's computers are "fast", it took 1.5 months of real time to reconstruct around 600 million events. We used an Amdahl 5890 computer which is approximately equivalent to fifty 780 VAX's. The average CPU time per event was 4 *msec*.

The reconstruction program deals with the recorded information in a series of steps until a track is reconstructed:

- Since data was packed and coded in words by the readout electronics (see section 2.7) the reconstruction starts by unpacking the event. That means reading a record from the storage media (magnetic tape) and allocating a program variable for the hits. At the same time it clusters wires (or strips) that belong to the same plane and same physical track. Since a hit is a cluster with width one in the next lines I use "hit" as a generic name for a hit itself or a cluster.

- A pattern recognition algorithm groups hits in the same SSD or PWC station which together define a space point. A space point is a full three

dimensional cartesian coordinate, not just a hit. This algorithm takes at least two non-parallel hits and a third one is grouped if it is close within 3.5 wire or strip spacings. In SSD stations a minimum of two hits made an space point, the baryon case was three. More than one space point may exist per station.

- Another pattern recognition algorithm will then group the space points per station into a track candidate. The algorithm looks for hits which will make a y vs z straight line in the hyperon spectrometer case. The baryon spectrometer looks for two straight lines which make a kink in the middle of the magnet. Since $\Sigma^+ \rightarrow p\gamma$ and $\Sigma^+ \rightarrow p\pi^0$ are one track per spectrometer multiple track candidates, with totally independent space points, cause the event to abort. When more than one space point were inside a window of 0.03 *cm* in SSD or 0.6 *cm* in PWC then non-independent track candidates may exist per event.

- Having the track candidate (collection of hits) the last step is to obtain the physical quantities which define the track:

x_0	track intercept in x at SSD3,
θ_{x0}	track angle in $x - z$ plane at SSD3,
y_0	track intercept in y at SSD3,
θ_{y0}	track angle in $y - z$ at SSD3,
$\frac{1}{p}$	inverse of the particle momentum, and
χ^2_ν	reduced χ^2, a measure of the fit quality.

  In appendix B there is more explanation on how to obtain the above quantities from the hit information.

- To improve the track quality the fitting routine was used as follows to test a few other hypothesis:

  - Select the minimum χ^2_ν for multiple non-independent track candidates.
  - Drop the hit farthest from the fitted track.
  - Recover hits which are within one wire spacing from the track.

Figure 3.1 shows the reduced χ^2 for hyperon and baryon tracks for a single run. The broader hyperon χ^2_ν distribution versus the narrower baryon χ^2_ν is explained by the different plane numbers, 9 and 30 respectively.

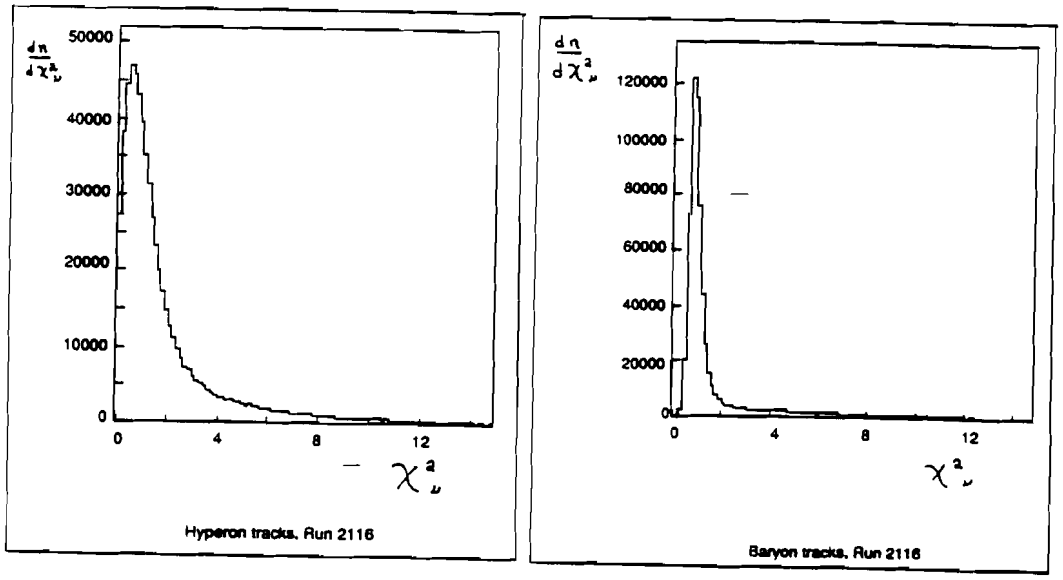

Figure 3.1: χ^2_ν for Hyperon and Baryon Tracks Run 2116.

3.2 Alignment of Chambers (SSD and PWC)

All SSD's and PWC's were originally surveyed by the E761 experimenters to a precision of $\sim 1\ mm$. Since we had detectors with resolutions of 10's of *microns* a technique relying on the track reconstruction itself was used for precision alignment. This alignment used undecayed particle tracks. Since we had two independent spectrometers the relative magnetic field calibration between HYPE2 and MA-MB-MC magnets was checked.

The alignment started by fixing the center of planes SD2X, SD2Y, WB2X and WB2Y. From there a fit through all SD2, SD3, WA and WB planes was made. Residuals (fit prediction - hit) were iterated until the residual distribution peaked at zero. An extra feed back residual correction was made by removing explicitly the plane in study from the fit. Alignment for WC and WD was made with runs having MA=MB=MC at zero field. Alignment for SD1 was made with runs having HYPE2 at zero field. Two alignment studies cover the data for this thesis. The biggest correction for the same data is 0.36 mm.

A check on each plane's angle orientation was made by comparing the actual u hit to the predicted u view, obtained from the $x\ and\ y$ views. Plane

WB-V4 (nominal 45°) has the biggest correction at 0.9°.

A relative magnet calibration was needed to fit undecayed particle tracks through all SSD and PWC planes at once. Magnets HYPE2 and MA-MB-MC were known to 0.1 % and 0.47 % magnetic field precision respectively, they were operated in a linear region. Since the magnets were mapped prior to run time we knew the momentum deflection (Ptk , see section 2.2.3) of each magnet. Field measurements were recorded for each magnet per run (actually, per spill) which used to scale the Ptk for each run. The undecayed particle track was fitted with SD1,SD2,SD3,WA and WB planes and was independently fitted with SD2,SD3,WA,WB,WC and WD. The ratio of the momentum of both fits was found to be 1 ± 0.001. In conclusion HYPE2 and MA-MB-MC were relatively calibrated from the original field measurements.

This alignment and magnetic calibration represent the standard E761 reconstruction analysis. An absolute momentum calibration is explained in another section. The absolute momentum calibration was needed to check the HTM Ptk .

3.3 Signal Σ^+ and $\bar{\Sigma}^-$

After the charged track parameters were defined the following variables are constructed:

$$
\begin{aligned}
r &= \frac{p_B}{p_Y} \\
\theta_{YB} &= \sqrt{(\theta_{x0B} - \theta_{x0Y})^2 + (\theta_{y0B} - \theta_{y0Y})^2} \\
z_v &= \frac{(X_{0B} - x_{0Y})(\theta_{x0B} - \theta_{x0Y}) + (y_{0B} - y_{0Y})(\theta_{y0B} - \theta_{y0Y})}{\theta_{YB}^2} \\
\cos\theta_x &= \frac{p_B(\theta_{x0B} - \theta_{x0Y})}{p_{CM}} \\
\cos\theta_y &= \frac{p_B(\theta_{y0B} - \theta_{y0Y})}{p_{CM}} \\
\cos\theta_z &= -\frac{E_{CMB}}{p_{CM}} + \frac{m_Y}{p_{CM}} r
\end{aligned}
$$

where:

r is the ratio of baryon momentum to hyperon momentum.

θ_{YB} is the opening angle between the hyperon and baryon tracks at the decay point. An approximation for small angles has been applied.

z_v is the vertex z position of the decay point. It is obtained by minimizing the distance between the hyperon and baryon tracks.

$\cos\theta_x$, $\cos\theta_y$, $\cos\theta_z$ are the baryon directional cosines in the hyperon center of mass (CM) system. Approximations $\beta = 1$ and $P_{lab} = E_{lab}$ have been applied. E_{CMB} is the CM baryon energy. The CM baryon (or neutral) momentum is unique and given by:

$$p_{CM} = \frac{1}{2}\frac{\sqrt{(m_Y^2 - (m_B - m_X)^2)\,(m_Y^2 - (m_B + m_X)^2)}}{m_Y}$$

For two body decays the scatter plot θ_{YB} versus r gives an elegant representation of the decays. Figure 3.2-a shows the data for the positive hyperon beam while Figure 3.2-b shows the negative hyperon beam. Figure 3.2-c shows the predicted θ_{YB} versus r plots.

To select the decay $\Sigma^+ \rightarrow p\pi^0$ ($\bar{\Sigma}^- \rightarrow \bar{p}\pi^0$) I use a cut in the neutral mass reconstructed from the hyperon Σ^+ ($\bar{\Sigma}^-$) and the baryon p ($\bar{p}$) tracks, see table 3.1. Figure 3.3 shows two plots, one of them is the reconstructed neutral mass squared distribution for the *PHOTON* megasample (48 million $\Sigma^+ \rightarrow p\pi^0$ events). The second figure shows the neutral mass for the negative hyperon from the full *NEGPHOTON* sample. The π^0 peak from $\Sigma^+ \rightarrow p\pi^0$ ($\bar{\Sigma}^- \rightarrow \bar{p}\pi^0$) and γ peak from $\Sigma^+ \rightarrow p\gamma$ ($\bar{\Sigma}^- \rightarrow \bar{p}\gamma$) can be seen. The neutral mass squared peak from $K^+ \rightarrow \pi^+\pi^0$ ($K^- \rightarrow \pi^-\pi^0$) is in the wrong place due to the fact that a Σ^+ and p ($\bar{\Sigma}^-$ and $\bar{p}$) hypothesis was used. Only the general quality data cuts were applied on these plots.

Table 3.1 shows the quality cuts applied to the neutral mass plots. In the same table are shown the cuts to select the signal for the final analysis.

After the selection cuts the background under the $\Sigma^+ \rightarrow p\pi^0$ peak is less than 0.2 % in *PHOTON*. Background under $\Sigma^+ \rightarrow p\pi^0$ peak is less than 0.3 % in *NEGPHOTON*. Background under $\bar{\Sigma}^- \rightarrow \bar{p}\pi^0$ peak is less than 2.1 %. The background estimation is an upper limit assuming a uniform flat background distribution under the peak signal in the neutral mass square distribution.

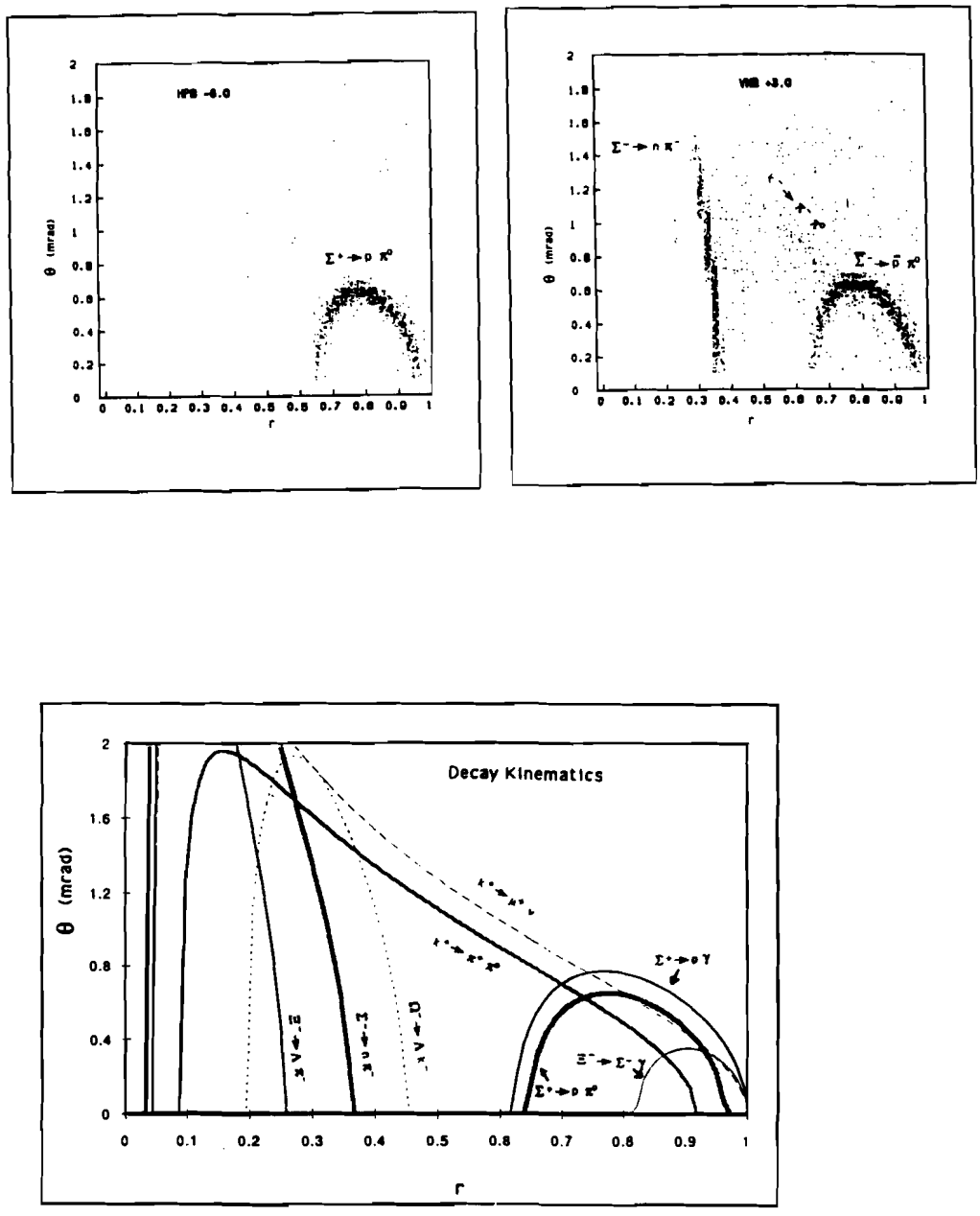

Figure 3.2: θ_{YB} Versus r Scatter Plot.

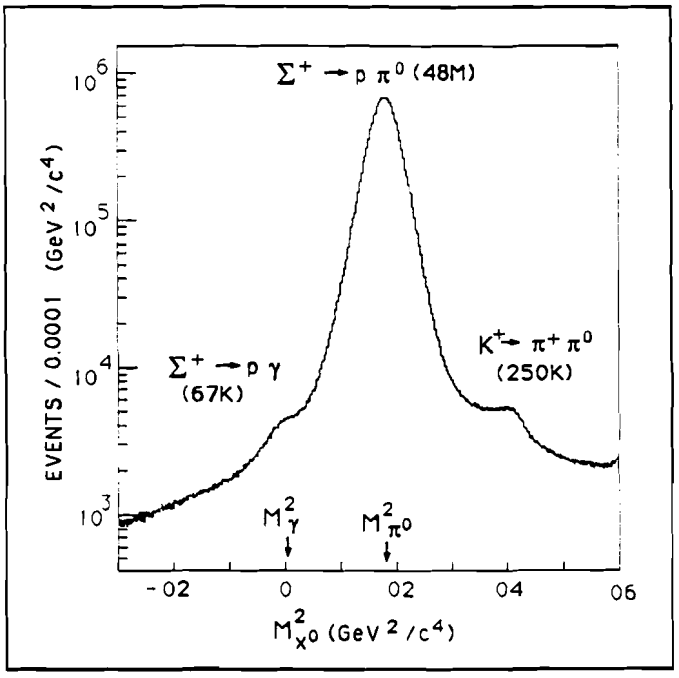

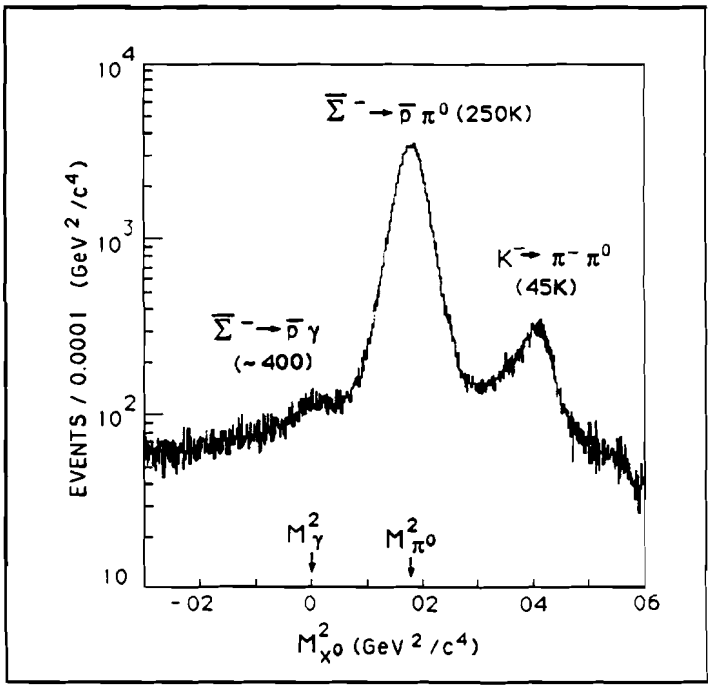

Figure 3.3: Neutral Mass Square for Positive and Negative Hyperon Beam.

Table 3.1: Analysis Cuts.

General Quality Data Cuts				
		$\chi^2_{\nu B}$	$<$	2
		$\chi^2_{\nu Y}$	$<$	4
		r	$<$	1
$325\,GeV/c$	$<$	p_Y	$<$	$425\,GeV/c$
$0.0001\,rad$	$<$	θ_{YB}		
$0\,cm$	$<$	z_v	$<$	$1200\,cm$
Selection Cuts				
$0.002\,rad$	$<$	θ_{x0Y}	$<$	$0.004\,rad$
$-0.001\,rad$	$<$	θ_{y0Y}	$<$	$0.001\,rad$
$3\,\sigma\,x$		target cut		see target section
$3\,\sigma\,y$		target cut		see target section
$1.8\,cm$	$<$	x_{0Y}	$<$	$2.5\,cm$
$-0.45\,cm$	$<$	y_{0Y}	$<$	$0.35\,cm$
-1.0	$<$	$\cos\theta_x$	$<$	1.0
-1.0	$<$	$\cos\theta_y$	$<$	1.0
-1.0	$<$	$\cos\theta_z$	$<$	1.0
exclude		$K^+ \rightarrow \pi^+\pi^0$		$(K^- \rightarrow \pi^-\pi^0)$
calculate $m^2_{\pi^0}$ from K^+ and π^+ (K^-, π^-)				
$0.024\,(GeV/c^2)^2$	$<$	$m^2_{\pi^0}$ or $m^2_{\pi^0}$	$<$	$0.012\,(GeV/c^2)^2$
select		$\Sigma^+ \rightarrow p\,\pi^0$		$(\bar{\Sigma}^- \rightarrow \bar{p}\,\pi^0)$
calculate $m^2_{\pi^0}$ from Σ^+ and p $(\bar{\Sigma}^-, \bar{p})$				
$0.010\,(GeV/c^2)^2$	$<$	$m^2_{\pi^0}$	$<$	$0.026\,(GeV/c^2)^2$

3.4 Absolute Momentum Calibration

The absolute momentum calibration is needed to know the HYPE2 Ptk and HTM Ptk to 0.1 % precision. This calibration has been extensively used to test the HTM Ptk and the effective z target center position.

From the standard analysis described above the π^0 mass square is 0.017982(3) $(GeV/c^2)^2$ while the accepted value is 0.018218(0) [1]. This discrepancy is due to the calibration of HYPE2 and MA-MB-MC.

The calibration technique uses the true [1] particle masses (M_X^{2t}, M_Y^2, M_B^2) from the decay $\Sigma^+ \rightarrow p\pi^0$ ($\bar{\Sigma}^- \rightarrow \bar{p}\pi^0$). The momentum calibration is related to a neutral mass (M_X^2) dependence on the parameter r (p_B/p_Y) caused by the calibration parameters (α, β) as will be shown in the following lines.

The relation between the true momentum (p_Y^t , p_B^t) and the measured one (p_Y , p_B) can be written as:

$$p_Y^t = p_Y(1+\alpha)$$

$$p_B^t = p_B(1+\beta)$$

For a two body decay M_X^2 is only function of the hyperon and baryon momentum. Based on this we can expand M_X^2 on α and β to first order around zero:

$$M_X^2(p_Y,p_B) = M_X^2(p_Y^t,p_B^t) + \left.\frac{\partial M_X^2}{\partial\alpha}\right|_{\alpha,\beta=0}\alpha + \left.\frac{\partial M_X^2}{\partial\beta}\right|_{\alpha,\beta=0}\beta$$

The partial derivatives are obtained from $M_{X(\alpha,\beta)}^2$. Using the quadrimomentum conservation M_X^2 can be written as:

$$M_X^2 = M_Y^2 + M_B^2 - 2E_Y E_B + 2p_Y p_B \cos\theta_{YB}$$

Substituting the $\cos\theta_{YB}(\alpha,\beta=0)$ term from the above M_X^2 expression into the expansion and keeping only terms to second order in (M/p), for hyperon and baryon, we obtain:

$$M_X^2 = M_X^{2t} + (m^2 - 2\,r\,M_Y^2)\,\alpha + (m^2 - 2\,\frac{1}{r}\,M_B^2)\,\beta$$

[1]The term "true" refers to the accepted masses from the particle data book [1]

where: $$m^2 = M_Y^2 + M_B^2 - M_X^{2t}$$

Figures 3.4 a and b show the M_X^2 dependence on r before and after the calibration is applied. The correction is on the order of 0.2 % in r for undecayed particles.

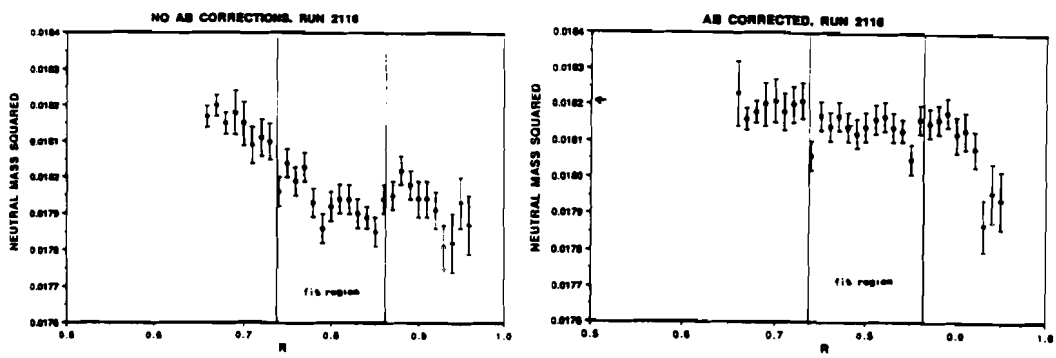

Figure 3.4: Neutral Mass Square Versus r.

3.5 Target: Angles, Position and HTM Ptk

At this point the HTM Ptk is known to $\approx$ 0.78 %. The uncertainty came from a detailed comparison between a magnetic field map made in the year 1979 versus a fringe field map made for E761 in 1989. Just 0.70 % of the uncertainty came from the difference between the predicted field at E761 current from the 1979 excitation curve against the actual field recorded by E761. The different contributions to the uncertainty are listed below. As I am writing there is a working plan to fully map the HTM field to 0.1 % accuracy.

The magnetic moment measurement (or precession angle) depends directly on $\int B\,dl$, or equivalently the Ptk , which deflects the hyperon track. The knowledge of the HTM field map and the effective z position of the hyperon production at the target are important to obtain this integral. Figure 2.8

shows the HTM field map. The HYPE2 Ptk is obtained from the absolute momentum calibration explained above.

HYPE2 Ptk is $+1.4243 \pm 0.0020$ GeV/c, see section 2.3.2.

To obtain the effective z position of the interaction point at the target I used a Monte Carlo simulation. The Monte Carlo generates a gaussian distributed beam in x direction with the same spread as in the experiment see section 2.2.1. The target is made with the same dimensions as in the experiment, see section 2.2.2 and it is tilted by 0.003 *radian*. The Monte Carlo emulates the incident proton beam impinging on the target and records the coordinates of the interaction point. The Monte Carlo also scans the beam through the target face to find the maximum interaction rate. The incident proton scan was made during the run to locate the beam onto the target [2] . Due to this scanning and the small size of the target in the x dimension (0.58 mm), the z and x effective interaction point at the target were different for each of the incident proton horizontal angles we used. For vertical targeting angle the effective interaction point remained fixed regardless of the magnitude of the angle. The y target dimension is nine times bigger than the y beam size (σ) while the x target dimension is only four times bigger than the x beam size (σ), see section 2.2.1.

With the effective z interaction position and the HTM field map I am able to compute the Ptk ($\int B\, dl$) for each of the incident proton angles. Tables 3.2 have a column with the effective HTM Ptk for each incident proton angle. The major contribution on the HTM Ptk uncertainty comes from the field measurement stated above. For vertical targeting angle (magnetic moment measurement) there is a zero Ptk uncertainty on a run by run basis.

The HTM Ptk uncertainty is $\pm$ 0.0587 GeV/c (0.78 %). The following lines list the individual contributions to the Ptk uncertainty:

[2]The data collected during these beam scans were used to determine the target tilt. The spread of the distribution from the normalized hyperon beam against the scanning variable is a measure of the target tilt. The targeting angle parallel to the target produces the minimum spread.

0.0000 GeV/c	run by run spread
0.10 %	local consistency of magnetic field map E497 (1979) (the absolute calibration is unknown)
0.70 %	magnetic field E761 versus predicted by E497
0.12 %	magnetic field merge from fringe E761 and map E497
0.30 %	shift E497 map by 3.02 cm
0.02 %	fringe tail at SSD3
0.05 %	magnet edge and target center known to 0.5 cm

The measurement of production polarization is studied as a function of the production $p_\perp$ in the following sections. The knowledge of the incident proton angle and the hyperon angle at the target are relevant for the $p_\perp$.

To determine the incident proton angle at the center of the target I used an incident proton beam transport program with the actual readings from the beam dipole magnets. Tables 3.2 have a column with the incident proton angle at the center of the target for each of the 28 different cases we had. The coordinate system is the same as in the offline reconstruction program. The error or uncertainty came from the incident proton angle spread, which is (σ) 0.34 $mrad$, see section 2.2.1. Other contributions are negligible.

To find the production targeting angle, the angle between the average hyperon trajectory and the incident proton, I used undecayed tracks fitted through all SSD's and PWC's applying the absolute calibration on HYPE2 and MA-MB-MC magnetic fields together with the HTM Ptk . Tables 3.2 have a column with the average targeting angle and the average production $p_\perp$ for each incident proton case. The major contribution to the uncertainties is the incident proton angle spread.

The uncertainty in targeting angle is $\pm$ 0.34 $mrad$.

The uncertainty in production $p_\perp$ is $\pm$ 0.13 GeV/c.

With the HTM Ptk values, I projected the hyperon from SD3 into the target to obtain the x and y target hyperon distributions [3] . From these

[3]It is important for the E761 readers to notice the difference between using the target as a cut versus using the target in the fit.

The center of the target for cutting use, it is obtained projecting the hyperon track into the z target position, the ones shown in table 3.3. We are cutting three σ on the shape of the hyperon distribution at the target.

The center of the target for fitting use, it is obtained projecting the alignment track using $T1PS$ events with the α and $beta$ calibration momentum corrections. This procedure

Table 3.2: Targeting Angle, $p_\perp$, HTM Ptk , and Number of $\Sigma^+ \rightarrow p\pi^0$.

Positive Hyperon Beam						
Horizontal Targeting Mode						
nominal targeting angle		incident proton angle *mrad*	average targeting angle *mrad*	average $p_\perp$ *GeV/c*	HTM Ptk *GeV/c*	events $\Sigma^+ \rightarrow p\pi^0$ ($\bar{\Sigma}^- \rightarrow \bar{p}\pi^0$)
HPB	-6.0	14.431	-4.719	1.803	-7.5204	11784
HPB	-5.5	14.881	-4.242	1.626	-7.5209	11074
HPB	-5.0	15.423	-3.604	1.391	-7.5214	32111
						5741863
HPB	-4.5	15.900	-3.153	1.215	-7.5219	9635
HPB	-2.0	18.408	-0.682	0.258	-7.5248	6440
HPB	-1.0	19.388	0.048	0.038	-7.5258	7778
HPB	0.0	20.388	1.086	0.416	-7.5267	7694
HPB	+1.0	21.347	1.862	0.695	-7.5275	9150
HPB	+2.0	22.324	2.831	1.054	-7.5286	11800
HPB	+2.5	22.838	3.308	1.223	-7.5302	10716
HPB	+3.0	23.275	3.711	1.370	-7.5283	11114
						6831355
HPB	+3.5	23.869	4.382	1.629	-7.5280	12099
HPB	+4.0	24.341	4.731	1.739	-7.5272	11960
Vertical Targeting Mode						
VPB	+3.0	-2.832	-2.563	0.992	-7.5258	123195
VPB	0.0	0.046	-0.007	0.086	-7.5258	5340
VPB	-3.0	3.014	2.597	1.010	-7.5258	126668
Negative Hyperon Beam						
Horizontal Targeting Mode						
HNB	-4.0	16.403	-2.659	1.018	-7.5227	11918
HNB	-3.0	17.490	-1.577	0.601	-7.5237	10505
HNB	-2.0	18.397	-0.609	0.227	-7.5248	654
HNB	-1.0	19.391	0.226	0.035	-7.5258	1433
HNB	0.0	20.347	1.026	0.388	-7.5267	900
HNB	+1.0	21.362	1.940	0.725	-7.5275	13125
HNB	+2.0	22.378	2.885	1.068	-7.5286	17039
HNB	+3.0	23.254	3.672	1.347	-7.5283	1511
HNB	+4.0	24.327	4.852	1.793	-7.5272	1178
Vertical Targeting Mode						
VNB	-3.0	-2.827	-2.686	1.006	-7.5258	6559
VNB	0.0	0.069	0.009	0.088	-7.5258	327
VNB	+3.0	3.031	2.600	1.016	-7.5258	5247

distributions I got the x and y center and σ (gaussian fit). The values are used to apply a 3 σ target cut to remove events which were not produced at the target. Table 3.3 shows the target x and y center and σ.

Before leaving this section I describe an alternate way to test the precision of the HTM Ptk. The test requires to project undecayed tracks from the $T1PS$ data set into the target z position. These tracks were reconstructed using all SSD and PWC chambers in the program reconstruction coordinate system with the α and *beta* calibration momentum corrections. It also requires the surveyed target mid position. The error in the surveyed target mid position is dominated by the precision in the parameters which transform from the survey coordinate system into the program reconstruction coordinate system. Figure 3.5 shows the projected x target position versus the labeled targeting angle. The full spread of all the points in the plot imply an uncertainty of 0.13 % in the HTM Ptk. In order to close the $\approx$ 0.1 % HTM Ptk precision the new HTM magnetic field map should confirm the today Ptk values with the required precision.

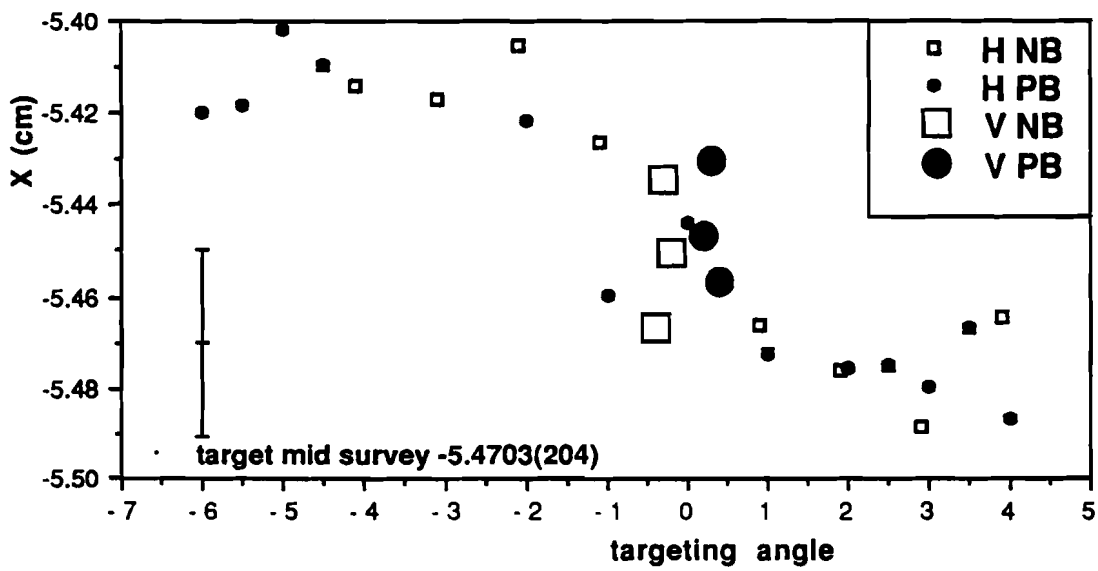

Figure 3.5: $T1PS$-Alignment projected into the Target x Center.

generates the best center position for the target. These center values are installed in the E761 offline data base. The fit is made to the best present known target position.

Table 3.3: Hyperon x and y Target Position, Momentum and σ.

Positive Hyperon Beam							
Horizontal Targeting Mode							
nominal targeting angle		Hyperon at Target (cm)				Hyperon momentum	
		x		y			
		center	σ	center	σ	p (GeV/c)	σ
HPB	-6.0	-5.3875	0.0499	-0.1597	0.0438	384.2	16.4
HPB	-5.5	-5.3861	0.0494	-0.1606	0.0443	385.3	16.7
HPB	-5.0	-5.3758	0.0508	-0.1505	0.0453	387.9	17.4
		-5.3844	0.0529	-0.1602	0.0464		
HPB	-4.5	-5.3837	0.0503	-0.1542	0.0459	387.0	16.8
HPB	-2.0	-5.3894	0.0534	-0.1306	0.0443	389.0	16.8
HPB	-1.0	-5.4303	0.0504	-0.0936	0.0248	380.3	14.4
HPB	0.0	-5.4150	0.0519	-0.1308	0.0432	380.1	14.7
HPB	+1.0	-5.4449	0.0519	-0.1328	0.0434	374.3	14.1
HPB	+2.0	-5.4434	0.0536	-0.1357	0.0422	372.9	14.1
HPB	+2.5	-5.4453	0.0550	-0.1512	0.0449	372.2	14.3
HPB	+3.0	-5.4508	0.0531	-0.1594	0.0437	370.8	14.0
		-5.4505	0.0556	-0.1584	0.0460		
HPB	+3.5	-5.4350	0.0556	-0.1595	0.0436	372.5	14.5
HPB	+4.0	-5.4509	0.0545	-0.1579	0.0427	370.2	14.1
Vertical Targeting Mode							
VPB	+3.0	-5.4316	0.0512	-0.1352	0.0430	379.1	14.6
VPB	0.0	-5.4138	0.0502	-0.1690	0.0492	383.4	14.5
VPB	-3.0	-5.4422	0.0509	-0.1839	0.0455	377.9	14.2
Negative Hyperon Beam							
Horizontal Targeting Mode							
HNB	-4.0	-5.3650	0.0524	-0.1511	0.0460	385.1	17.2
HNB	-3.0	-5.3644	0.0501	-0.1554	0.0507	387.4	15.3
HNB	-2.0	-5.3590	0.0507	-0.1301	0.0450	385.8	14.7
HNB	-1.0	-5.3827	0.0499	-0.1515	0.0608	380.9	14.3
HNB	0.0	-5.4040	0.0545	-0.1267	0.0380	373.6	13.8
HNB	+1.0	-5.4138	0.0523	-0.1588	0.0511	373.8	13.7
HNB	+2.0	-5.4210	0.0532	-0.1503	0.0458	372.8	13.8
HNB	+3.0	-5.4389	0.0538	-0.1477	0.0429	369.3	13.7
HNB	+4.0	-5.4193	0.0572	-0.1417	0.0420	368.9	13.8
Vertical Targeting Mode							
VNB	-3.0	-5.4160	0.0513	-0.1361	0.0426	376.9	13.9
VNB	0.0	-5.3863	0.0496	-0.1482	0.0416	380.7	14.4
VNB	+3.0	-5.4159	0.0516	-0.2206	0.0435	377.4	13.7

3.6 Polarization

3.6.1 Polarization Measurement Technique

The measurement of polarization is obtained from purely experimental data using a pair of symmetric targeting angles and proper handling of the hyperon beam phase space to cancel the acceptances. No Monte Carlo simulation was required or used on this analysis.

The baryon angular distribution in the hyperon CM system was expressed in the polarization theory section as:

$$\frac{dN}{d\Omega} = a(\Omega)N_0\frac{1}{4\pi}(1 + \vec{A} \cdot \hat{p}_b)$$

where:

$\vec{A}$ is the asymmetry defined as $\vec{A} = \alpha \vec{\mathbf{P}}$,
$\vec{\mathbf{P}}$ is the hyperon polarization vector,
$\Sigma^+ \rightarrow p\pi^0$ α parameter is -0.980 ± 0.016 [1],
$\bar{\Sigma}^- \rightarrow \bar{p}\pi^0$ α parameter is $+0.980 \pm 0.016$,

$\hat{p}_b$ is a unit vector along the baryon momentum in the hyperon CM,

N_0 is the total number of events in the sample,

$a(\Omega)$ is the acceptance of the apparatus, trigger, and analysis, which depends upon the proton direction cosines ($\cos\theta_x$, $\cos\theta_y$, $\cos\theta_z$) in the hyperon center of mass (CM) and the hyperon's laboratory angles in the decay volume (θ_{x0Y} ,θ_{y0Y}), see section 3.3.

The hyperon angles θ_{x0Y} and θ_{y0Y} are the variables used to describe the change in the beam phase space when the targeting angle is reversed. In order to control systematic errors in the extraction of asymmetries it is necessary to control the differences in acceptance caused by changes in the beam phase space when the targeting angle is changed. This is done by dividing the data into bins in beam angle space, calculating the asymmetry for each bin, and averaging those asymmetries to achieve a final result. I can now write the

baryon angular distribution for a single bin in (θ_{x0Y} ,θ_{y0Y}) as:

$$\left.\frac{dN}{d\Omega}\right|_{\theta_{x0Y}\ ,\theta_{y0Y}} = a' N_0' \frac{1}{4\pi}(1 + \vec{A} \cdot \hat{p}_b)\Big|_{\theta_{x0Y}\ ,\theta_{y0Y}}$$

where: a' is the acceptance of the apparatus, trigger, and analysis, which depends now on the proton direction cosines only. Inside a bin of (θ_{x0Y} ,θ_{y0Y}) the acceptance is constant with respect to these variables. N_0' is the total number of events inside a bin (θ_{x0Y} ,θ_{y0Y}).

The distribution of events in a given direction cosine, let's say $\cos\theta_y$, is obtained by integrating in ϕ. The angle ϕ lies on the plane perpendicular to $\hat{y}$. If the acceptance is constant in ϕ only the $\cos\theta_y$ component is left after integration. In the same way three independent distributions can be written as ($i = x, y, z$):

$$\left.\frac{dN}{d\cos\theta_i}\right|_{\theta_{x0Y}\ ,\theta_{y0Y}} = a_i' N_0' \frac{1}{2}(1 + \mathbf{A_i}\ \cos\theta_i)\Big|_{\theta_{x0Y}\ ,\theta_{y0Y}} \tag{3.1}$$

The approximation of the acceptance is the standard procedure because of the ease and speed of calculations [17]. The three independent cosine distributions are the bases for the Bias Canceling Method with Arithmetic Mean (BCMAM), see appendix C.

Applying BCMAM I can write the asymmetry as:

$$\left.\frac{\frac{1}{N_0'^{(1)}}\frac{dN^{(1)}}{d\cos\theta_i} - \frac{1}{N_0'^{(2)}}\frac{dN^{(2)}}{d\cos\theta_i}}{\frac{1}{N_0'^{(1)}}\frac{dN^{(1)}}{d\cos\theta_i} + \frac{1}{N_0'^{(2)}}\frac{dN^{(2)}}{d\cos\theta_i}}\right|_{\theta_{x0Y}\ ,\theta_{y0Y}} = \mathbf{A_i}^{\ (1)}\ \cos\theta_i\Big|_{\theta_{x0Y}\ ,\theta_{y0Y}} \tag{3.2}$$

where:

upper-indices (1) and (2) refer to a pair of symmetric targeting angles.

$\vec{A}^{\ (2)} = -\vec{A}^{\ (1)}$. The polarization magnitude has a dependence on the absolute value of the $p_\perp$. The direction of the polarization is given by $\vec{\mathbf{P}} \sim \vec{p}_{p_{in}} X\, \vec{p}_{hyperon}$.
Note: The acceptance function is the same for both symmetric targeting angles.

$N_0'^{(1)}$ and $N_0'^{(2)}$ are normalization factors equal to the total number of events in each sample in a bin defined by (θ_{x0Y} ,θ_{y0Y}).

The problem of measuring the asymmetry experimentally is reduced to obtaining the event cosine distribution given in the left side of equation 3.2 and making the fit to obtain $\mathbf{A_i}$ for a single bin in (θ_{x0Y} ,θ_{y0Y}). Experimentally $\frac{dN^{(j)}}{d\cos\theta_i}$ is the number of events in a $\cos\theta_i$, θ_{x0Y} , and θ_{y0Y} bin. A final step is to average $\mathbf{A_i}$ over all the bins in (θ_{x0Y} ,θ_{y0Y}):

$$\mathbf{A_i}^{(1)} = \quad < \mathbf{A_i}^{(1)}\Big|_{\theta_{x0Y}\ ,\theta_{y0Y}} >$$

Figure 3.6 shows the Σ^+ and $\bar{\Sigma}^-$ cosine distributions for a sample of targeting angles.

3.6.2 Hyperon Phase Space

As explained in the above lines the measured asymmetry is the average of subsample in bins of θ_{x0} and θ_{y0} hyperon variables. Inside each bin the acceptance function is the same for each symmetric targeting angle. Figure 3.7 shows the θ_{x0} and θ_{y0} event distributions. These distributions differ by targeting angle due to the HTM geometrical acceptance. These variables are uncorrelated.

The event distributions of x_f and $p_\perp$ for a sample of targeting angles is shown in figure 3.8. These variables are correlated in horizontal targeting angle and they overlap in the central region. The variables are not correlated in vertical targeting angle and they fully overlap.

3.6.3 Polarization and Targeting angle Sign

In this section the relation of the polarization sign given by (equation 1.1):

$$\vec{\mathbf{P}} \sim \vec{p}_{p\,incident} \times \vec{p}_{hyperon}$$

at the production point is checked against the event distributions.

In horizontal targeting angle mode the polarization is parallel to $\hat{y}$. Figure 3.9 shows the Σ^+ $\cos\theta_y$ distribution for nominal -5.0 and +3.0 targeting

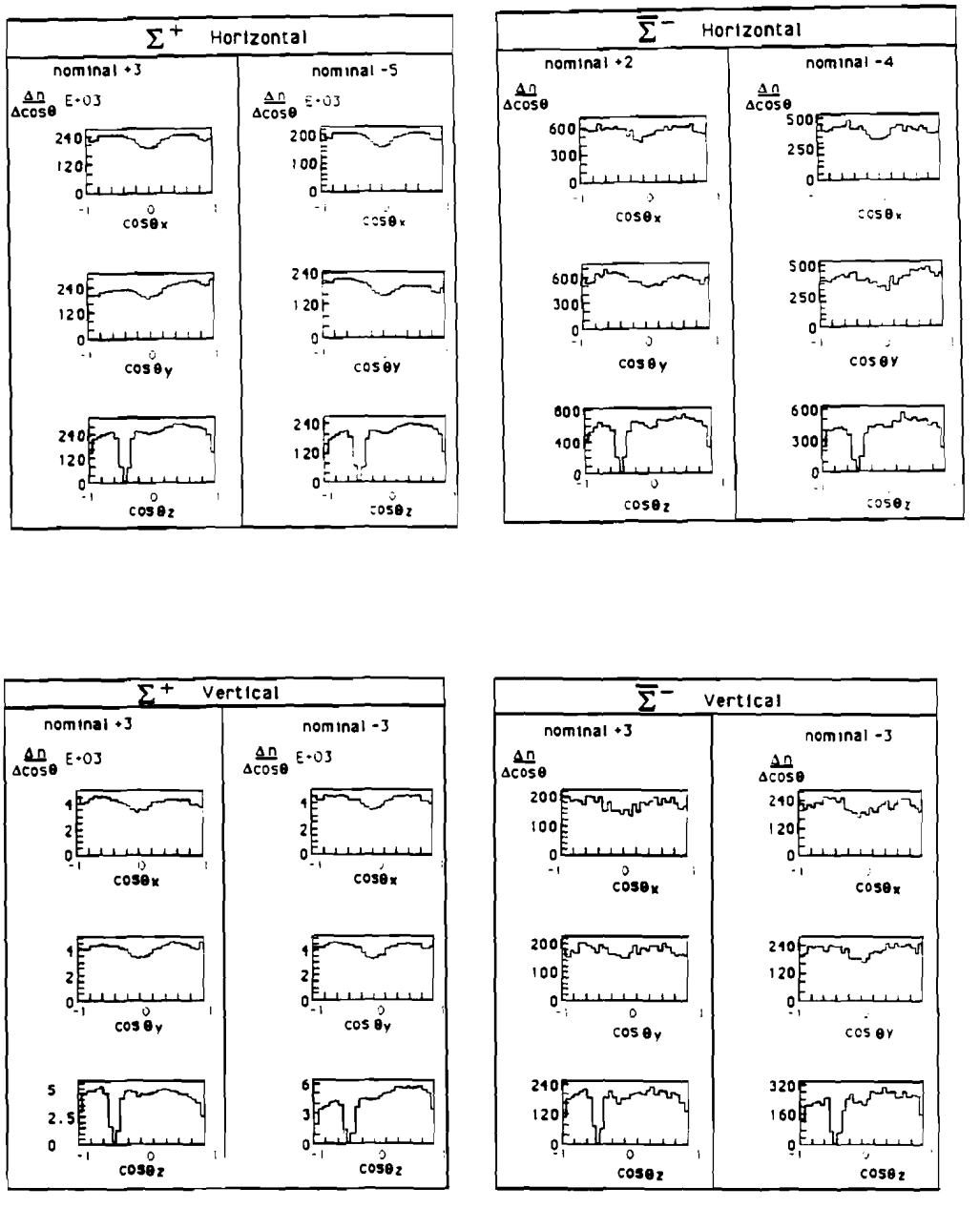

Figure 3.6: Cosine Event Distributions.

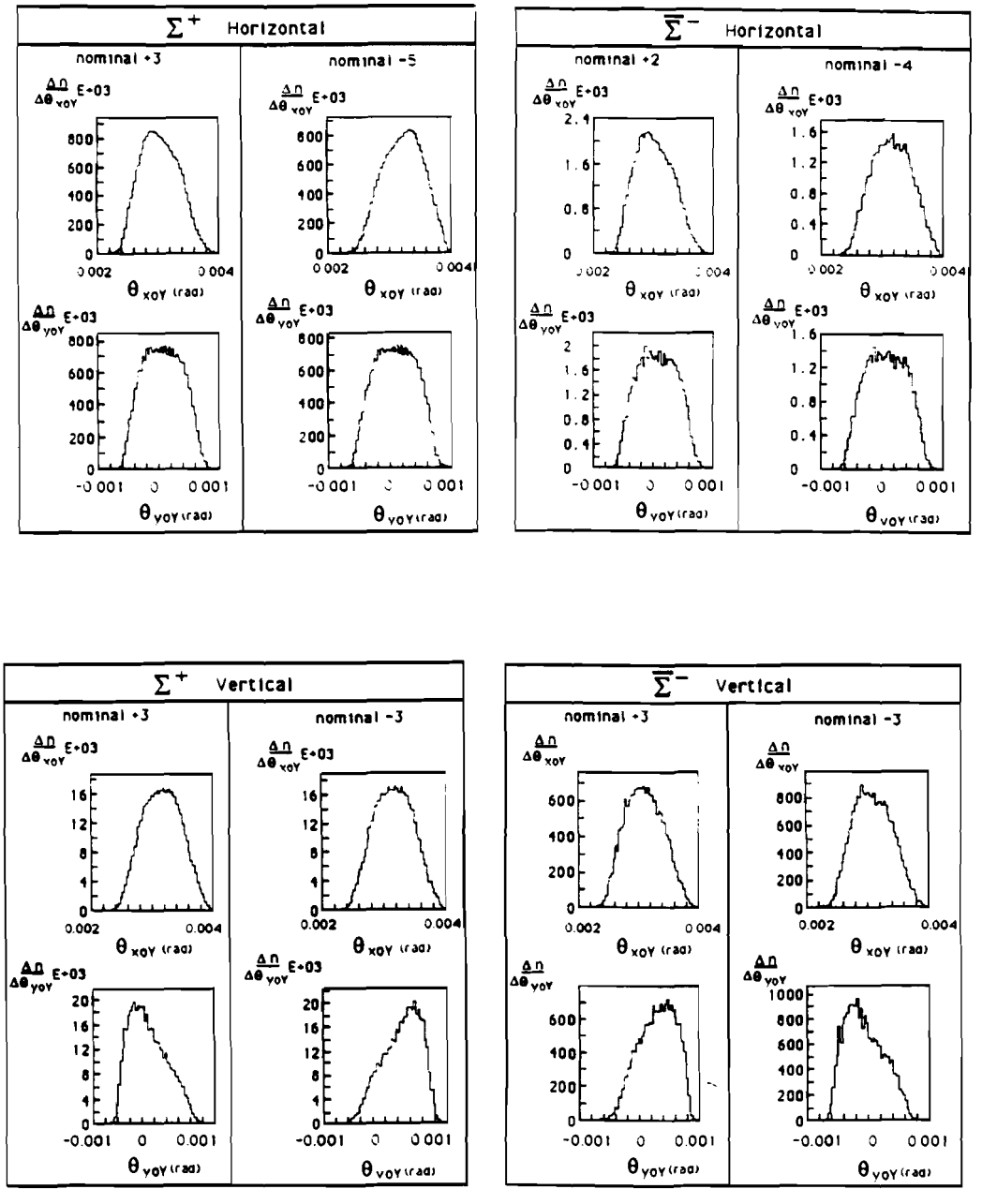

Figure 3.7: Event Distribution in θ_{x0} and θ_{y0} .

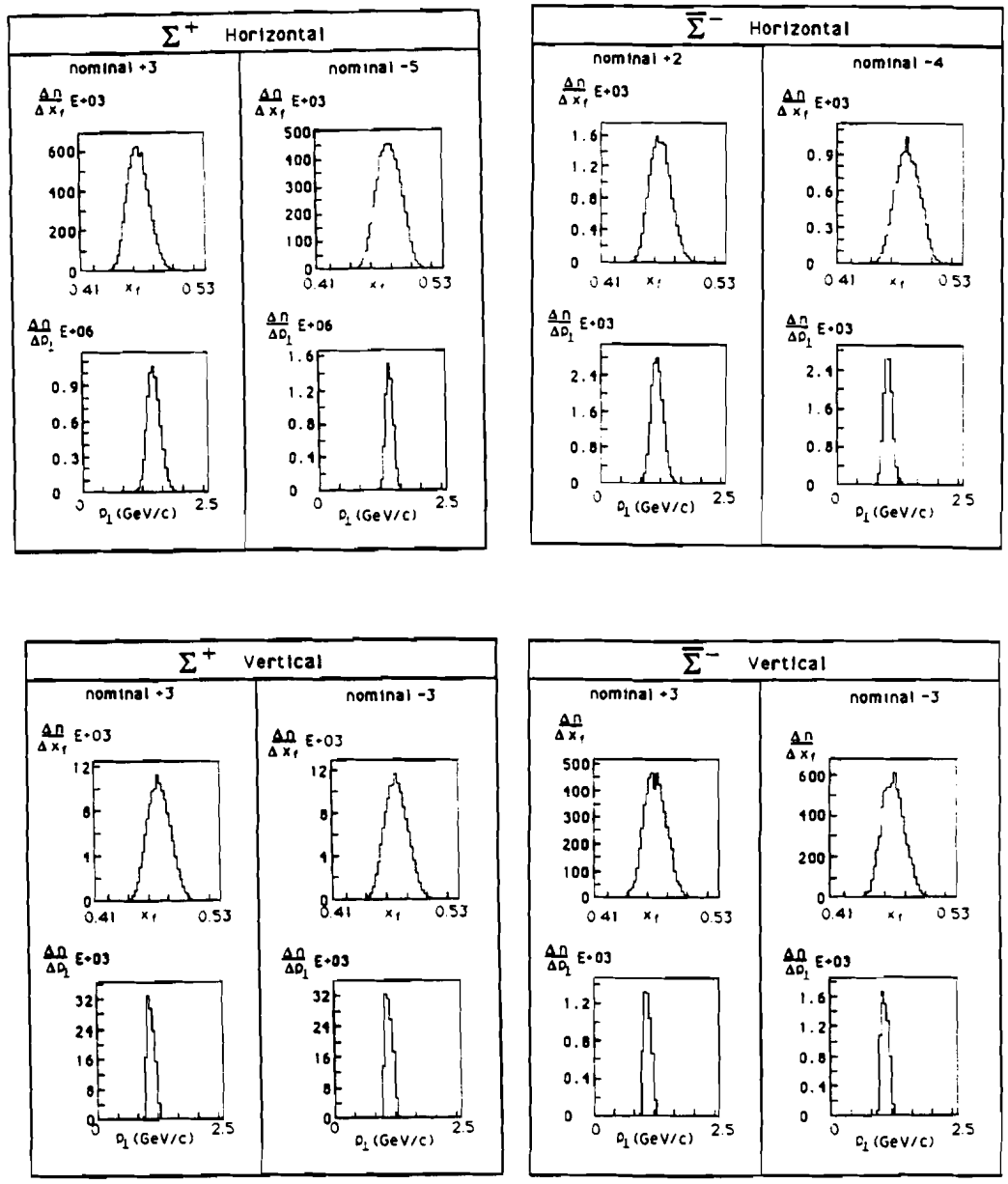

Figure 3.8: Event Distribution in x_f and $p_\perp$.

angles. The slope of the distribution is proportional to the asymmetry. The polarization has opposite sign as the asymmetry ($\alpha < 0$), it is sketched in the same figure. The trajectory of the incident beam proton is also sketched and right next to it is the cross product 1.1 for the polarization. The figure concludes that the incident proton beam direction and the cosine distribution are in agreement for the polarization sign. Nominal positive targeting angle produces the polarization pointing $-\hat{y}$, and viceversa for the nominal negative targeting angle.

Figure 3.10 shows equivalent plots for $\bar{\Sigma}^-$ horizontal targeting angle. In $\bar{\Sigma}^-$ $\alpha > 0$. The figure also concludes the agreement in the incident proton direction and the cosine distributions for the polarization sign. The polarization sign of $\bar{\Sigma}^-$ is the same as Σ^+ .

The vertical targeting angle can not use the cosine distributions since the polarization precessed in the magnetic field of HTM and HYPE2. The magnitude of polarization after precession is preserved but the information on the polarization direction at the production point from the baryon cosine distribution is lost. Rather, the θ_{y0} hyperon distribution is used. If the θ_{y0} event distribution is more populated in the $+\theta_{y0}$ than in the $-\theta_{y0}$ then the incident proton beam was entering into the positive quadrant, and viceversa for the opposite case [4] .

Figures 3.11 and 3.12 show the θ_{y0} distributions, incident proton direction, and the polarization vector at production point. The nominal +3 and -3 vertical targeting angles in Σ^+ and $\bar{\Sigma}^-$ are inverted, this effect goes back to the polarities of the beam dipole magnets, see tables 2.1 and 3.2.

3.6.4 Acceptance Function

The acceptance function can be obtained from equation 3.1. Applying equation 3.1 for each targeting angle the acceptance can be written as ($i = x, y, z$ and no θ_{x0Y} ,θ_{y0Y} binning applies):

$$\frac{1}{N_0^{(1)}}\frac{dN^{(1)}}{d\cos\theta_i} + \frac{1}{N_0^{(2)}}\frac{dN^{(2)}}{d\cos\theta_i} = a_i$$

[4]The hyperon production is maximal in the direction parallel to the incident proton beam. In a separate study, the same targeting angle data used in this thesis confirms the statement.

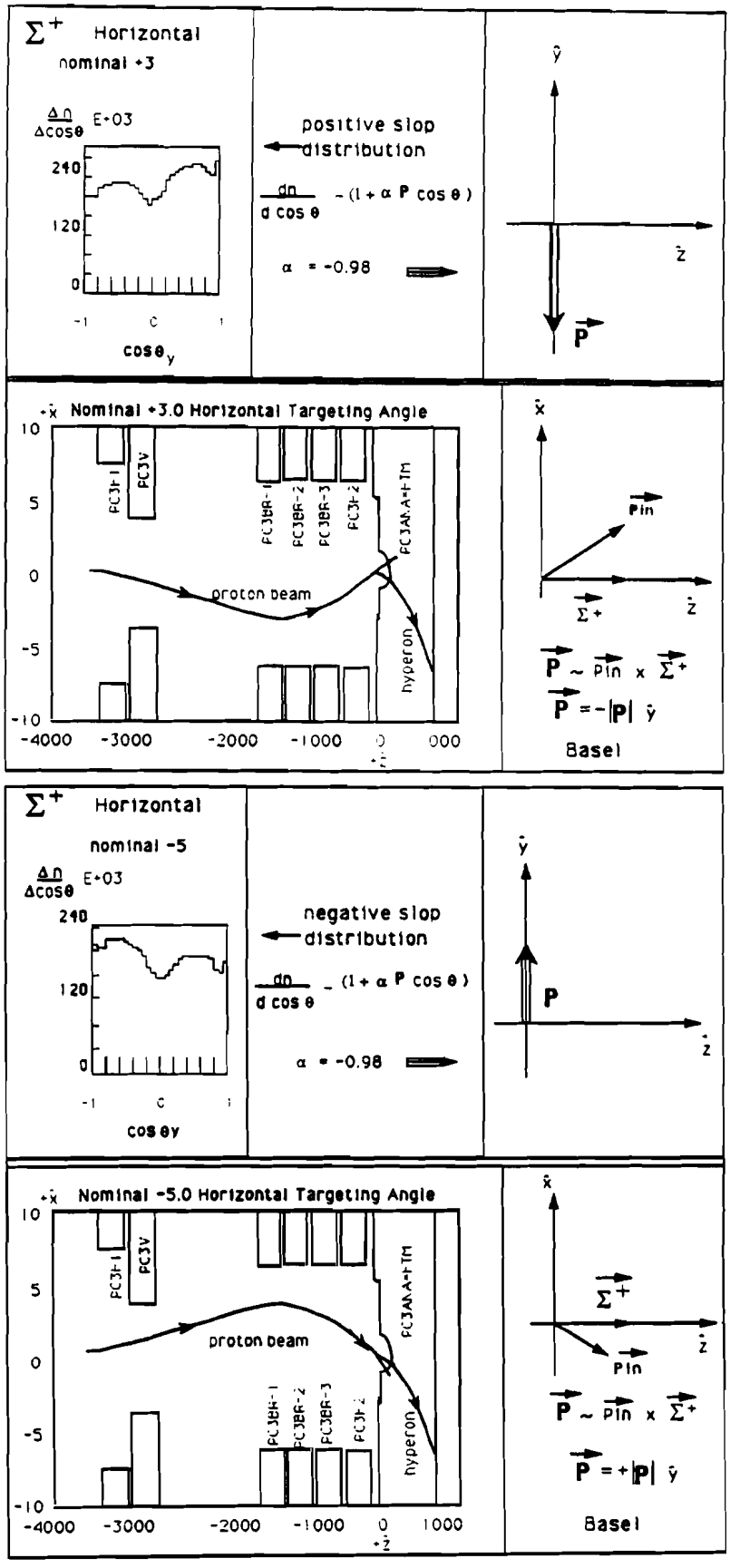

Figure 3.9: Horizontal Σ^+ Polarization and Targeting Angle Signs.

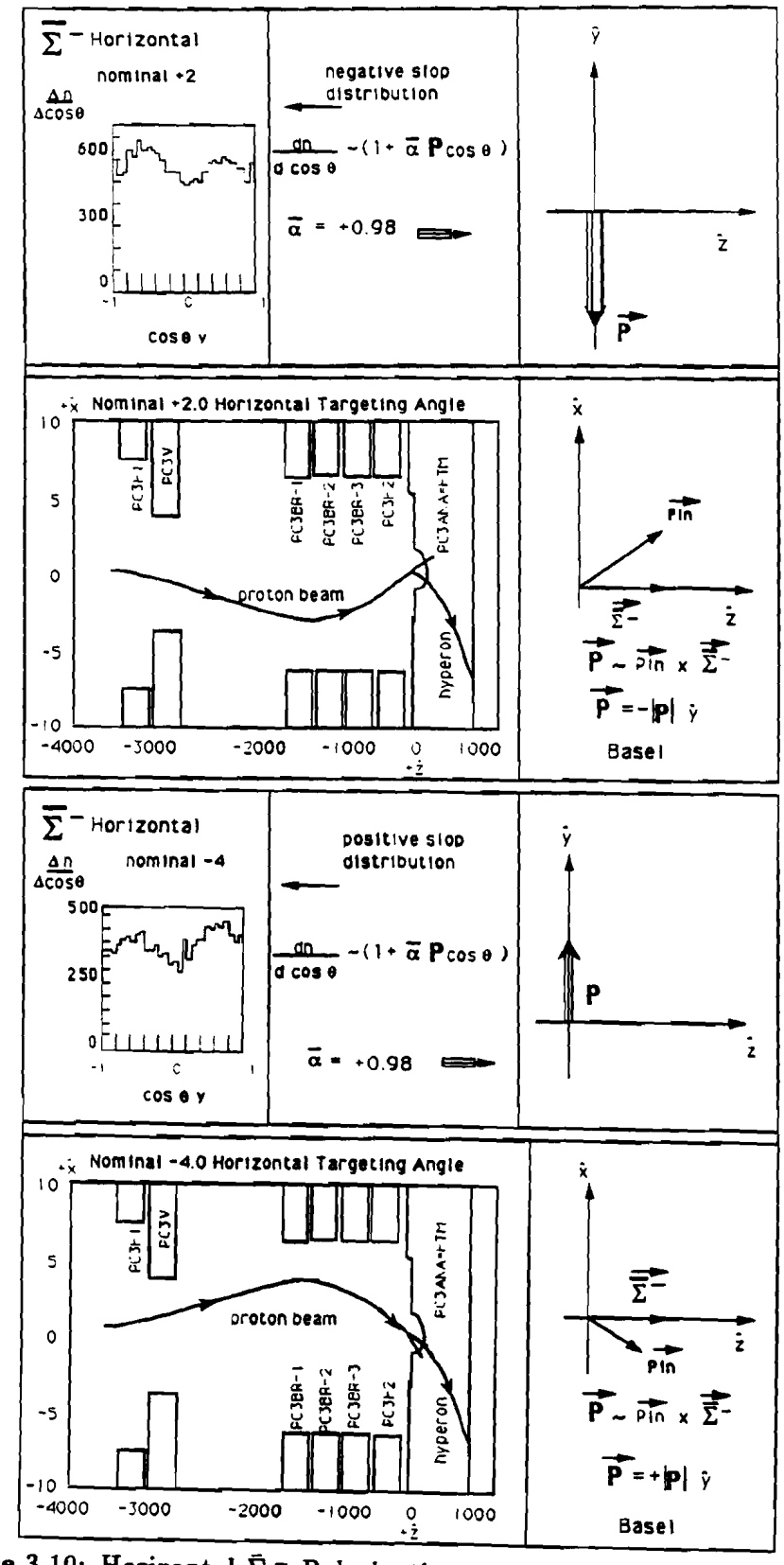

Figure 3.10: Horizontal $\bar{\Sigma}^-$ Polarization and Targeting Angle Signs.

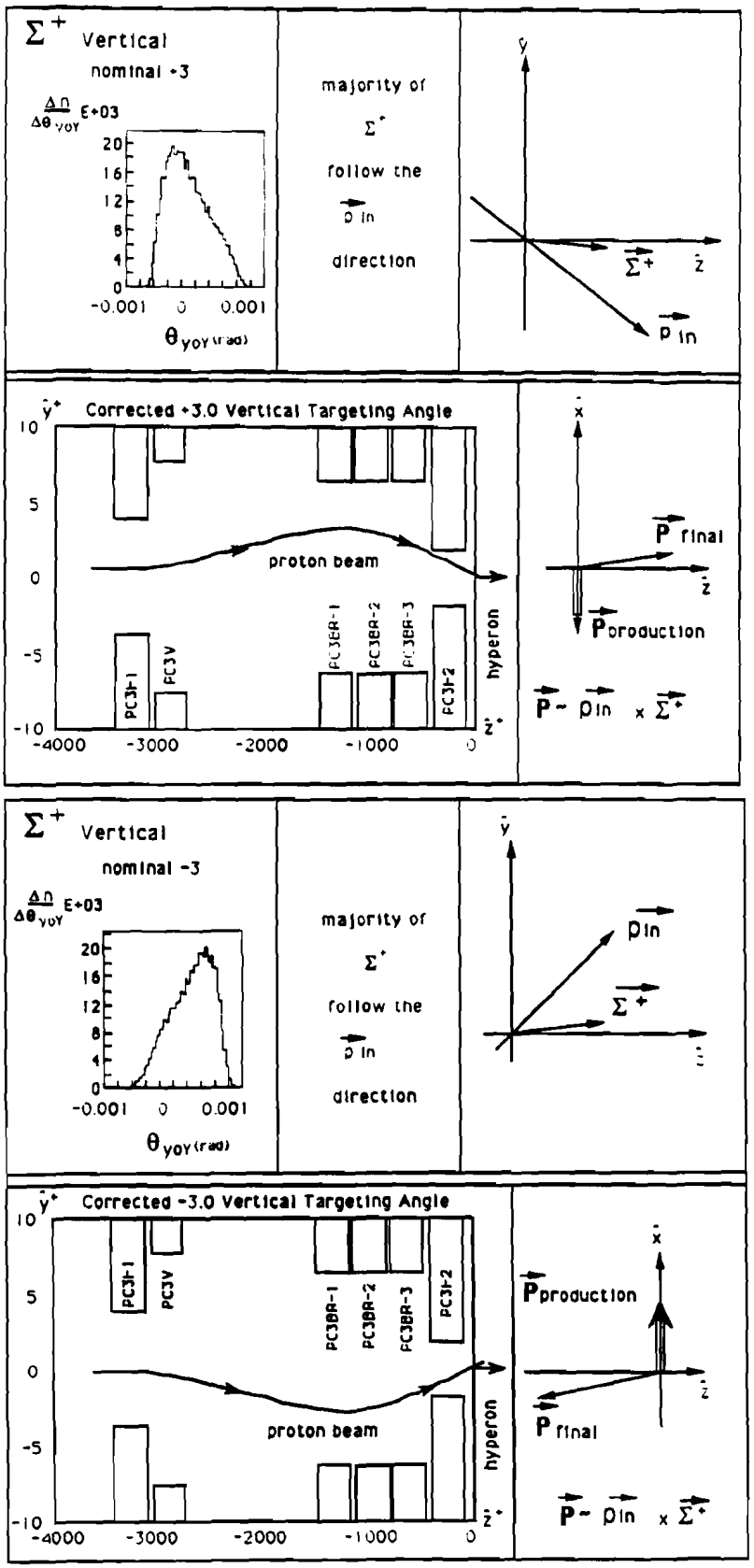

Figure 3.11: Vertical Σ^+ Polarization and Targeting Angle Signs.

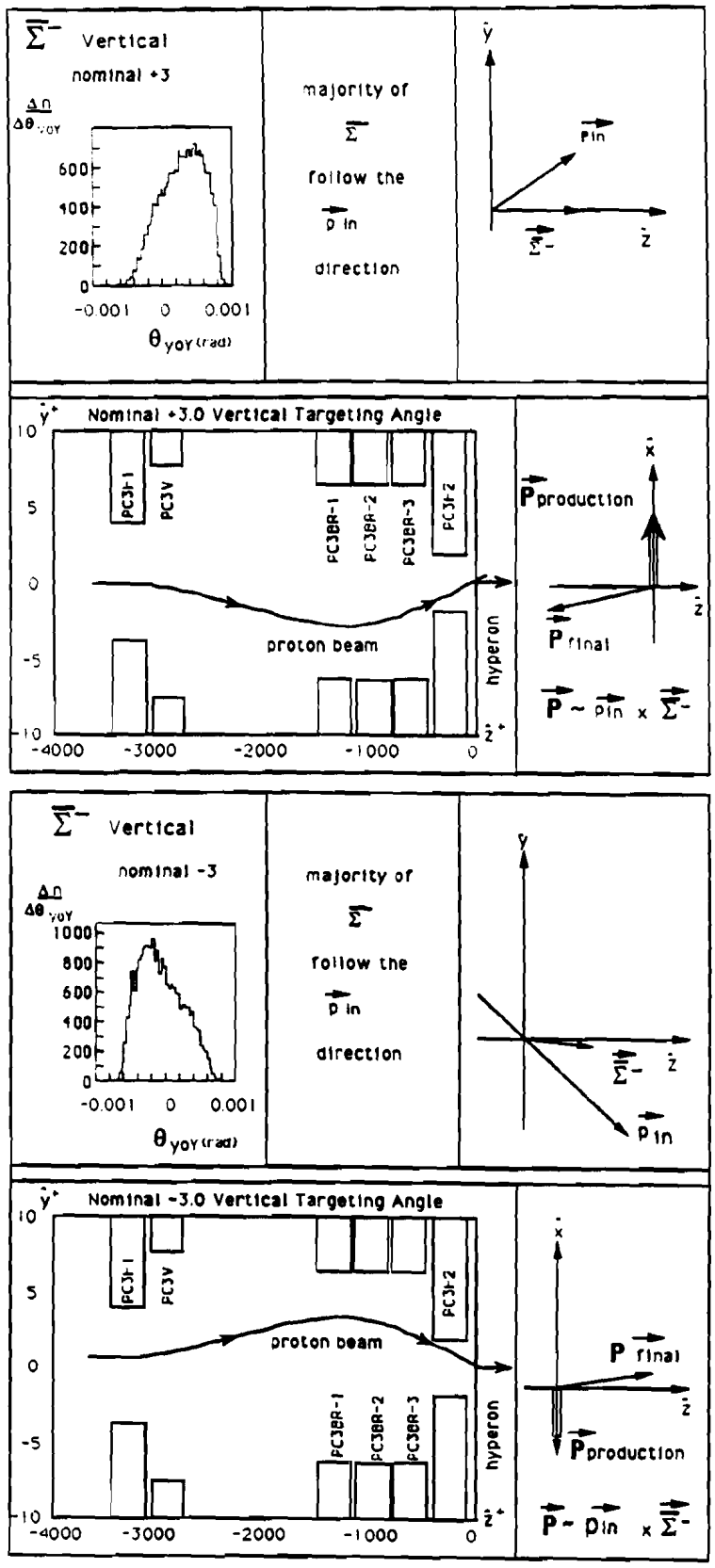

Figure 3.12: Vertical $\bar{\Sigma}^-$ Polarization and Targeting Angle Signs.

where:

Upper-indices (1) and (2) refer to a pair of symmetric targeting angles.

$\vec{A}^{(2)} = -\vec{A}^{(1)}$.

$a^{(1)} = a^{(2)} = a$.

$N_0^{(1)}$ and $N_0^{(2)}$ are normalization factors equal to the total number of events in each sample.

Figure 3.13 shows the acceptance function for a sample of targeting angles.

3.6.5 Comparing Arithmetic and Geometric Mean

In appendix C is shown that the arithmetic and geometric way of canceling the acceptance is different in each case. For both the asymmetry expression can be written as (equations C.4 and C.7):

$$\epsilon_i = \mathbf{A}^{(1)} z_i$$

In the geometric mean ϵ is written as (equation C.7):

$$\epsilon_i = \frac{\sqrt{N_i^{(1R)} N_i^{(2L)}} - \sqrt{N_i^{(1L)} N_i^{(2R)}}}{\sqrt{N_i^{(1R)} N_i^{(2L)}} + \sqrt{N_i^{(1L)} N_i^{(2R)}}}$$

It does not use the normalization of the events. Small variations on polarization and acceptance cancel to first order.

In the arithmetic mean ϵ is written as (equation C.5):

$$\epsilon_i = \frac{x_i - y_i}{x_i + y_i}$$

where:

i makes reference to the bin ith in $\cos\theta$,

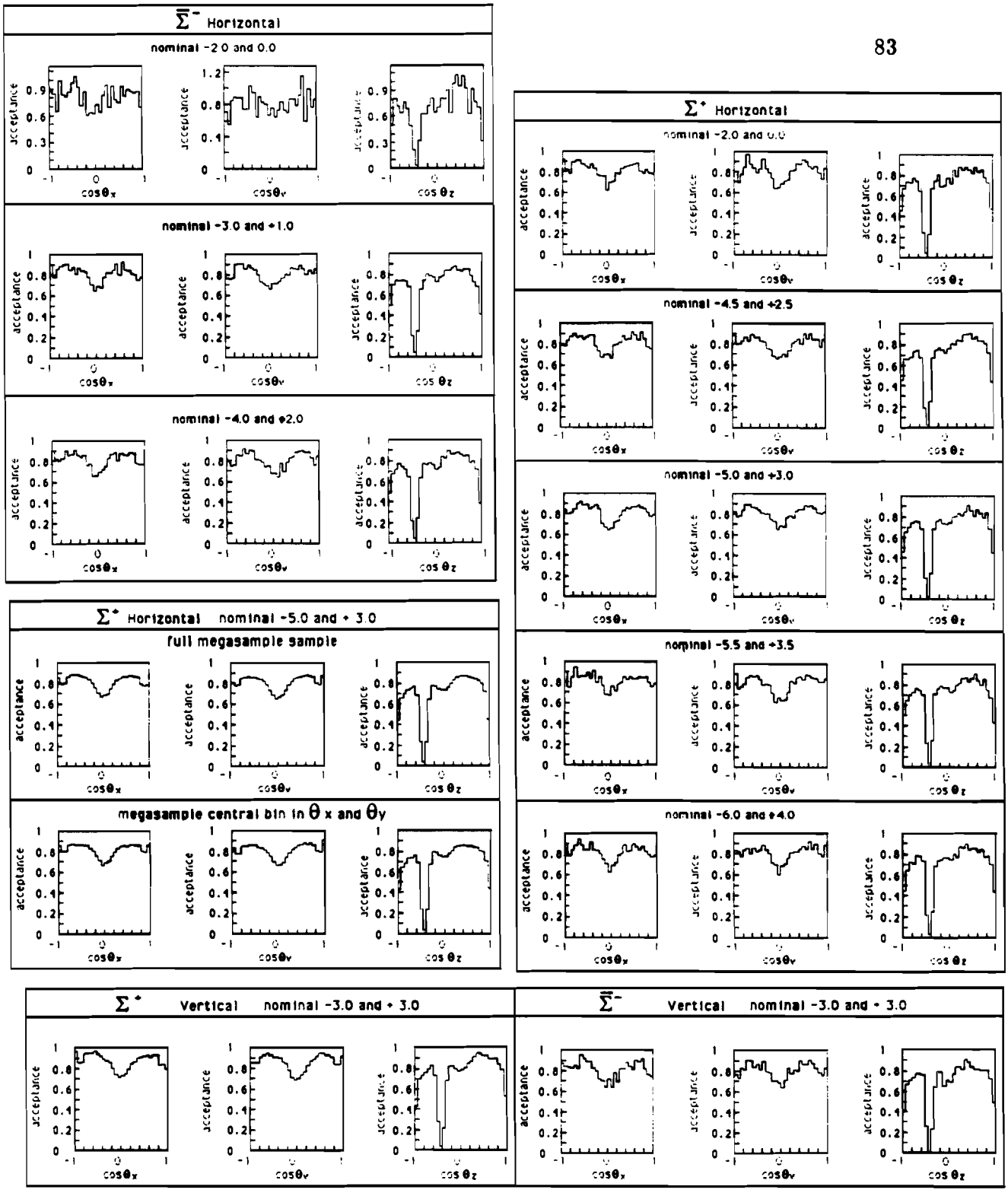

Figure 3.13: Acceptance Function from Data.

$$x_i = \frac{N_i^{(1)}}{N_0^{(1)}} \quad , \quad N_0^{(1)} = \sum_{k=1}^{m} N_k^{(1)},$$

$$y_i = \frac{N_i^{(2)}}{N_0^{(2)}} \quad , \quad N_0^{(2)} = \sum_{k=1}^{m} N_k^{(2)}.$$

It uses the normalization of events. Small variations on polarization and acceptance do not cancel to first order.

The hyperon x and y at SD3 cut was applied originally to request a full baryon acceptance on the photon detector hole for all the events which passed the mentioned cut. It came later that only when that cut was applied the arithmetic and geometric mean had a perfect match, within the statistical error. Table 3.4 shows the asymmetry with the arithmetic and geometric mean for a sample of data.

Table 3.4: Asymmetry using Arithmetic and Geometric Mean.

Horizontal Nominal +3 -5 Σ^+						
	Arithmetic			Geometric		
	A	σ	χ^2_ν/ν	**A**	σ	χ^2_ν/ν
$\mathbf{A_x}$	-0.0011	0.0005	2.23/15	-0.0011	0.0005	2.16/16
$\mathbf{A_y}$	-0.1212	0.0005	6.13/15	-0.1212	0.0005	6.06/16
$\mathbf{A_z}$	0.0014	0.0005	1.43/15	0.0014	0.0005	1.16/15
Vertical Nominal +3 -3 Σ^+						
$\mathbf{A_x}$	0.0094	0.0036	0.61/11	0.0094	0.0036	0.69/14
$\mathbf{A_y}$	-0.0055	0.0036	1.00/11	-0.0056	0.0036	0.89/14
$\mathbf{A_z}$	0.1598	0.0037	1.60/11	0.1617	0.0037	1.64/14
σ is statistical only						

3.6.6 History: Asymmetry Measurement

Using a subsample, selecting randomly one event every fifty, of the megasample a historical review of the analysis is shown in figure 3.14. The historical analysis did not include the hyperon x and y SD3 cuts. Notice the inversion on the asymmetry sign on all components. In the following lines I explain each one of the 10 asymmetry entries.

Entry 1 Binning the data only in θ_{x0} (60,60 bins in cos and θ_{x0}).

Entry 2 Binning the data in θ_{x0} and θ_{y0} (30,16,16 bins in cos, θ_{x0} , and θ_{y0}).

Entry 3 Three σ x and y target cut.

Entry 4 Removal of K^+ with binning as 2 and target as 3.

Entry 5 Fine correction on target constants with 2,3, and 4.

Entry 6 Binning 15,8,8, in cos, θ_{x0} , and θ_{y0} with 3 and 4.

Entry 7 Re-fitting events, with 6.

Entry 8 Replay DST (Data Summary Tape) 7.

Entry 9 Fine momentum calibration and target in the fit, with 2 and 4.

Entry 10 Replay DST 9.

The asymmetry in y or polarization is stable as soon as the θ_{x0} and θ_{y0} binning, target cuts, and K^+ removal is made. This set of measurements shows negligible effect when the target and fine momentum calibration are inserted in the reconstruction program. Further analysis used the target cut mode. The final analysis required the hyperon x and y SD3 cut, to assure full baryon acceptance in the photon detector hole. No systematic error was assigned to these studies, since the analysis was progressively corrected.

3.6.7 Systematic: Binning in θ_{x0} and θ_{y0}

With the final set of cuts a search on optimum number of divisions for the $\cos\theta$, θ_{x0} , and θ_{y0} was made for all data sample. The more divisions there are the more identical is the acceptance in each symmetric pair of data. However, data sample with small number of events can not be highly divided. It was found that the nominal combination of 2,2,2 was adequate to cover all data sample. The nominal 2,2,2 means 15,8,8 bins in:

$$-1 < \cos\theta < 1,$$

$$0.002 < \theta_{x0} < 0.004(rad), \text{and}$$

$$-0.001 < \theta_{y0} < 0.001(rad)$$

The hyperon x and y at SD3 cut reduced the above range of data in θ_{x0} and θ_{y0} such that only the four central divisions contain events.

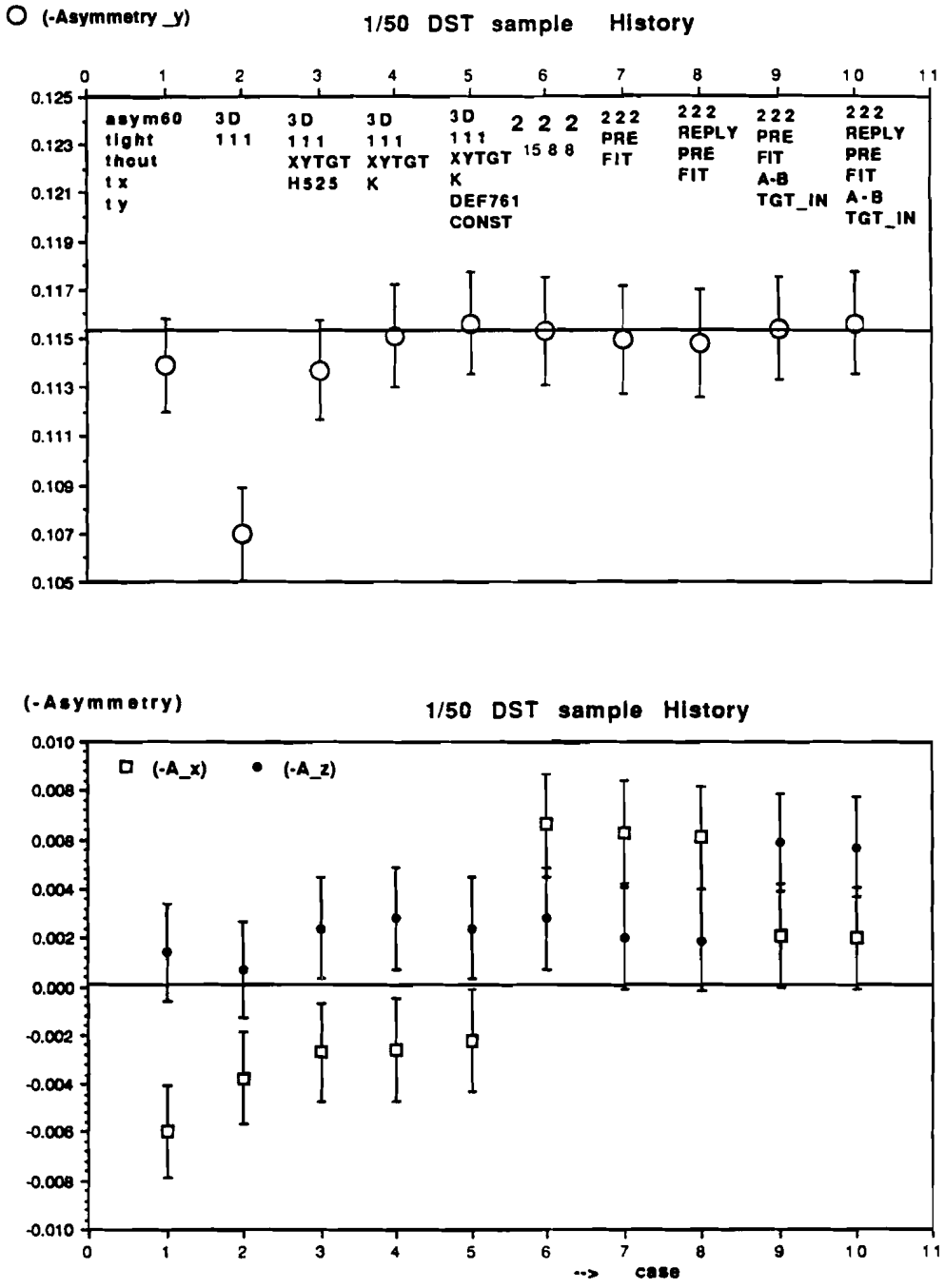

Figure 3.14: Historical Asymmetry Review.

A systematic error limit in the asymmetry is taken from the y asymmetry in the megasample data. The limit is the largest difference, with respect the 2,2,2 binning, of all combination of divisions in the y asymmetry. The systematic error is 0.0010 in the asymmetry.

3.6.8 Systematic: Run by Run and Variable Splitting

The asymmetry was computed for thirteen pair sets of runs increasing in real time (or run number) for the megasample. Figure 3.15 shows the asymmetry result for each set.

The asymmetry of the megasample was studied as a function of the variables:

$\theta_{x0\ Y}$, one of the analysis binning variables, 3 slices.

$\theta_{y0\ Y}$, one of the analysis binning variables, 3 slices.

r/r, set of runs, 13 sets.

z_v, 7 slices of equal statistics.

$\chi^2_{\nu Y}$, 7 slices of equal statistics.

$\chi^2_{\nu B}$, 7 slices of equal statistics.

x_Y SD3, 7 slices of equal statistics.

y_Y SD3, 7 slices of equal statistics.

x_f , 7 slices of equal statistics.

$p_\perp$, 7 slices of equal statistics.

m^2_X, neutral mass square, 7 slices of equal statistics.

x target, 7 slices of equal statistics.

y target, 7 slices of equal statistics.

The momentum of the baryon, x, and y positions of the baryon at the iron sheets are not used. The baryon momentum variables select particular pieces of the $\cos\theta$ distribution such that the asymmetry lost its meaning. The variables x_f , x target, $p_\perp$ and m^2_X affect the $\cos\theta_z$ distribution. The background tails

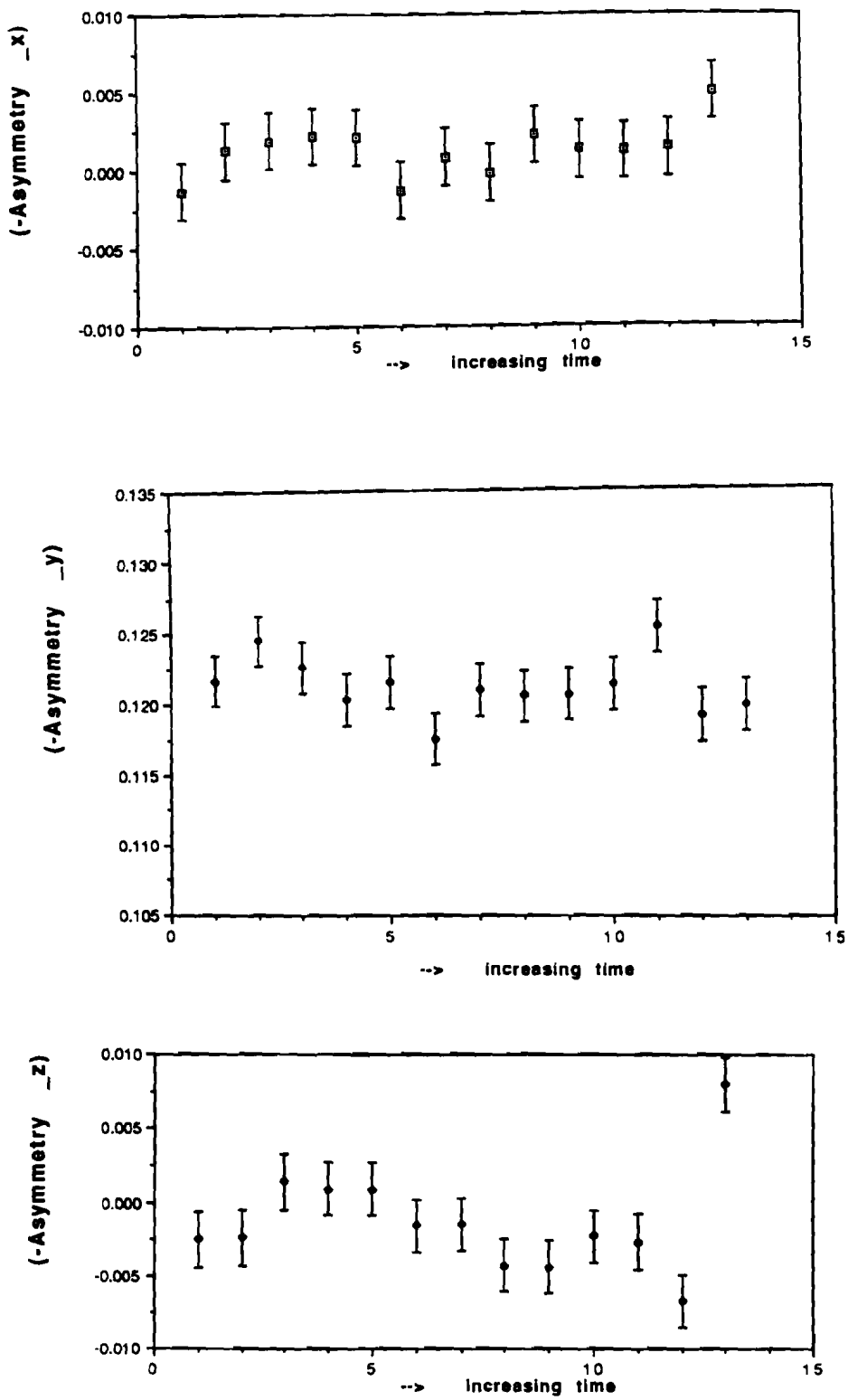

Figure 3.15: Asymmetry Versus Time.

of those variables are characterized by incorrectly measured hadronic decays. A z bias is caused by momentum errors while x and y biases depend mainly on angles. The largest class of measurement errors are errors in the hyperon momentum. Figure 3.16 show the systematic studies for the megasample data.

A systematic upper error limit in the asymmetry is taken from the standard deviation (STD). The STD is the product of the χ^2_ν times the statistical error. The systematic error is dominated by the θ_{x0} variable. There is a physical x_f dependence of the polarization at constant $p_\perp$ [5] , see figure 3.17. There is a correlation between x_f and θ_{x0} in both targeting angles such that the polarization has θ_{x0} physical dependence. The systematic error is 0.0030 in the asymmetry.

3.6.9 Polarization Σ^+

Table 3.5 shows the asymmetry for each pair of symmetric targeting angles.

The physical asymmetry in horizontal mode is $\mathbf{A_y}$. The selection order of (1) and (2) targeting angles is made such the polarization points in the $+y$ direction. For the case of nominal -5.0 and +3.0 targeting angle two numbers are shown. One of them is the polarization from a *NEGPHOTON* trigger sample (low statistics) and the second one is from *PHOTON* trigger sample. Both values agree within statistical error.

The physical asymmetry components in vertical mode are $\mathbf{A_x}$ and $\mathbf{A_z}$. The selection of (1) and (2) targeting angles is made such the polarization at production points in the $+x$ direction.

The assigned asymmetry systematic error is the same for all cases. It was obtained from the study of the megasample data. There are two contributions in the asymmetry systematic error; the binning and the variable splitting, $\pm$ 0.0010 $\pm$ 0.0030 respectively. The total contribution is $\pm$ 0.0032 in the asymmetry.

[5]Since the x_f and $p_\perp$ phase space overlap in the central region both variables can not be divided at once in the megasample data. The x_f is split while the $p_\perp$ is kept constant, and viceversa.

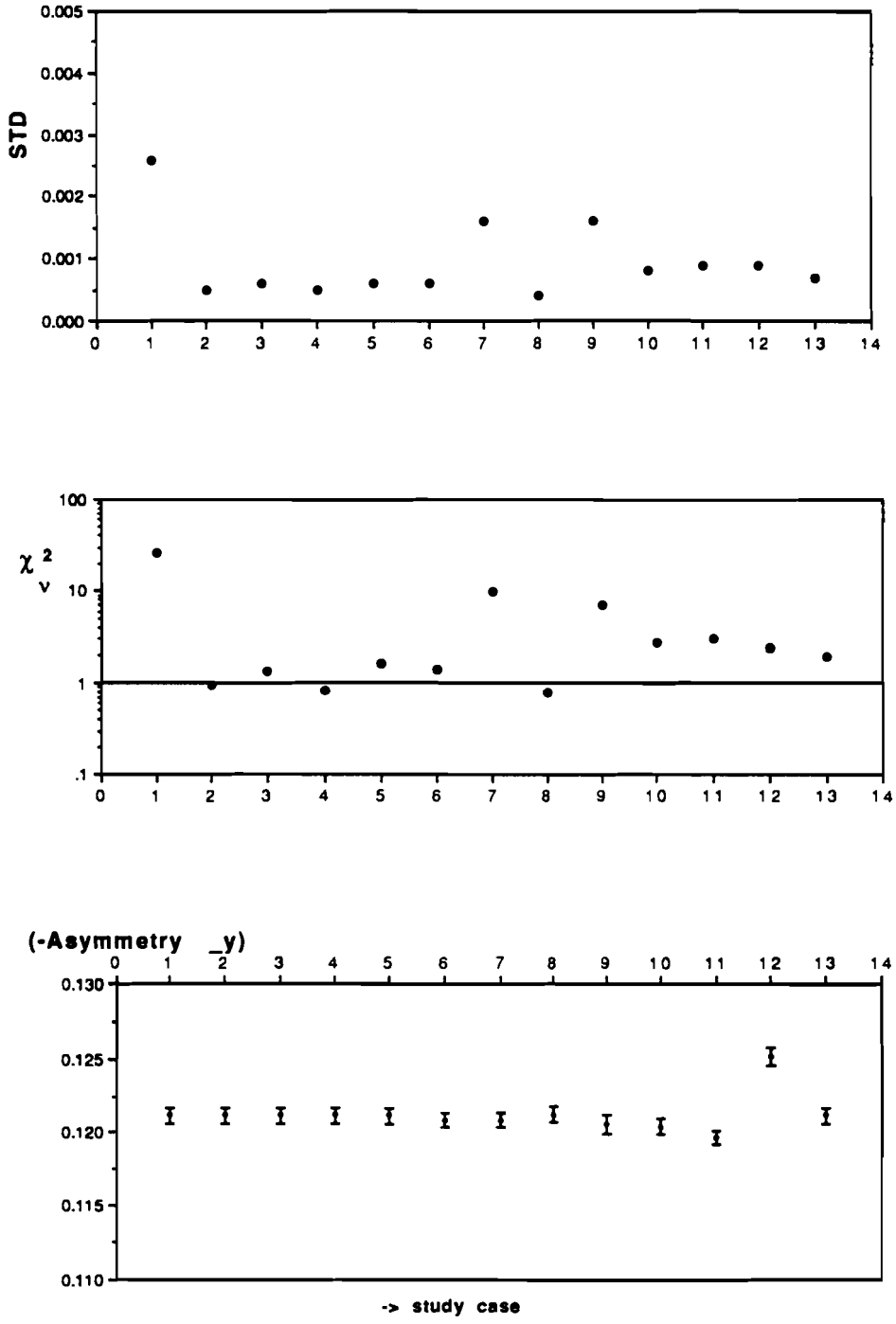

Figure 3.16: Asymmetry Study from Variable Splitting.

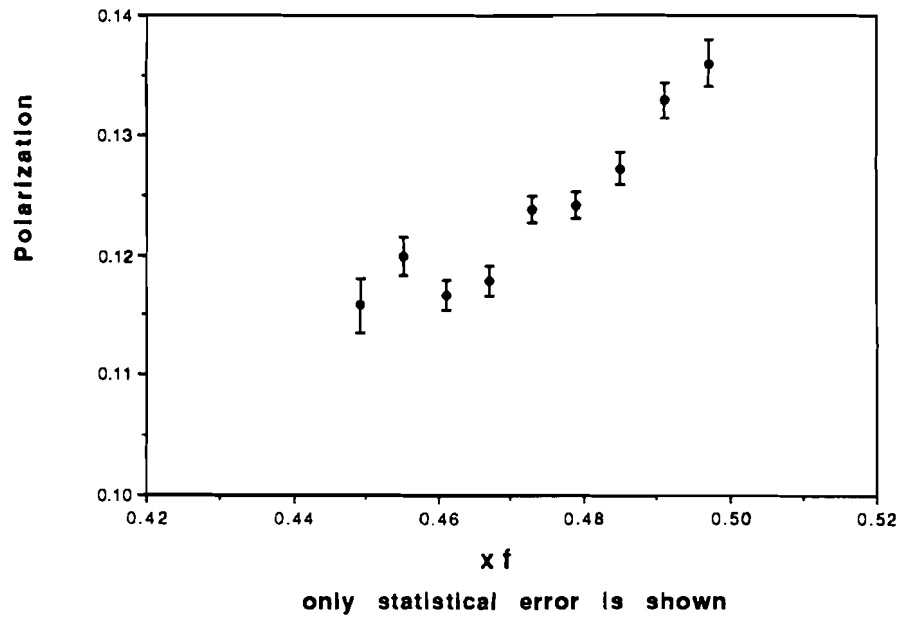

Figure 3.17: Polarization Versus x_f .

The polarization is shown in table 3.6 and in figure 3.18. Comments will follow in section 4. The x_f was 0.47 with a spread of 0.01 (σ) for the whole data sample. The propagated polarization systematic error from the asymmetry is $\pm$ 0.0032, same value for the whole data sample. The α parameter error contributes to the polarization systematic error, as shown in the table. For horizontal mode the polarization is the $\mathbf{A_y}$ /α. For vertical mode the polarization is $\sqrt{\mathbf{A_x}^{\,2} + \mathbf{A_z}^{\,2}}/\alpha$.

The megasample offers the possibility of breaking the sample into equal $p_\perp$ bins to get the polarization for each $p_\perp$ bin. Figure 3.19 shows the megasample polarization as a function of $p_\perp$, at fix x_f . Only statistical errors are shown. Comparing this plot versus figure 3.18 the slope of polarization in $p_\perp$ looks less sharp in figure 3.19. The polarization in each $p_\perp$ bin is biased by the $p_\perp$ and x_f phase space overlapping.

3.6.10 Polarization $\bar{\Sigma}^-$

Table 3.7 shows the asymmetry for each pair of symmetric targeting angles.

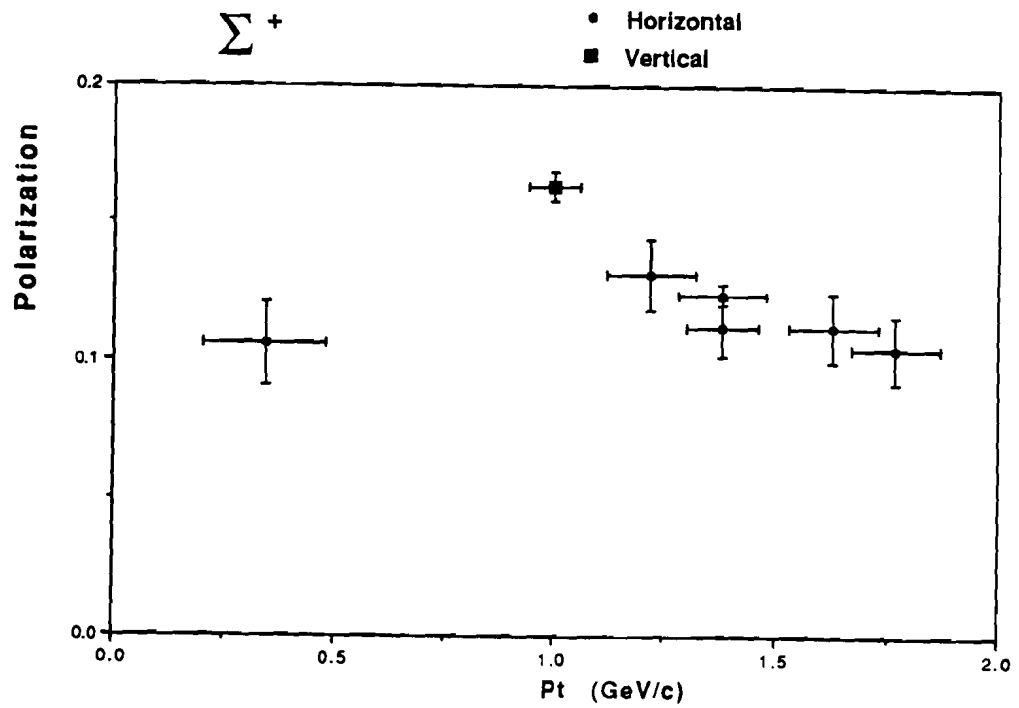

Figure 3.18: Polarization Versus $p_\perp$ for Σ^+ .

The physical asymmetry in horizontal mode is $\mathbf{A_y}$. The selection order of (1) and (2) targeting angles is made such that the polarization point in the $+\hat{y}$ direction.

The physical asymmetry components in vertical mode are $\mathbf{A_x}$ and $\mathbf{A_z}$. The selection of (1) and (2) targeting angles is made such that the polarization at production point points in the $+x$ direction.

The vertical nominal (+3,-3) and horizontal nominal (-4,2) are at the same production $p_\perp$. Their asymmetry (or polarization) agrees well within statistical error, see figure 3.20.

The asymmetry systematic error is $\pm$ 0.0032, the same for all cases. It was obtained from the study of the megasample asymmetry data.

The polarization is shown in table 3.8 and in figure 3.20. Comments will follow in section 4. The x_f was 0.47 with a spread of 0.01 (σ) for the whole data sample. The propagated polarization systematic error from the asymmetry is $\pm$ 0.0032, same value for the whole data sample. The α parameter error contributes to the systematic error, as shown in the table. For horizontal mode the polarization is the $\mathbf{A_y}$ /α. For vertical mode the polarization is $\sqrt{\mathbf{A_x}^2 + \mathbf{A_z}^2}/\alpha$.

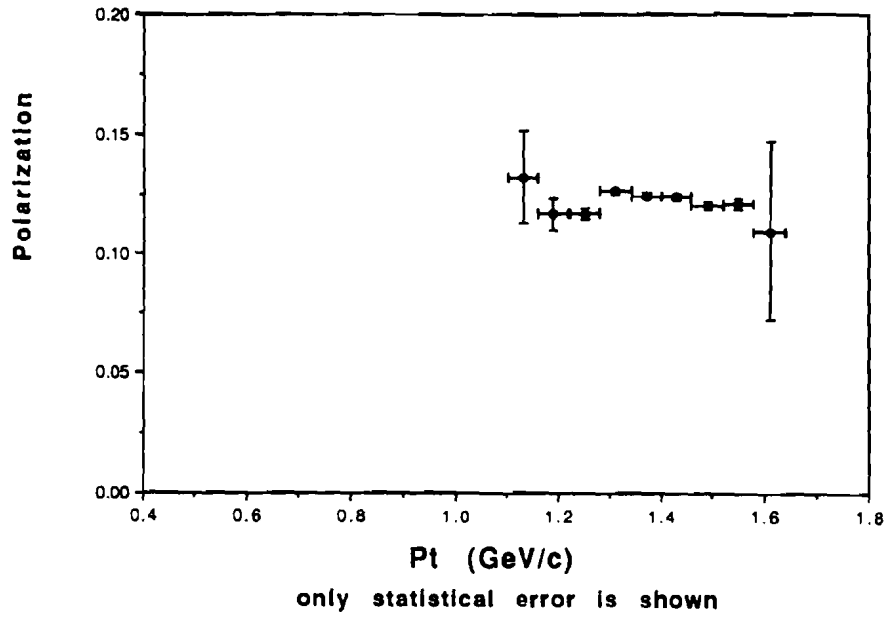

Figure 3.19: Megasample Data Polarization Versus $p_\perp$.

3.7 Magnetic Moment

3.7.1 Spin Precession Technique

Appendix D describes the rotation of the particle's spin while the charged particle itself travels through a magnetic field. Figure 3.21 sketches the precession of the polarization vector while it traverses a magnetic field. In the vertical mode the polarization vector is perpendicular to the HTM and HYPE2 magnetic field at the proton beam target interaction. The polarization at production point is parallel to axis $+\hat{x}$.

The precession angle ϕ is measured from the asymmetry ($\vec{A}$) components obtained from the data (equation D.11):

$$\phi = \arctan\left(\frac{|\mathbf{A_x}|}{|\mathbf{A_z}|}\right) + \text{quadrant correction} + n \cdot 2\pi$$

where n can not be determined with the experiment itself. The value of n is obtained from previous measurements. The sign of ϕ is positive if the rotation

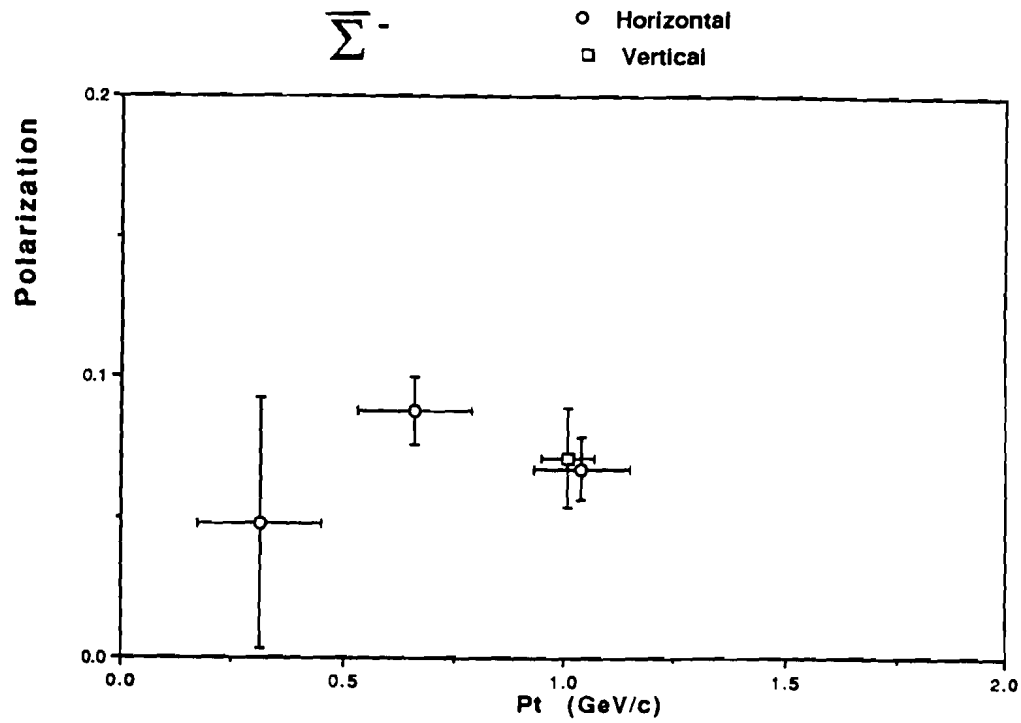

Figure 3.20: Polarization Versus $p_\perp$ for $\bar{\Sigma}^-$.

went counter-clockwise. The precession angle of the spin is (equation D.9):

$$\phi = \frac{q}{mc^2}\frac{1}{\beta}\frac{g-2}{2}\int Bdl$$

The absolute value of the magnetic moment in Nuclear Magneton units is (equation D.10):

$$|\mu| = \frac{m_p}{m}\left(1 + \beta mc^2 \frac{\phi}{\text{Ptk } c}\right)$$

3.7.2 Determination of n 2 π

The factor n (or complete turns) is determined from an observation on experiments E620 [35], E497 [34] and E761 itself. Each one of them was made at different Ptk . Figure 3.22 shows the precession angle versus the Ptk for the mentioned experiments. The plotted precession angle is the total one, the asymmetry ratio, quadrant correction, and factor n. The n E761 factor is obtained by a straight line intercepting zero and each one of the precession angles. The final result is $n = 1$. The quadrant correction is 1.5 π. Figure 3.23 shows the polarization vector at production point and after the precession.

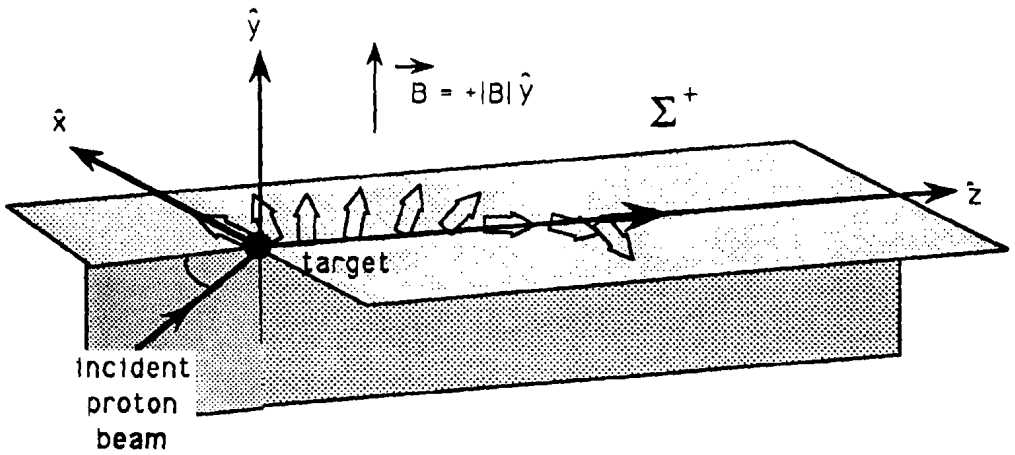

Figure 3.21: Spin Precession in a Magnetic Field.

3.7.3 History: Magnetic Moment Measurement

Using the Σ^+ vertical targeting sample a historical review of the analysis is shown in figure 3.24. The historical analysis did not include the hyperon x and y SD3 cuts. In the following lines I explain each one of the 4 magnetic moment entries.

Entry 1 Binning the data only in θ_{y0} (60,60 bins in cos and θ_{y0}).

Entry 2 Binning the data in θ_{x0} and θ_{y0} (30,16,16 bins in cos, θ_{x0} , and θ_{y0}).

Entry 3 x and y target three σ cut.

Entry 4 Removal of K^+ with binning as 2 and target as 3.

The magnetic moment is stable as soon as the θ_{x0} and θ_{y0} binning is made. The final analysis required the hyperon x and y SD3 cut, to assure full baryon acceptance in the photon detector hole. No systematic error was assigned to these studies, since the analysis was progressively corrected.

3.7.4 Systematic: Binning in θ_{x0} and θ_{y0}

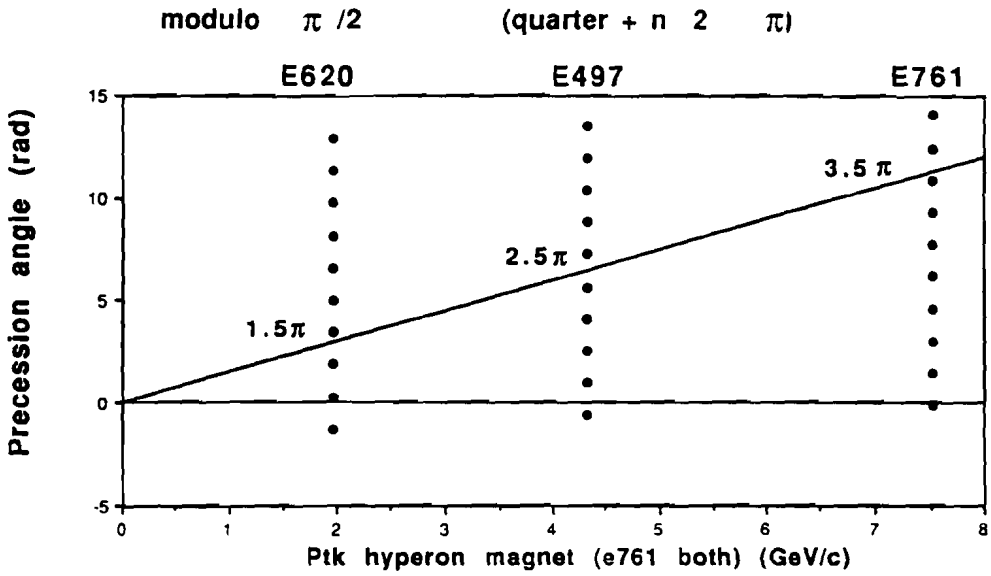

Figure 3.22: Precession Angle Versus Ptk .

With the final set of cuts a search on optimum number of divisions for the $\cos\theta$, θ_{x0} , and θ_{y0} was made for all data sample. The more divisions there are the acceptance is more identical in each symmetric pair of data. However, data sample with small number of events can not be highly divided. It was found that the nominal combination of 2,2,2 was adequate to cover all data sample. The nominal 2,2,2 means 15,8,8 bins in:

$$-1 < \cos\theta < 1,$$

$$0.002 < \theta_{x0} < 0.004(rad), \text{and}$$

$$-0.001 < \theta_{y0} < 0.001(rad)$$

The hyperon x and y at SD3 cut reduced the above range of data in θ_{x0} and θ_{y0} such that only the four central divisions contain events.

A systematic error limit in the magnetic moment is taken from the Σ^+ vertical data. The limit is the largest difference, with respect to the 2,2,2 binning, of all combination of divisions in the magnetic moment. The magnetic moment systematic error is 0.0013 μ_N .

3.7.5 Systematic: Run by Run and Variable Splitting

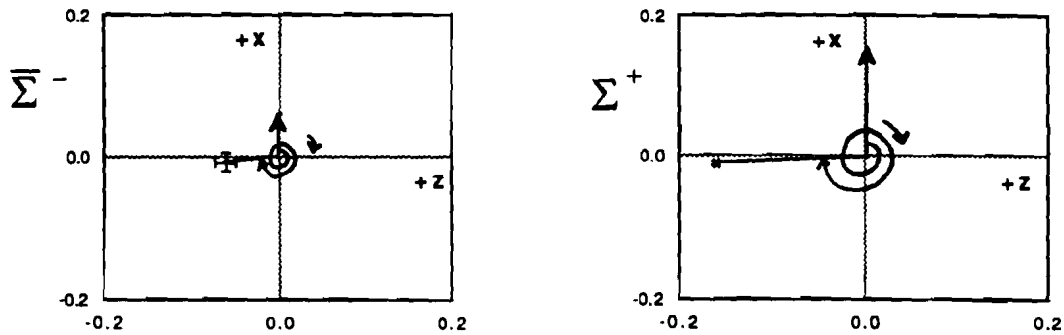

Figure 3.23: Polarization Vector Before and After Precession.

The magnetic moment was computed for four pair sets of runs increasing in real time (or run number) for the Σ^+ vertical data. Figure 3.25 shows the magnetic moment result for each set.

The magnetic moment was studied as a function of the variables:

$\theta_{x0\ Y}$, one of the analysis binning variables, 3 slices.

$\theta_{y0\ Y}$, one of the analysis binning variables, 3 slices.

r/r, set of runs, 13 sets.

z_v, 7 slices of equal statistics.

$\chi^2_{\nu Y}$, 7 slices of equal statistics.

$\chi^2_{\nu B}$, 7 slices of equal statistics.

x_Y SD3, 7 slices of equal statistics.

y_Y SD3, 7 slices of equal statistics.

x_f , 7 slices of equal statistics.

$p_\perp$, 7 slices of equal statistics.

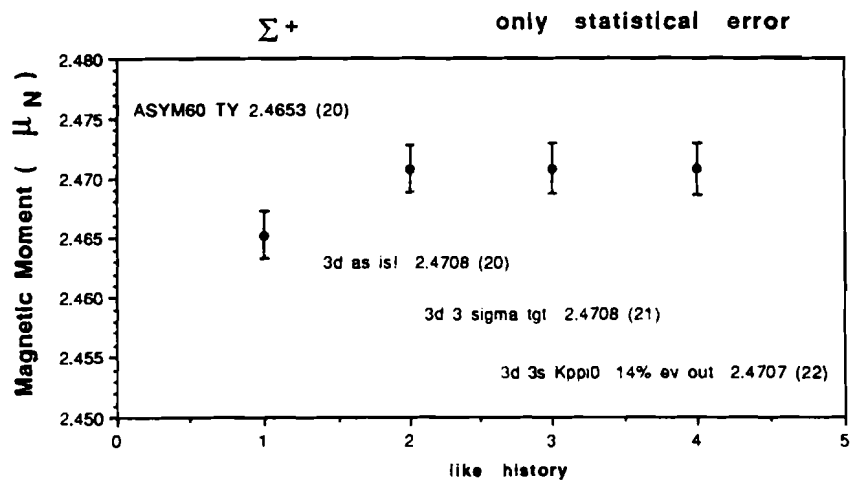

Figure 3.24: Historical Magnetic Moment Review.

m_X^2, neutral mass square, 7 slices of equal statistics.

x target, 7 slices of equal statistics.

y target, 7 slices of equal statistics.

The momentum of the baryon, x, and y positions of the baryon at the iron sheets are not used. The baryon momentum variables select particular pieces of the $\cos\theta$ distribution such that the asymmetry lost its meaning. From figure 3.26 the magnetic moment is affected only by the variables $p_\perp$ and m_X^2. The $p_\perp$ effect rises from the fact that events are being lost due to the phase space correlation between θ_{y0} and $p_\perp$. The m_X^2 effect comes from the background tail events which are characterized by incorrectly measured hadronic decays. A z bias is caused by momentum measurement errors. The distribution of χ^2 or STD show that most of the effects are statistical fluctuations. As a preliminary upper limit for the systematic error, the largest STD is taken, which is 0.0114 μ_N (0.46 %).

3.7.6 Systematic: HTM and HYPE2 Ptk

As is written in equation D.10 the Ptk (or integral field) enters into the magnetic moment measurement. In the following lines the systematic error sources are described.

The HYPE2 magnet was already discussed in section 2.3.2. In the following lines there is a list with the relevant parameters of HYPE2.

magnet full aperture x	35.56 cm
magnet full aperture y	3.81 cm
magnet full length z	182 cm
magnet current	1520 $Amps$
magnetic field	26 kG
$\int B\,dl$	4.77 $T \cdot m$
Ptk	+1.4243 GeV/c
maximum hyperon spread in HYPE2	1.75 cm
magnetic field spatial uniformity	0.1 % in 2.0 cm (or 0.0014 GeV/c)
Ptk run by run spread	0.0020 GeV/c or 0.14 %

The systematic error associated to Ptk HYPE2 is 0.0020 GeV/c. This error was extracted from the fine momentum calibration procedure, see section 3.4. The systematic error on the magnetic moment due to the HYPE2 Ptk is 0.0006 μ_N (0.02 %).

The HTM magnet was already discussed in sections 2.2.3 and 3.5. In the following lines there is a list with the relevant parameters of HTM.

channel radio	350 m
channel most narrow width x	0.14 cm
channel most narrow width y	0.43 cm
channel exit width x	0.36 cm
channel exit width y	0.90 cm
magnet full length z	7.31 m
hyperon solid angle spread exiting HTM	0.62 $\mu sterad$
hyperon average momentum	377 GeV/c
hyperon momentum spread $\Delta p/p$	7% FWHM
hyperon horizontal angle spread	0.001 rad FWHM
magnet current	3230 $Amps$
magnetic field	3.46 kG
$\int B\,dl$	25.1 $T \cdot m$
Ptk for vertical mode	-7.5258 GeV/c
uncertainty Ptk total	0.0587 GeV/c (0.78 %)

The systematic error on the magnetic moment due to the HTM Ptk is 0.0162 μ_N (0.66 %).

The total Ptk is: $-7.5258 + 1.4243 = -6.1015\,GeV/c$.

The total precession angle is $-772.91^o + 146.28^o = -626.63^o$

$$(\text{or } -13.49 + 2.55 = -10.94\,rad).$$

3.7.7 Magnetic Moment Σ^+ and $\bar{\Sigma}^-$

The table 3.9 show the magnetic moment of the Σ^+ and $\bar{\Sigma}^-$. These magnetic moments are preliminary results. The systematic error in Σ^+ is dominated by the HTM Ptk . There is work in progress, as I write this thesis, for a 0.1 % HTM Ptk measurement. Both magnetic moments will be affected by the new measurement within the limits of the quoted systematic error associated to the HTM Ptk . The systematic error from the variable studies is dominated by the m_X^2 which can be corrected and leveled to the size of the statistical error. From the variation of the magnetic moment itself in the historical analysis it is feasible to loosen the cuts to gain a factor of two in number of events for the magnetic moment measurement. We are setting our goal for a ≈ 0.2 % Σ^+ magnetic moment measurement.

Table 3.5: Asymmetry Σ^+ .

Horizontal Targeting Mode				
nominal		Asymmetry		
targeting		σ statistical		
angle		**A**	σ	χ^2_ν/ν
(1)	(2)		$\mathbf{A_x}$	
-6.0	+4.0	0.0060	0.0112	1.06/11
-5.5	+3.5	-0.0096	0.0114	1.04/11
-5.0	+3.0	0.0143	0.0095	1.79/11
		-0.0011	0.0005	2.23/15
-4.5	+2.5	0.0016	0.0122	0.77/11
-2.0	0.0	-0.0113	0.0145	3.61/10
			$\mathbf{A_y}$	
-6.0	+4.0	-0.1021	0.0112	0.67/11
-5.5	+3.5	-0.1098	0.0113	1.95/11
-5.0	+3.0	-0.1099	0.0095	0.81/11
		-0.1212	0.0005	6.13/15
-4.5	+2.5	-0.1283	0.0121	0.27/11
-2.0	0.0	-0.1038	0.0145	1.24/10
			$\mathbf{A_z}$	
-6.0	+4.0	-0.0184	0.0116	1.42/11
-5.5	+3.5	0.0051	0.0118	2.23/11
-5.0	+3.0	0.0065	0.0098	1.68/11
		0.0014	0.0005	1.43/15
-4.5	+2.5	0.0097	0.0125	1.68/11
-2.0	0.0	-0.0099	0.0149	0.47/10
Vertical Targeting Mode				
(1)	(2)		$\mathbf{A_x}$	
-3.0	+3.0	0.0094	0.0036	0.61/11
			$\mathbf{A_y}$	
-3.0	+3.0	-0.0055	0.0036	1.00/11
			$\mathbf{A_z}$	
-3.0	+3.0	0.1598	0.0037	1.60/11

Table 3.6: Polarization Σ^+ .

Horizontal Targeting Mode							
Production				Polarization			
average			number	syst.		σ	
targeting	$< p_\perp >$	σ	of	from	P	stat.	syst.
angle	GeV/c	GeV/c	events	α			total
mrad							
H 4.73	1.77	0.10	23744	0.0017	0.1042	0.0114	0.0036
H 4.31	1.63	0.10	23173	0.0018	0.1120	0.0115	0.0037
H 3.66	1.38	0.08	43225	0.0018	0.1121	0.0097	0.0037
H 3.66	1.38	0.10	12573218	0.0020	0.1236	0.0005	0.0038
H 3.23	1.22	0.10	20351	0.0021	0.1309	0.0123	0.0039
V 2.58	1.00	0.06	249863	0.0027	0.1633	0.0038	0.0042
H 0.88	0.34	0.14	14134	0.0017	0.1059	0.0148	0.0037
common $x_f = 0.47$							
stat. and syst. mean statistic and systematic respectively common polarization syst. $\pm$ 0.0032							
syst. targeting angle spread is 0.34 *mrad* (σ) syst. $p_\perp$ spread is 0.13 GeV/c (σ) the incident proton dominates the angular spread							

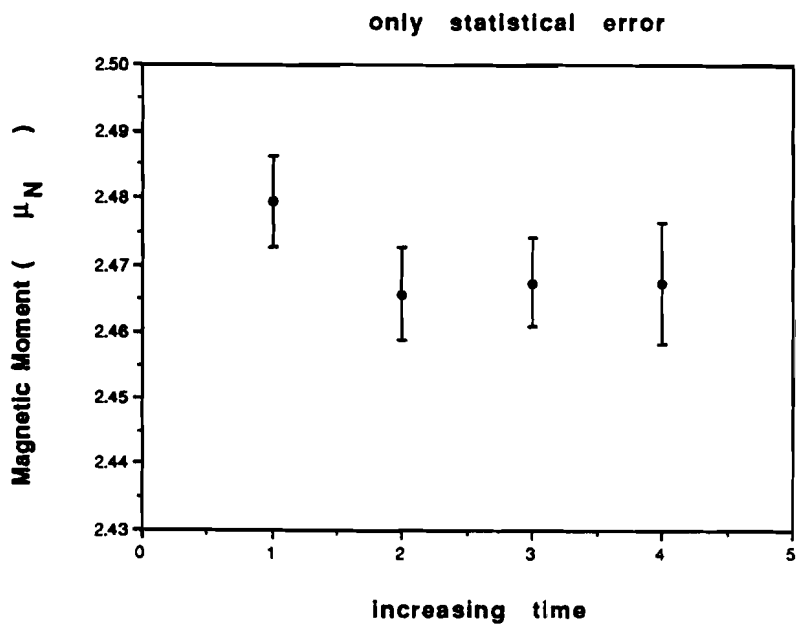

Figure 3.25: Magnetic Moment Versus Time.

Table 3.7: Asymmetry $\bar{\Sigma}^-$.

Horizontal Targeting Mode				
nominal		Asymmetry		
targeting		σ statistical		
angle		**A**	σ	χ^2_ν/ν
(1)	(2)		$\mathbf{A_x}$	
-4.0	+2.0	-0.0122	0.0103	1.12/11
-3.0	+1.0	0.0047	0.0113	1.69/11
-2.0	0.0	0.0124	0.0443	0.61/7
			$\mathbf{A_y}$	
-4.0	+2.0	0.0662	0.0103	1.22/11
-3.0	+1.0	0.0867	0.0112	1.00/11
-2.0	0.0	0.0470	0.0438	0.58/7
			$\mathbf{A_z}$	
-4.0	+2.0	0.0180	0.0106	0.75/11
-3.0	+1.0	-0.0047	0.0116	0.49/11
-2.0	0.0	0.0373	0.0460	1.87/7
Vertical Targeting Mode				
(1)	(2)		$\mathbf{A_x}$	
+3.0	-3.0	-0.0191	0.0166	1.65/10
			$\mathbf{A_y}$	
+3.0	-3.0	-0.0227	0.0167	2.38/10
			$\mathbf{A_z}$	
+3.0	-3.0	-0.0678	0.0171	0.56/10

Table 3.8: Polarization $\bar{\Sigma}^-$

Horizontal Targeting Mode							
Production				Polarization			
average			number	syst.		σ	
targeting	$< p_\perp >$	σ	of	from	**P**	stat.	syst.
angle	GeV/c	GeV/c	events	α			total
$mrad$							
V 2.64	1.01	0.06	11806	0.0012	0.0719	0.0174	0.0034
H 2.77	1.04	0.11	28957	0.0011	0.0676	0.0105	0.0034
H 1.76	0.66	0.13	23630	0.0014	0.0884	0.0114	0.0035
H 0.82	0.31	0.14	1554	0.0008	0.0480	0.0447	0.0033
common $x_f = 0.47$							
stat. and syst. mean statistic and systematic respectively common polarization syst. $\pm$ 0.0032							
syst. targeting angle spread is 0.34 $mrad$ (σ) syst. $p_\perp$ spread is 0.13 GeV/c (σ) the incident proton dominates the angular spread							

Table 3.9: Magnetic Moment.

systematic μ (μ_N)	
binning	$\pm$ 0.0013
variables	$\pm$ 0.0114
HYPE2	$\pm$ 0.0006
HTM	$\pm$ 0.0162

μ (μ_N)			
Σ^+	2.4707	$\pm$ 0.0035	$\pm$ 0.0199
$\bar{\Sigma}^-$	-2.4375	$\pm$ 0.0363	$\pm$ 0.0199

precession angle		
Σ^+	-626.6^o	$\pm$ 1.3^o
$\bar{\Sigma}^-$	-614.3^o	$\pm$ 13.5^o

the quoted numbers are preliminary

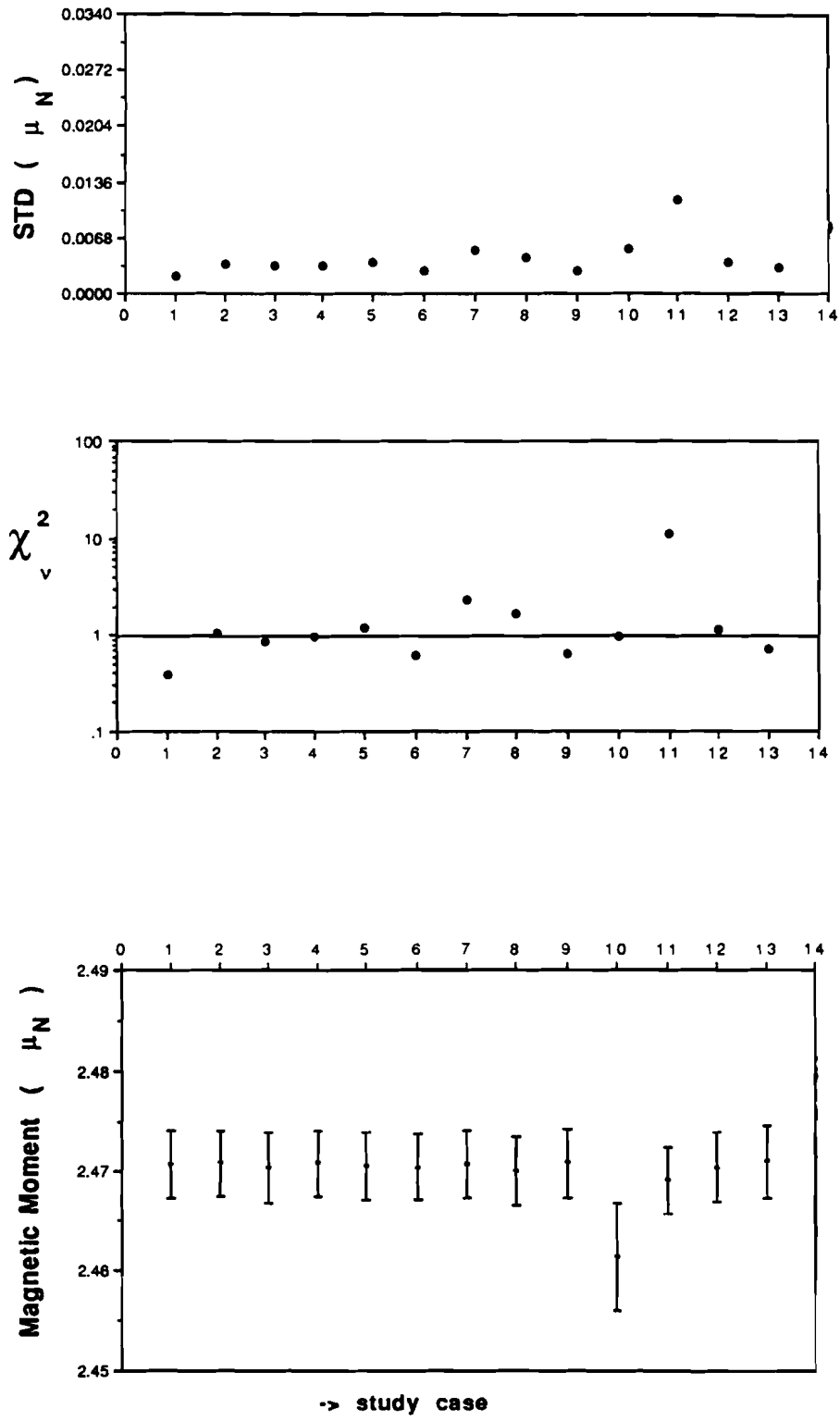

Figure 3.26: Magnetic Moment Study from Variable Splitting.

Chapter 4

Comparisons and Conclusions

4.1 Polarization Σ^+

Figure 4.1 shows the world Σ^+ polarization data. The same figure shows also the $p_\perp$ and x_f hyperon kinematical region. Table 4.1 shows the relevant parameters of each individual experiment.

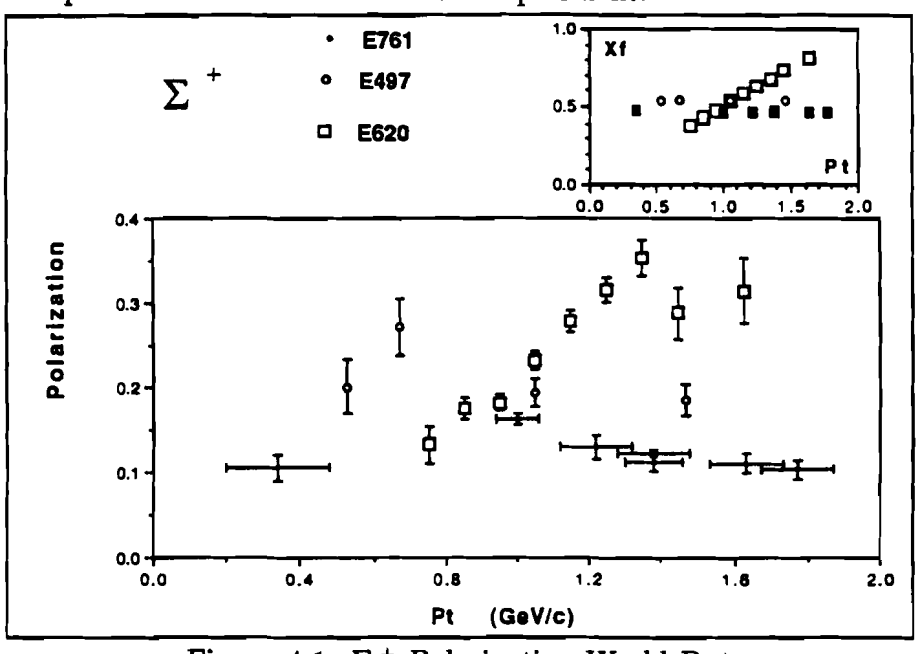

Figure 4.1: Σ^+ Polarization World Data.

From figure 4.1 it is noticeable that E497 and E761 were made at constant x_f while E620 varies $p_\perp$ and x_f at the same time. Several conclusions can be drawn from the E761 data:

- The Σ^+ polarization increases in $p_\perp$ from zero up to a maximum of 0.16 at 1.0 GeV/c. Collinear beam-hyperon interaction produces zero polarization by rotational symmetry. From there the polarization starts to rise. A common feature to all hyperon polarization.

- First observation of the polarization fall-off at high $p_\perp$. Perturbative QCD predicts zero polarization at high $p_\perp$ [55, 61]. However, no model can determine at which $p_\perp$ the polarization will show the fall-off, exceptional case of Dharmaratna et al. [63] on Λ^0 . In Figure 4.1 or 3.6 the polarization fall-off effect is visually highlighted. The fall-off is a 5.8σ effect, observing the points at $p_\perp$ of 1.0 and 1.38 GeV/c.

  Supporting E761 Σ^+ polarization $p_\perp$ fall-off, E497 shows a peak in the polarization at $p_\perp$ of ≈ 0.7 GeV/c. However, the polarization errors are too large to confirm the fall-off by themselves.

  Contrasting the Σ^+ , Λ^0 , the most studied polarized hyperon, is fitted to a constant polarization at high $p_\perp$ [19].

  Supporting the Σ^+ polarization fall-off, Ξ^- measured by Duryea, et all [43] shows also polarization magnitude fall off at $p_\perp$ greater than 1.0 GeV/c. However, the polarization errors are large to confirm the fall-off by themselves. It was an 800 GeV proton beam incident on a 0.22 interaction length (l_i) Be target.

- Comparing E497 and E761 where Δx_f is 0.05 or 11 % increase and Δbeam-energy is 400 GeV or 100 % increase the qualitative polarization difference is dominated by the beam energy change. This polarization difference, due to the beam energy, increases with increasing $p_\perp$. The polarization at 400 GeV is higher than the one at 800 GeV.

  Contrasting Σ^+ , Λ^0 polarization is constant as function of the beam energy in the range of 12 to 1600 Gev, see section 1.1.1.

  Contrasting Σ^+ , Ξ^- polarization magnitude at 400 GeV is lower than the one at 800 GeV [43, 41]. Note: 800 GeV data used 0.22 l_i Be target while 400 GeV data used 0.5 l_i Be target.

- Of all the $p_\perp$, x_f , and beam energy combinations only one pair match. The matching is between E620 and E497 at $p_\perp$ of 1.050 GeV/c, x_f of 0.52 and beam energy of 400 GeV. The only difference between those

points is the Be versus Cu and 0.5 versus 1.0 l_i target. The polarization of Be is higher than the one of Cu.

Supporting Σ^+ polarization material dependence, Λ^0 polarization magnitude produced on Be is higher than the combined polarization produced on Cu and on Pb, see section 1.1.1.

- Having discussed the dependences on $p_\perp$, material (l_i), and beam energy the fourth variable of interest is x_f . None of the first three mentioned polarization dependences are able to anticipate such a high increase of polarization as shown in E620 data. The only open explanation is to rely on a strong polarization dependence on the x_f variable.

  Supporting Σ^+ x_f dependence, E761 megasample at constant $p_\perp$ is broken into equal x_f intervals. As a result the polarization increases in x_f , see figure 3.17.

  Supporting Σ^+ x_f dependence, Λ^0 polarization magnitude increases on x_f at constant $p_\perp$, see section 1.1.1.

  Contrasting Σ^+ x_f dependence, Ξ^- [43] polarization is constant as a function of x_f at constant $p_\perp$.

All theoretical models, see section 1.1.2, do not address the Σ^+ polarization $p_\perp$ and x_f dependence. With the new accumulated data there is information to expand the leading particle models to describe production of Σ^+ polarization and Ξ^- polarization. The leading particle models are not the most general approach to hyperon polarization, see the following section.

4.2 Polarization $\bar{\Sigma}^-$

An important conclusion is the measurement of nonzero anti-hyperon polarization, see figure 4.2. The $\bar{\Sigma}^-$ and $\bar{\Xi}^+$ [45] nonzero polarization ruled out all the leading particle polarization models as the most general spin quark dynamics, see section 1.1.2. Leading particle models predict zero polarization since all anti-quark states are formed from the sea.

Figure 4.3 shows the Σ^+ and $\bar{\Sigma}^-$ polarization data. The x_f is fixed and common to both particles, only the $p_\perp$ region is different. The difference in $p_\perp$ region is due to the horizontal forbidden targeting angles, see section 2.2.3. The following conclusions can be drawn from the data:

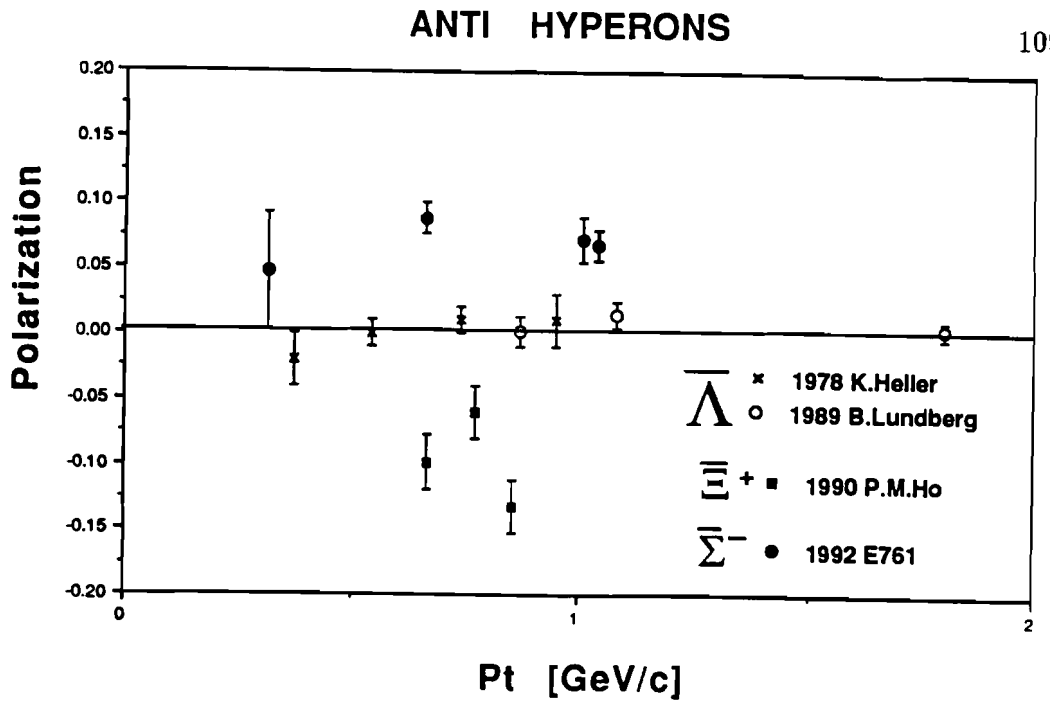

Figure 4.2: Anti-Hyperon Polarization.

- An experimental ability to measure same polarization in different modes, horizontal versus vertical, for $\bar{\Sigma}^-$ at $p_\perp$ of 1.0 GeV/c
- Similar $p_\perp$ kinematical behaviour as Σ^+ . The polarization raises from zero up to a maximum and then starts to fall-off.
- The $\bar{\Sigma}^-$ polarization is lower than the Σ^+ polarization at identical conditions. Contrasting $\bar{\Sigma}^-$ and Σ^+ relative polarization, $\bar{\Xi}^+$ and Ξ^- [45] have the same polarization.

At present there is no theoretical explanation for anti-hyperon polarization production. Nonzero anti-hyperon polarization is now measured in $\bar{\Sigma}^-$ and $\bar{\Xi}^+$ hyperons. A sizable amount of data, with small error bars, distributed in the $p_\perp$ and x_f variables is accessible on Λ^0 , Ξ^- , Ξ^0 , Σ^+ and $\bar{\Sigma}^-$ hyperons. The most promising procedure could be the one of Dharmaratna, since it is adequately able to address the low and high $p_\perp$ range at once.

4.3 Magnetic Moment

The Σ^+ magnetic moment measurement is important for two reason:

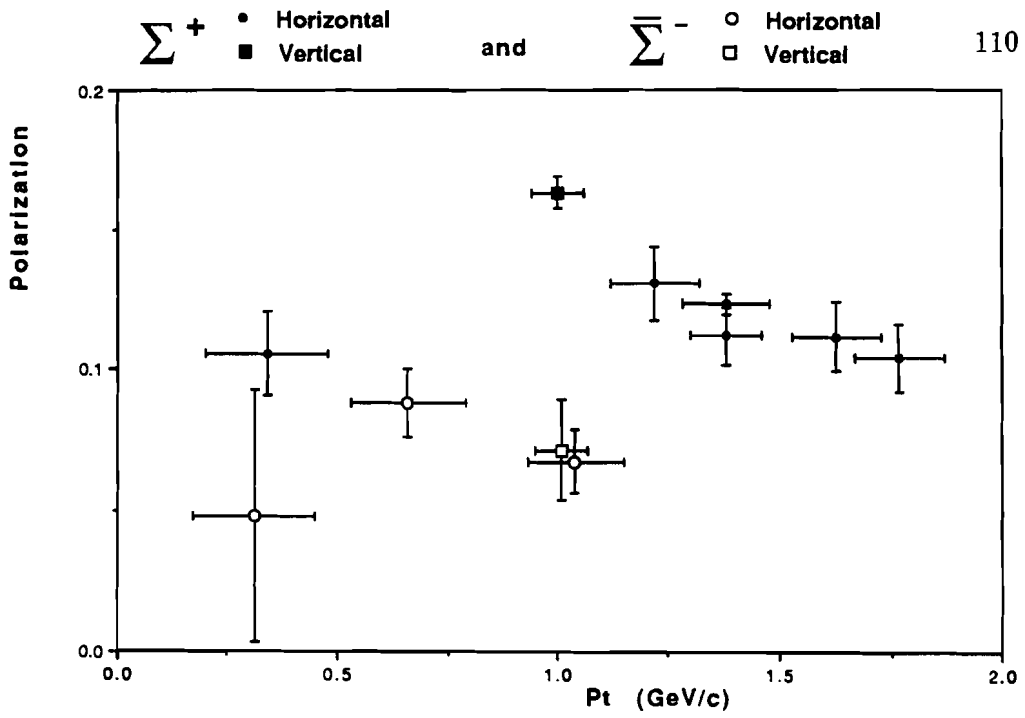

Figure 4.3: E761 $\bar{\Sigma}^-$ and Σ^+ Polarization.

- The need for magnetic moment measurements below the 1 % experimental precision. Today the best fit to magnetic moment data is able to reach a 4 % precision [95]. It excludes Ω^- , Δ^{++} and the transition magnetic moment $\Sigma\Lambda$ which are at the 10 % experimental precision.

- The need to resolve an experimental dilemma of two 1 % measurements which differ by 3 σ, see figure 4.4.

To fill the first request a 0.1 % precision measurement of the HTM Ptk is in progress as I am writing this thesis. A preliminary result of $\approx$ 1 % Σ^+ magnetic moment is able to cast some light on these measurements, see table 3.9 and figure 4.4.

The $\bar{\Sigma}^-$ magnetic moment has been measured for the first time, see table 3.9 and figure 4.4. The magnitude of the magnetic moment of Σ^+ and $\bar{\Sigma}^-$ agree within the statistical error by 0.9 σ.

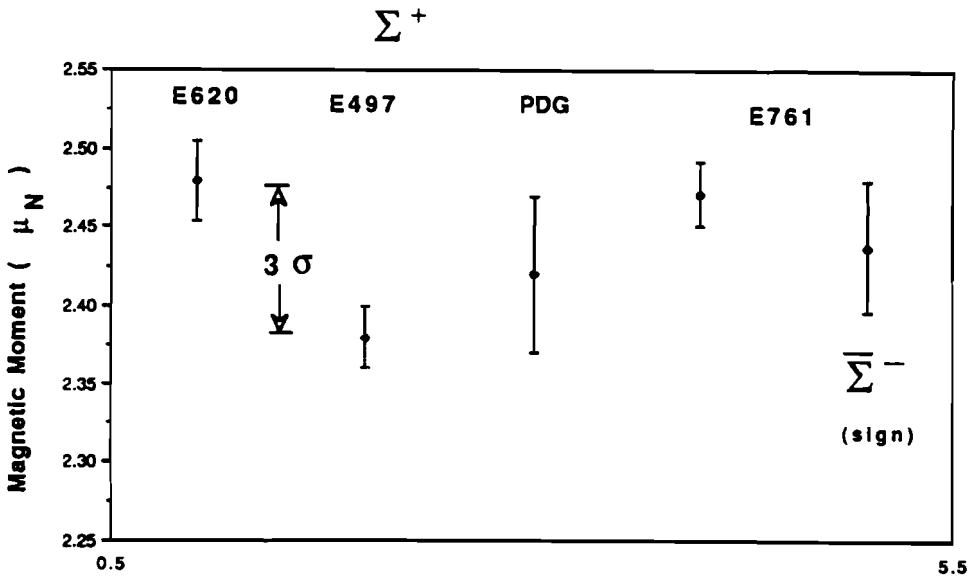

Figure 4.4: Σ^+ and $\bar{\Sigma}^-$ Magnetic Moment.

Table 4.1: Parameters of E620, E497, and E761.

	E620 [35]	E497[34]	E761
beam energy (GeV)	400	400	800
x_f		0.52	0.47
target material	Be	Cu	Cu
length (l_i)	0.5	1.0	1.0
length (l_c)	0.7	1.6	1.6

Appendix A

Fermilab Accelerator Complex

The ultimate goal of the Fermilab accelerator complex is to provide an 800 GeV proton beam to 15 parallel fixed target lines at the same time. One of these beam lines is called Proton Center, where E761 was located. The accelerator also provides $\bar{p} - p$ collisions for the collider facility, but that is a separate issue totally outside the scope of this thesis. It is understood that the accelerator complex is not part of E761 apparatus, but without it there could be no experiment. Figure A.1 shows an aerial view of Fermilab.

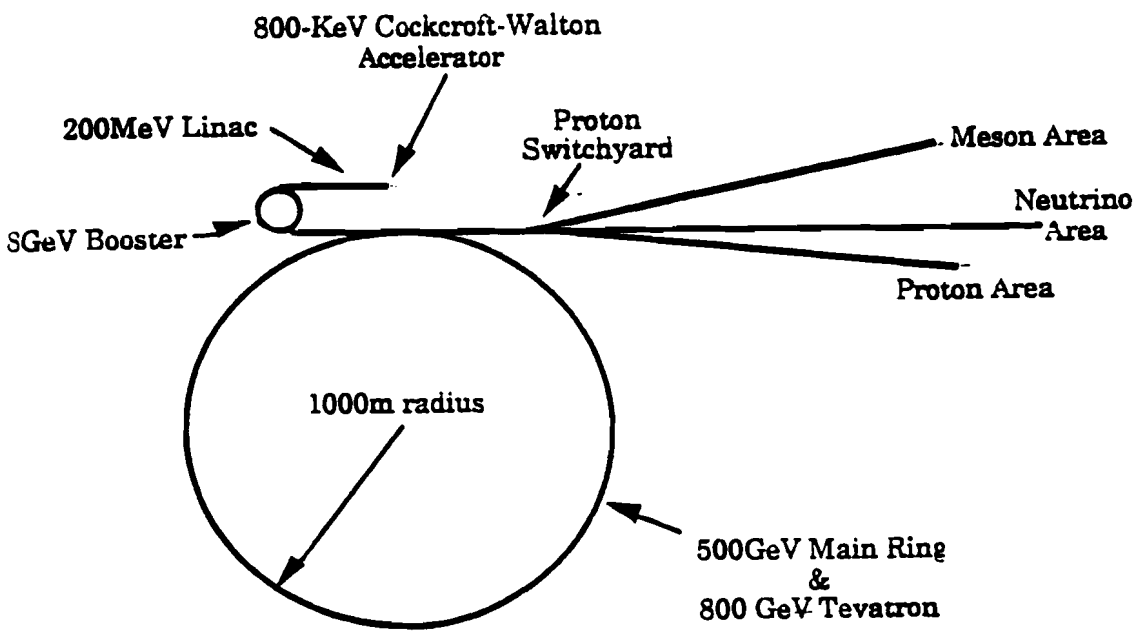

Figure A.1: Fermilab Accelerator Complex.

The accelerator works in stages. The first stages accelerate H^- ions while the last ones use protons. Table A.1 list in order the stages along with their characteristics.

Table A.1: Fermilab Acceleration Stages.

stage	type	energy	particle	dimension	
Gas Bottle	source		H_2		
Magnetron	ion source	18 keV	H^-	volume	$(5cm)^3$
Cockcroft Walton	charge	750 keV	H^-	length	60 cm
Linac	linear (RF)	200 MeV	H^-	length	150 m
Booster	synchrotron	8 GeV	p	circumference	475 m
Main Ring	synchrotron	150 GeV	p	circumference	6300 m
Tevatron	synchrotron	800 GeV	p	circumference	6300 m

The primary raw material is H_2. A Magnetron ion source [108] produces negative hydrogen ions. The Cockcroft Walton is a static charge capacitor accelerator. The Linac uses radio frequency to alternate the accelerating voltage as the H^- travels in a straight line path. A thin carbon foil removes the electrons from H^- as they enter into the Booster. The Booster and Main Ring are synchrotron accelerators with room temperature magnets. Tevatron is a synchrotron accelerator with superconducting magnets.

The H^- ion in the first stages causes an increase in p intensity at the final stage. The increase is due to a high focusing of neutral H in the intermediate step between Linac and Booster.

The accelerator proton intensity is 1 to 2 x 10^{13} *protons/pulse*. From stage to stage the beam is steered to other sections by dipole magnets. After the TEVATRON the proton beam is extracted to the fixed target switch yard. The switch yard uses a filament electrostatic separator, quadrupole magnets, and dipole magnets to split and transport the proton beam into experimental areas. One of those beam lines is Proton Center.

The beam intensity in Proton Center was in the range of 1 to 100 10^{10} *protons/pulse* (*ppp*). In the fixed target lines the proton beam is not a continuous current, it only exists for 21 *seconds* during a cycle of 60 *seconds*. This period of time, or pulse, is called spill.

There are so many technical details surrounding the accelerator that a branch named Accelerator Physics has been born. For an introduction to

accelerators see [109].

As soon as the proton beam is in the experimental area it is the responsibility of E761 to make good use of it. Here the E761 apparatus starts.

Appendix B

E761 Track Fit Algorithm

Track reconstruction technique depends solely on fitting straight line segments to the hits which have been recorded in each SSD or PWC. Hits are the wire or wires of each plane, properly specified in a coordinate system. In the case where multiple wires are on in one plane and they belong to the same track, a cluster rather than individual wires is more often used. One cluster is like one wire except that the cluster has a wider width than a single wire. In this section wire can mean a wire from a PWC or a strip from a SSD, also a hit can mean an individual wire or an individual cluster. In general I talk about a track regardless of whether it is a hyperon, a baryon, or an undecayed particle. Hyperon tracking uses only hit information from the hyperon spectrometer (SSD). Baryon tracking uses only hit information from the baryon spectrometer (PWC). The undecayed particles use all SSD and PWC hits.

Equations which describe horizontal track trajectory are obtained by approximating the magnetic field to a mid plane momentum deflection, see figure B.1. By geometry it can be proved that the deflection angle is:

$$\theta = \frac{\mathrm{Ptk}}{p}$$

$$[\theta] = radians, \ [\mathrm{Ptk}\ ] = [p] = GeV/c$$

The approximation $\sin(\theta/2) \approx \theta/2$ has to be made. The vertical momentum component is assumed to be negligible compared to the full momentum and its resolution, so the magnetic field allows us to measure the full particle momentum.

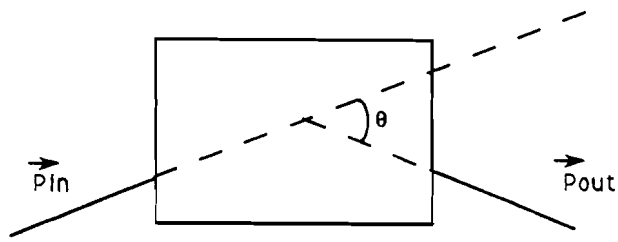

Figure B.1: Mid Plane Momentum Deflection.

With only vertical magnetic fields (parallel to $\hat{y}$) a track can be written as in the next parametric equation:

$$
\begin{aligned}
x = \; & x_0 + \theta_{x0}\; z \; -(z - z_{HYPE2})\frac{\mathrm{Ptk}_{\;HYPE2}}{p} \\
& \qquad -(z - z_{HTM})\frac{\mathrm{Ptk}_{\;HTM}}{p} && ; \quad -\infty < z < z_{HTM} \\
= \; & x_0 + \theta_{x0}\; z \; -(z - z_{HYPE2})\frac{\mathrm{Ptk}_{\;HYPE2}}{p} && ; \quad z_{HTM} < z < z_{HYPE2} \\
= \; & x_0 + \theta_{x0}\; z && ; \quad z_{HYPE2} < z < z_{MA} \\
= \; & x_0 + \theta_{x0}\; z \; +(z - z_{MA})\frac{\mathrm{Ptk}_{\;MA}}{p} \\
& \qquad +(z - z_{MB})\frac{\mathrm{Ptk}_{\;MB}}{p} \\
& \qquad +(z - z_{MB})\frac{\mathrm{Ptk}_{\;MB}}{p} && ; \quad z_{MC} < z < +\infty \\
y = \; & y_0 + \theta_{y0}\; z && ; \quad -\infty < z < +\infty
\end{aligned}
$$

where:

x_0 is the track intercept in x at SSD3,
θ_{x0} is the track angle in $x - z$ plane at SSD3,
y_0 is the track intercept in y at SSD3,
θ_{y0} is the track angle in $y - z$,
p is the particle momentum.

Each magnet z position is measured at its center. The reconstruction coordinate system origin is chosen to be at the center of SSD3. An expansion for the horizontal magnetic field component can be done by just rewriting the y in an equivalent way as x. The relation between track and hit in plane i can be written as:

$$hit_i = f_i(x_0, \theta_{x0}\ , y_0, \theta_{y0}\ , \frac{1}{p}) = x_i \cos(angle_i) + y_i \sin(angle_i)$$

where $angle_i$ is the orientation angle of the plane, and x_i,y_i are the respective values from the above track equation evaluated at their respective z_i plane. Remember that the planes are not necessarily x or y oriented, so one hit may have both x and y components.

The problem of track reconstruction turned into a linear fit problem. For a general discussion on data fitting see [5]. There are 5 variables in the fit which I group in vector $V = (x_0, \theta_{x0}\ , y_0, \theta_{y0}\ , \frac{1}{p})$. The fit is made with the χ^2 between track and hits written as:

$$\chi^2 = \sum_i \left(\frac{hit_i - f_i}{\frac{\Delta_i}{\sqrt{12}}} \right)^2$$

Δ_i is the wire spacing associated to plane i. The $\sqrt{12}$ factor is associated to a spatial uniform probability for a particle crossing the wire spacing. The $\sum$ goes over as many hits have been recorded in the track. The E761 algorithm had one hit (cluster) per plane.

The χ^2 minimization on each of the five variables reduces to a matrix equation:

$$D = M \cdot V$$

where:

$$D_k = \sum_i \left(\frac{\frac{\partial f_i}{\partial v_k} hit_i}{\Delta_i^2} \right)$$

$$M_{kj} = \sum_i \left(\frac{\frac{\partial f_i}{\partial v_k} \frac{\partial f_i}{\partial v_j}}{\Delta_i^2} \right)$$

$$k = 1, ..., 5 \qquad\qquad j = 1, ..., 5$$

Variables $V = (x_0, \theta_{x0}, y_0, \theta_{y0}, \frac{1}{p})$ are found by inverting the matrix M:

$$V = M^{-1} \cdot D$$

Error or resolution for each one of the five variables $V = (x_0, \theta_{x0}, y_0, \theta_{y0}, \frac{1}{p})$ is given by the diagonal terms of the inverse M matrix:

$$\sigma_{v(k)} = \sqrt{(M^{-1})_{kk}} \qquad\qquad k = 1, ..., 5$$

It is worth noting that the error matrix only depends on constants. These constants are fixed by the geometry of the apparatus.

In brief, the reconstruction of the track is equivalent to specify the values:

x_0	track intercept in x at SSD3,
θ_{x0}	track angle in $x - z$ plane at SSD3,
y_0	track intercept in y at SSD3,
θ_{y0}	track angle in $y - z$,
$\frac{1}{p}$	inverse of the particle momentum, and
χ^2_ν	reduced χ^2, a measure of the fit quality.

Appendix C

Bias Canceling Method (BCM)

The bias canceling method obtains the asymmetry ($\mathbf{A}$) using only experimental data. It requires data from a pair of symmetric targeting angles.

For a two body particle decay, such as hyperon $\rightarrow$ baryon + neutral, if the hyperon is polarized then the baryon angular distribution in the hyperon CM is given by:

$$\frac{dN}{d\Omega} = a(\Omega)N_0\frac{1}{4\pi}(1 + \vec{\mathbf{A}} \cdot \hat{p}_b) \tag{C.1}$$

where:

$\vec{\mathbf{A}}$ is the asymmetry defined as $\vec{\mathbf{A}} = \alpha\ \vec{\mathbf{P}}$; $\vec{\mathbf{P}}$ is the hyperon polarization vector. α is the asymmetry parameter.

$\hat{p}_b$ is a unit vector along the baryon momentum in the hyperon CM.

$a(\Omega)$ is the experimental, ad-hoc, weighting function representing the acceptance.

N_0 is the total number of events in the sample.

The BCM method, for obtaining the asymmetry components from purely experimental data is based on the following facts:

- Independent baryon angular distributions in the hyperon CM apply to the experimental data for each asymmetry component.

$$\frac{dN}{d\cos\theta} = aN_0\frac{1}{2}(1 + \mathbf{A}\ \cos\theta)$$

where: $\cos\theta = \cos\theta_x, \cos\theta_y$ or $\cos\theta_z$ and $\mathbf{A} = \mathbf{A_x}$, $\mathbf{A_y}$ or $\mathbf{A_z}$.

It requires making the integral of equation C.1 in the azimuthal angle for each cosine distribution. The azimuthal acceptance is approximated to a constant in each case.

- The polarization magnitude is the same for both targeting angles;

$$\mathbf{A}^{(2)} = -\mathbf{A}^{(1)}$$

All the asymmetry studies used the arithmetic mean. Only once for comparison the geometric mean was used. In the following sections I describe both.

C.1 Arithmetic Mean (BCMAM)

The arithmetic mean requires that the acceptance function for the pair of symmetric targeting angle data be the same [1] ; $a_i^{(2)} = a_i^{(1)}$.

Based on all above facts, and using a numerical function (histogram) for $\frac{dN}{d\cos\theta}$, I can write the baryon angular distribution for each targeting angle,

[1] Using the arithmetic mean and allowing the acceptance and polarization be different by a small amount as:

$$a_i^{(1)} = a_i + \Delta a_i$$

$$a_i^{(2)} = -(a_i - \Delta a_i)$$

$$\mathbf{A}^{(1)} = \mathbf{A} + \Delta\mathbf{A}$$

$$\mathbf{A}^{(2)} = \mathbf{A} - \Delta\mathbf{A}$$

With the equivalent equations to C.2 and C.3, and doing the same arithmetic exercise, equation C.4 now becomes:

$$\epsilon_i = \frac{\Delta a_i}{a_i} + \mathbf{A}\, z_i - \mathbf{A}^2 \left(\frac{\Delta\mathbf{A}}{\mathbf{A}} + \frac{\Delta a_i}{a_i}\right) z_i^2$$

the above equation shows that Δa and $\Delta\mathbf{A}$ do not cancel to first order in the arithmetic mean. The geometric mean cancel both variations to first order.

(1) and (2), and each asymmetry component as:

$$x_i = a_i \frac{1}{2}(1 + \mathbf{A}^{(1)} z_i) \tag{C.2}$$

$$y_i = a_i \frac{1}{2}(1 - \mathbf{A}^{(1)} z_i) \tag{C.3}$$

where:

$z = \cos\theta$,

i makes reference to the bin ith in $\cos\theta$,

a_i is the acceptance in bin i,

$$x_i = \frac{N_i^{(1)}}{N_0^{(1)}} \quad , \quad N_0^{(1)} = \sum_{k=1}^{m} N_k^{(1)},$$

$$y_i = \frac{N_i^{(2)}}{N_0^{(2)}} \quad , \quad N_0^{(2)} = \sum_{k=1}^{m} N_k^{(2)}.$$

$N_i^{(1)}$ and $N_i^{(2)}$ are the number of events from targeting angle (1) and (2),respectively, inside the ith cosine bin. $N_0^{(1)}$ and $N_0^{(2)}$ are the total number of events in each cosine distribution, which has a total of m bins. It is equivalent to $\left.\frac{\Delta N}{\Delta \cos\theta}\right|_i / \left(\sum_k \left.\frac{\Delta N}{\Delta \cos\theta}\right|_k\right)$ for each symmetric targeting angle.

To remove the biases in acceptance from the asymmetry ($\mathbf{A}$) measurement it is enough to take the ratio of the difference to the sum of equations C.2 and C.3:

$$\epsilon_i = \mathbf{A}^{(1)} z_i \tag{C.4}$$

where:

$$\epsilon_i = \frac{x_i - y_i}{x_i + y_i} \tag{C.5}$$

The problem of measuring the asymmetry has been enormously simplified as stated in equation C.4. The next step is to make the fit of ϵ against the linear term $\mathbf{A}^{(1)} z$. Care should be taken in propagating the counting

error from the N's into the ϵ error. The fit is made through χ^2 minimization, where χ^2 is defined as:

$$\chi^2 = \sum_{ij}(\mathbf{A}\ ^{(1)}z_i - \epsilon_i)W_{ij}(\mathbf{A}\ ^{(1)}z_j - \epsilon_j)$$

where: W is the inverse of the covariance matrix : $W_{ij} = [\sigma_{ij}^2]^{-1}$

The covariance matrix is defined in terms of ϵ as:

$$\sigma_{ij}^2 =< \Delta\epsilon_i \Delta\epsilon_j >$$

$\Delta\epsilon_i$ can be written as:

$$\Delta\epsilon_i = \frac{\partial\epsilon_i}{\partial N_k}\Delta N_k\ ;\ k = 1, 2, ..., 2m\ ;\ \text{(index summation convention assumed)}$$

where:

$$N_k = \begin{cases} N_k^{(1)} & k = 1, 2, ..., m \\ N_k^{(2)} & k = m+1, m+2, ..., 2m \end{cases}$$

so the covariance matrix can be written as:

$$\sigma_{ij}^2 = \frac{\partial\epsilon_i}{\partial N_k}\frac{\partial\epsilon_j}{\partial N_l} < \Delta N_k \Delta N_l >$$

since the N_k are independent numbers of counts [2] then:

$$< \Delta N_k \Delta N_l >= N_k \delta_{kl}$$

the covariance matrix takes the form:

$$\sigma_{ij}^2 = \frac{\partial\epsilon_i}{\partial N_k}\frac{\partial\epsilon_j}{\partial N_k}N_k$$

the partial derivative can then be written as:

$$\frac{\partial\epsilon_i}{\partial N_k} = \frac{\partial\epsilon_i}{\partial x_i}\frac{\partial x_i}{\partial N_k} + \frac{\partial\epsilon_i}{\partial y_i}\frac{\partial y_i}{\partial N_k}$$

after algebra and noticing that $1 - \epsilon_i^2 = \dfrac{4x_i y_i}{(x_i + y_i)^2}$, the partial takes the form:

$$\frac{\partial\epsilon_i}{\partial N_k} = \begin{cases} \dfrac{-(1-\epsilon_i^2)}{2N_0^{(1)}}(1 - \dfrac{\delta_{ik}}{x_i}) & k = 1, 2, ..., m \\ \\ \dfrac{1-\epsilon_i^2}{2N_0^{(2)}}(1 - \dfrac{\delta_{il}}{y_i}) & l = k - m \quad k = m+1, m+2, ..., 2m \end{cases}$$

[2] $< (\Delta N)^2 > \quad = \quad \sigma_{N^2} \quad =$ N or zero for $k \neq l$, there is no correlation.

Substituting the partial derivatives into σ_{ij}^2, and writing x_i *and* y_i explicitly in terms of the N's, σ_{ij}^2 will have two terms: $\sum_{k=1}^{m}$ *and* $\sum_{k=m+1}^{2m}$. The second term can be rewritten into $\sum_{k=1}^{m}$ by just redefining the dummy indices l *and* k. After some algebra σ_{ij}^2 takes the form:

$$\sigma_{ij}^2 = \frac{(1-\epsilon_i^2)(1-\epsilon_j^2)}{4}\left[\delta_{ij}\left(\frac{1}{N_i^{(1)}}+\frac{1}{N_i^{(2)}}\right)-\left(\frac{1}{N_0^{(1)}}+\frac{1}{N_0^{(2)}}\right)\right]$$

Since the covariance matrix (σ_{ij}^2) is symmetric, the inverse (W) will be also. Minimizing χ^2 for the parameter $\mathbf{A}$ $(\frac{\partial\chi^2}{\partial\mathbf{A}} = 0)$ the asymmetry takes the form:

$$\mathbf{A}^{(1)} = \frac{\sum_{ij} z_i W_{ij}\epsilon_j}{\sum_{ij} z_i W_{ij} z_j}$$

The error in $\mathbf{A}^{(1)}$ is written as:

$$\sigma_{\mathbf{A}^{(1)}} = \sqrt{\frac{1}{\sum_{ij} z_i W_{ij} z_j}}$$

It turns out that the non-diagonal terms of the covariance matrix are small and negative. Omitting them, therefore, does not change the error significantly and does simplify the calculation. Under this approximation:

$$W_{ij} = \frac{1}{\sigma_{ii}^2}\delta_{ij}$$

C.2 Geometric Mean (BCMGM)

The geometric mean makes a reflection of the event distribution in $\cos\theta$ from -1.0 to 0.0 into an event distribution in $\cos\theta$ from 0.0 to 1.0, see figure C.1. The four event distributions, two per targeting angle, can be written as:

$$N_i^{(1R)} = a_i^{(1R)} N_0^{(1)} \sigma E^{(1R)} \frac{1}{2}(1+\mathbf{A}^{(1)} z_i)$$

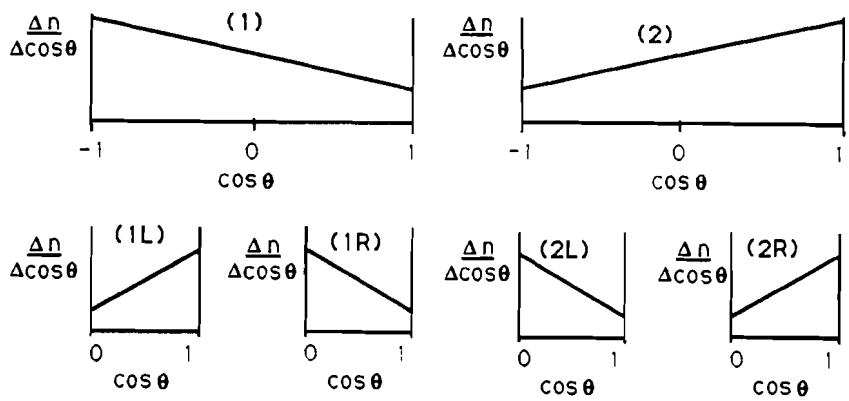

Figure C.1: Geometric Mean.

$$N_i^{(1L)} = a_i^{(1L)}\, N_0^{(1)}\, \sigma\, E^{(1L)} \frac{1}{2}(1 - \mathbf{A}^{\,(1)} z_i)$$

$$N_i^{(2R)} = a_i^{(2R)}\, N_0^{(2)}\, \sigma\, E^{(2R)} \frac{1}{2}(1 - \mathbf{A}^{\,(1)} z_i)$$

$$N_i^{(2L)} = a_i^{(2L)}\, N_0^{(2)}\, \sigma\, E^{(2L)} \frac{1}{2}(1 + \mathbf{A}^{\,(1)} z_i)$$

where:

$z = \cos\theta$,

i makes reference to the bin ith in $\cos\theta$,

$N_i^{(1R)}$ is the number of events of right (R) side of targeting angle one (1) inside the ith cosine bin,

a_i^{1R} is the acceptance of right (R) side of targeting angle one (1) distribution in the ith cosine bin,

$N_0^{(1)}$ is the integrated beam count for the targeting angle one (1) case,

σ is the cross section,

$E^{(1R)}$ is the efficiency of right (R) side of targeting angle one (1),

similar definitions for $(1L)$, $(2R)$ and $(2L)$.

The removal of biases in acceptance from the asymmetry ($\mathbf{A}$) measurement can be made as follows:

$$\epsilon_i = \mathbf{A}^{(1)} z_i \tag{C.6}$$

where:

$$\epsilon_i = \frac{\sqrt{N_i^{(1R)} N_i^{(2L)}} - \sqrt{N_i^{(1L)} N_i^{(2R)}}}{\sqrt{N_i^{(1R)} N_i^{(2L)}} + \sqrt{N_i^{(1L)} N_i^{(2R)}}} \tag{C.7}$$

the following assumption should be made: $(aE)^{(2)} = (aE)^{(1)}$.

The covariance matrix ($\sigma_{ij}^2 =< \Delta\epsilon_i \Delta\epsilon_j >$) does not include cross terms and can be written as:

$$\sigma_{ij}^2 = \left(\frac{1-\epsilon_i^2}{4}\right)^2 \left(\frac{1}{N_i^{(1R)}} + \frac{1}{N_i^{(1L)}} + \frac{1}{N_i^{(2R)}} + \frac{1}{N_i^{(2L)}}\right) \delta_{ij}$$

As in the arithmetic mean, the next step is to make the fit of ϵ against the linear term $\mathbf{A}^{(1)} z$. The fit is made through χ^2 minimization, where χ^2 is defined as:

$$\chi^2 = \sum_{ij} (\mathbf{A}^{(1)} z_i - \epsilon_i) W_{ij} (\mathbf{A}^{(1)} z_j - \epsilon_j)$$

where: W is the inverse of the covariance matrix : $W_{ij} = [\sigma_{ij}^2]^{-1}$

Minimizing χ^2 for the parameter $\mathbf{A}$ ($\frac{\partial \chi^2}{\partial \mathbf{A}} = 0$) the asymmetry takes the form:

$$\mathbf{A}^{(1)} = \frac{\sum_{ij} z_i W_{ij} \epsilon_j}{\sum_{ij} z_i W_{ij} z_j}$$

The error in $\mathbf{A}^{(1)}$ is written as:

$$\sigma_{\mathbf{A}^{(1)}} = \sqrt{\frac{1}{\sum_{ij} z_i W_{ij} z_j}}$$

Appendix D

Spin Precession in a Magnetic Field

This appendix describes the rotation of the particle's spin while the charged particle itself travels through a magnetic field. The net rotation angle of the spin is obtained in a non-rotational reference system.

The magnetic moment of a particle can be written as:

$$\vec{\mu} = \frac{g}{2}\frac{q}{mc}\vec{s} \tag{D.1}$$

where g, q, m, and $\vec{s}$ are the particle's Lande factor charge, mass, and spin, and c is the speed of light.

The spin experiences a torque under an external magnetic field. In the particle's center of mass system (or rest frame) the change in time of the spin can be written as:

$$\frac{d\vec{s}}{d\tau} = \vec{\mu} \times \vec{B}' \tag{D.2}$$

where: τ and $\vec{B}'$ are the time and magnetic field in the particle's rest frame.

With $dt = \gamma d\tau$, $\vec{B}' = \gamma\vec{B}$ (the particle's velocity is perpendicular to the magnetic field) and substituting the magnetic moment (D.1) into D.2 the torque expression can be rewritten as:

$$\frac{d\vec{s}}{dt} = \frac{g}{2}\frac{q}{mc}\vec{s} \times \vec{B} \tag{D.3}$$

where: t and $\vec{B}$ are the time and magnetic field in the laboratory reference system. Notice that the $\vec{s}$ components are in the particle's rest frame.

The particles's rest frame is a coordinate system with one of its axis parallel to the particle's path in the laboratory system. While the charged particle travels through the magnetic field the particles's rest frame rotates as the particle's path bends by the magnetic field. To obtain the net rotation angle of the spin a non-rotational coordinate system is required. The difference of the rotation angle of the spin in the non-rotational frame minus the rotation angle of the velocity is the net rotation angle of the spin in the non-rotational frame.

The vector (spin) change on time relation between a rotational and non-rotational reference frame is written as [9]:

$$\left.\frac{d\vec{s}}{dt}\right|_{non-rotational} = \left.\frac{d\vec{s}}{dt}\right|_{rest\,frame} + \omega_T \times \vec{s} \tag{D.4}$$

where ω_T is the Thomas Precessional Frequency [9] given by:

$$\omega_T = \frac{\gamma^2}{(\gamma+1)}\frac{\vec{a}\times\vec{v}}{c^2} \tag{D.5}$$

Substituting ω_T D.5, $\vec{a}$ by the Lorentz Force ($\vec{a} = \frac{q}{\gamma mc}\vec{v}\times\vec{B}$), and equation D.3 into D.4 the change on time of the spin can be written as [1] :

$$\left.\frac{d\vec{s}}{dt}\right|_{non-rotational} = \frac{q}{mc}\left(\frac{g}{2} - 1 + \frac{1}{\gamma}\right)\vec{s}\times\vec{B} \tag{D.6}$$

where the assumption $\vec{v}\cdot\vec{B} = 0$ has been done.

Requiring that $\vec{s}$ and $\vec{B}$ be perpendicular, defining $\Delta\phi = \frac{\Delta s}{s}$, and using $\Delta t = \frac{\Delta l}{v}$ equation D.6 can be written as:

$$\Delta\phi|_{non-rotational} = \frac{q}{mc^2}\frac{1}{\beta}\left(\frac{g}{2} - 1 + \frac{1}{\gamma}\right)\int Bdl \tag{D.7}$$

The rotation of the rest frame itself is the rotation of the velocity. The velocity angle change is obtained from the Lorentz Force. Requesting that $\vec{v}$ and $\vec{B}$ be perpendicular and defining $\Delta\phi = \frac{\Delta v}{v}$ the rotation angle of the velocity itself can be written as:

$$\Delta\phi|_{velocity} = \frac{q}{\gamma mc^2}\frac{1}{\beta}\int Bdl \tag{D.8}$$

[1] Equation D.6 is a special case of the BMT equation (Bargmann,Michel and Telegdi) [9, 16] which describes the spin motion in a general electromagnetic field.

The net rotation angle of the spin is the difference of equations D.7 minus D.8:

$$\phi = \frac{q}{mc^2}\frac{1}{\beta}\frac{g-2}{2}\int Bdl \tag{D.9}$$

Using equation D.1, the definition of Ptk (see section 2.2.3), and equation D.9 the absolute value of the magnetic moment in Nuclear Magneton units ($\mu_N = \frac{e\hbar}{2m_pc}$) can be written as:

$$|\mu| = \frac{m_p}{m}\left(1 + \beta mc^2\frac{\phi}{\text{Ptk } c}\right) \tag{D.10}$$

where m_p is the proton mass.

The angle ϕ is measured from the asymmetry ($\vec{A}$) components obtained from the data. The sign of ϕ is positive if the rotation went counter-clockwise. The experiments produce the polarization vector perpendicular to a vertical magnetic field at the proton beam target interaction. The polarization at production point will be parallel to an explicit coordinate axis ($+\hat{x}$). On this description the angle ϕ will be obtained as:

$$\phi = \arctan\left(\frac{|\mathbf{A_x}|}{|\mathbf{A_z}|}\right) + \text{quadrant correction} + n \cdot 2\pi \tag{D.11}$$

where n can not be determined with the experiment itself. The value n is obtained from previous measurements.

Bibliography

[1] Review of Particle Properties, *Phys. Rev. D* , 45, 1, (1992).

[2] D.B. Lichtenberg *Unitary Symmetry and Elementary Particles*, (2nd Edition, Academic Press, 1978).

[3] G. Arfken *Mathematical Methods for Physicists* , (2nd Edition, Academic Press, 1970).

[4] D.H. Perkins *Introduction to High Energy Physics* , (2nd Edition, Benjamin/Cummings Publishing Company, Inc., 1982).

[5] Philip R. Bevington *Data Reduction and Error Analysis for the Physical Sciences*, (McGraw-Hill, New York, 1969).

[6] W.R. Leo *Techniques for Nuclear and Particle Physics Experiments*, (Springer-Verlag Berlin Heidelberg 1987).

[7] Bruno Rossi *High Energy Particles* , (Prentice-Hall, Inc., Englewood Cliffs, N.J., 3th printing 1961).

[8] G.Moreno & L.Villaseñor *Revista Mexicana de Física*, 36 Suplemento 1 (1990).

[9] J.D. Jackson *Classical Electrodynamics* , (2nd edition John Wiley & Sons, Inc. 1975).

[10] E.Jastrzembski, *Charged Hyperon Fluxes*, Hyperon Physics at the Tevatron, Workshop, Fermilab, 16, (1984).

[11] T.Cardello *Thechnical Memo Fermilab*, TM-964 2257 (1984).

[12] M.Foucher et al., *Phys. Rev. Lett.*, 68, 3004, (1992).
and
M.Foucher, *Ph. D. Thesis*, Yale University, (1992), Unpublished.

[13] D. Chen et al., *Submited to Phys. Rev. Lett.*, (September 4, 1992). Fermilab Pub-92/242.
and
D. Chen, *Ph. D. Thesis*, State University of New York - Albany (1992), Unpublished.

[14] V.W. Hughes et al., *"last page"* , Proceedings of the International Symposium on Polarization Phenomena of Nucleons, Basel, Switzerland, (July 1960).

[15] T.D. Lee, *Preludes in Theoretical Physics*, (North-Holland Publishing Co., pp. 5-16 1966)
and
T.D. Lee, *Selected Papers V-2*, (Birkhauser · Boston · Basel · Stuttgart pp. 391-402 1986).

[16] V. Bargmann, L. Michel, V.L. Telegdi, *Phys. Rev. Lett.*, 2, 435, (1959).

[17] Lee G. Pondrom, *Phys. Rep.*, 122, 57, (1985).

[18] J. Lach *Magnetic Moments of the Baryons An Experimental Review* , Proceedings of the 9th International Symposium on High Energy Spin Physics, Volume 1, p 87, Bonn, FRG, (1990)
and
J. Lach *Hyperons: Insights Into Baryon Structures* , Invited lectures given at 4th Mexican School of Particles and Fields, Oaxtepec, Mexico, (1990), (FERMILAB-CONF-91-200, 1991) .

[19] K. Heller *Hyperon Polarization at High Energy*, Proceedings of the 9th International Symposium on High Energy Spin Physics, Volume 1, p 97, Bonn, FRG, (1990).

[20] R.O. Bangerter et al., *Phys. Rev. Lett.*, 17, 495, (1966) .

[21] R.O. Polvado et al., *Phys. Rev. Lett.*, 42, 1325, (1979).

[22] G.Bunce et al., *Phys. Rev. Lett.*, 36, 1113, (1976).

[23] K. Heller et al., *Phys. Lett. B*, 68, 480, (1977) .

[24] P. Skubic et al., *Phys. Rev. D* , 18, 3115, (1978).

[25] K. Heller et al., *Phys. Rev. Lett.*, 41, 607, (1978) .

[26] S. Erhan et al., *Phys. Lett. B*, 82, 301, (1979).

[27] F. Lomanno et al., *Phys. Rev. Lett.*, 43, 1905, (1979).

[28] F. Lomanno et al., *Phys. Lett. B* , 96, 223, (1980).

[29] S.A. Gourlay et al., *Phys. Rev. Lett.*, 56, 2244, (1986).

[30] F.Abe et al., *Phys. Rev. D*, 34, 1950, (1986).

[31] A.M. Smith et al., *Phys. Lett. B* , 185, 209, (1987).

[32] B.E. Bonner et al., *Phys. Rev. D*, 38, 729, (1988).

[33] B. Lundberg et al., *Phys. Rev. D*, 40, 3557, (1989).

[34] C. Ankenbrandt, et al., *Phys. Rev. Lett.*, 51, 863, (1983)
and
Y. W. Wah, *Ph. D. Thesis*, Yale University, (1983), Unpublished.

[35] C. Wilkinson et al., *Phys. Rev. Lett.*, 58, 855, (1987) .

[36] C. Dukes et al., *Phys. Lett. B* , 193, 135, (1987).

[37] P.C. Petersen et al., *Phys. Rev. Lett.*, 57, 949, (1986).

[38] L. Deck et al., *Phys. Rev. D*, 28, 2, (1983).

[39] Y.W. Wah et al., *Phys. Rev. Lett.*, 55, 2551, (1985).

[40] K. Heller et al., *Phys. Rev. Lett.*, 51, 2025, (1983).

[41] R. Rameika et al., *Phys. Rev. D*, 33, 3172, (1986).

[42] L.H. Trost et al., *Phys. Rev. D*, 40, 1703, (1989).

[43] J. Duryea et al., *Phys. Rev. Lett.*, 67, 1193, (1991).

[44] J. Duryea et al., *Phys. Rev. Lett.*, 68, 768, (1992).

[45] P.M. Ho et al., *Phys. Rev. Lett.*, 65, 1713, (1990).

[46] M.J. Longo et al., *Polarization and Spin Transfer of* Ω^- *and* Ξ^- *Hyperons at 800 GeV* , Proceedings of the 8th International Symposium on High Energy Spin Physics, Volume 1, p 80, Minneapolis, MN, USA, (1988).

[47] H.T. Diehl et al., *Phys. Rev. Lett.*, 67, 804, (1991).

[48] H.T. Diehl *Ph. D. Thesis*, Rutgers - The State University of New Jersey, (1990), Unpublished.

[49] R. Rubinstein *Fermilab Research Program 1991 Workbook*, Fermilab, (1991).

[50] BIS-2 Collaboration *Sov. J. Nucl. Phys.*, 43, 395, (1986).

[51] M. Jezabek et. al., *Phys. Lett. B*, 286, 175, (1992).

[52] A. Bosshard et al., *Phys. Rev. D*, 44, 1962, (1991).

[53] Paige et al., *Phys. Rev. D*, 14, 2307, (1976) .

[54] Moriarty et al., *Lett. al Nuovo Cimento*, 19, 393, (1977) .

[55] G.L. Kane et al., *Phys. Rev. Lett.*, 41, 1689, (1978) .

[56] Andersson et al., *Phys. Lett. B*, 85, 417, (1979) .

[57] DeGrand et al., *Phys. Rev. D*, 24, 2419, (1981) .

[58] J. Szwed, *Phys. Lett. B*, 105, 403, (1981) .

[59] Andersson et al., *Phys. Rep.*, 97, 31, (1983) .

[60] P. Cea et al., *Phys. Lett. B*, 361, 193, (1987) .

[61] P. Cea et al., *Phys. Lett. B*, 209, 333, (1988) .

[62] J Szwed et al., *Hyperon Polarization and Multiple Quark Scattering*, Proceedings of the 8th International Symposium on High Energy Spin Physics, Volume 1, p 739, Minneapolis, MN, USA, (1988).

[63] Dharmaratna et al., *Phys. Rev. D* , 41, 1731, (1990) .

[64] J. Soffer et al., *Phys. Rev. Lett.* , 68, 907, (1992) .

[65] J. Franklin, *Phys. Rev.*, 172, 1807, (1968).

[66] A. DE Rújula et al., *Phys. Rev. D* , 12, 147, (1975).

[67] T. Barnes, *Nucl. Phys. B*, 96, 353, (1975).

[68] T. DeGrand et al., *Phys. Rev. D* , 12, 2060, (1975).

[69] H.J. Lipkin, *Phys. Rev. Lett.*, 41, 1629, (1978).

[70] R.B. Teese et al., *Phys. Lett. B*, 87, 111, (1979).

[71] Y. Tomozawa, *Phys. Rev. D* , 19, 1626, (1979).

[72] N. Isgur et al., *Phys. Rev. D* , 21, 3175, (1980).

[73] R. Verma, *Phys. Rev. D* , 22, 1156, (1980).

[74] G.E. Brown et al., *Phys. Lett. B*, 97, 423, (1980).

[75] T. Das et al., *Phys. Lett. B*, 96, 165, (1980).

[76] J. Franklin et al., *Phys. Rev. D* , 24, 2910, (1981).

[77] R.B. Teese, *Phys. Rev. D* , 24, 1413, (1981).

[78] A.W. Thomas et al., *Phys. Rev. D* , 24, 216, (1981).

[79] D.B. Lichtenberg, *Z. Physik C-Particles and Fields*, 7, 143, (1981).

[80] Y. Tomozawa, *Phys. Rev. D* , 25, 795, (1982).

[81] Y Nogami et al., *Phys. Rev. D* , 26, 261, (1982).

[82] W-Y.P. Hwang, *Z. Physik C-Particles and Fields*, 16, 327, (1983).

[83] H. Georgi et al., *Phys. Lett. B*, 132, 183, (1983).

[84] L.Brekke et al., *Phys. Rev. D* , 28, 1178, (1983).

[85] S. Theberge et al., *Nucl. Phys. A*, 393, 252, (1983).

[86] B. I. Ioffe et al., *Phys. Lett. B*, 133, 436, (1983).

[87] G.E. Brown et al., *Phys. Lett. B*, 128, 229, (1983).

[88] J. Franklin, *Phys. Rev. D* , 30, 1542, (1984).

[89] A.N. Mitra et al., *Phys. Rev. D* , 29, 1399, (1984).

[90] K. Ushio, *Phys. Lett. B*, 158, 71, (1985).

[91] Z. Dziembowski, et al., *Phys. Rev. Lett.* , 55, 1839, (1985).

[92] I. Sogami et al., *Phys. Rev. Lett.* , 54, 2295 (1985).

[93] J. Cohen et al., *Phys. Lett. B*, 165, 229, (1985).

[94] V.P. Efrosinin et al., *Sov. J. Nucl. Phys.*, 44, 681, (1986).

[95] S. K. Gupta et al., *Phys. Rev. D* , 36, 307, (1987).

[96] M. I. Krivoruchenko, *Sov. J. Nucl. Phys.*, 45, 109, (1987).

[97] R. Verma et al., *Phys. Lett. B*, 183, 207, (1987).

[98] C. B. Chiu et al., *Phys. Rev. D* , 36, 1553, (1987).

[99] Z. Dziembowski, et al., *Phys. Lett. B*, 200, 539, (1988).

[100] H. Hogaasen et al., *Phys. Rev. D* , 37, 1950, (1988).

[101] K. Charchula et al., *Phys. Lett. B*, 205, 358, (1988).

[102] L. Brekke et al., *Comm.Nucl.Part.Phys.* 18, 83, (1988).

[103] K. Tsushima et al., *Phys. Lett. B*, 205, 128, (1988).

[104] J.H. Kim et al., *Nucl. Phys. A*, 501, 835, (1989).

[105] K.-T. Chao *Phys. Rev. D* , 41, 920, (1990).

[106] D.B. Leinweber, *Phys. Rev. D* , 45, 252, (1992).

[107] D.B. Leinweber et al., *preprint Fermilab and Triumf TRI-PP-92-28*, (submited to Phys. Rev. D) (1992).

[108] Charles W. Schmidt, *Review of Negative Hydrogen Ion Source*, 1990 Linear Accelerator Conference, Albuquerque, NM, (September 1990).

[109] Stephen D. Holmes *A Practical Guide to Modern High Energy Particle Accelerators*, Theoretical Advanced Summer Institute, Santa Fe, New Mexico, July 6-24 (1987), FERMILAB-Conf-87/160.

Addendum:

The magnetic moment theoretical review is an extensive subject. I tried to include all authors which predicted or fitted the stable hyperon magnetic moments. My intention was good but partial, see pages 19 to 23. In the following lines I include another reference:

M. Bohm, R. Huerta and A. Zepeda,
Phys. Rev. D, 25 , 223, (1982).

It uses a confining harmonic-oscillator potential, orbital mixing, and symmetry breaking. The largest predicted precision is 12.4 % on the Σ^+. This model has the lowest precision of the potential models, see page 22.

I apologize with the authors that I may have omitted.